Study of Single Particle Spectra and Two Particle Correlations in Au+Au Collisions at 4 - 11 A GeV

Tatsuya CHUJO

A dissertation submitted to the Doctoral Program
in Physics, the University of Tsukuba
in partial fulfillment of the requirements for the
degree of Doctor of Philosophy (Science)

February, 2000

Abstract

We present the results of single particle spectra in Au+Au collisions at the energy of 4 and 11 A GeV, and the results of high statistic $\pi^+\pi^+$ two-particle correlations in Yano-Koonin Podgoretskii (YKP) parameterization in Au+Au collisions at 11 A GeV, measured by the E866 experiment using the Alternating Gradient Synchrotron (AGS) at Brookhaven National Laboratory (BNL).

For the systematic studies of hadron productions in relativistic heavy-ion collisions near mid-rapidity region, we have constructed a rotatable magnetic spectrometer, called the Forward Spectrometer. It is designed for the good particle identification capability under the condition of high particle density and for the wide range of kinematic coverage in Au+Au collisions at AGS. Using the data taken by the Forward Spectrometer, single particle spectra and HBT correlations are analyzed.

For single particle analysis, we have measured transverse mass spectra for $\pi^{\pm}$, K^+, protons and deuterons at 4 and 11 A GeV as a function of centrality. For the transverse mass spectra, we have observed the mass dependence of mean transverse mass $< m_t > -m_0$; for the particle with heavier mass, the larger $< m_t > -m_0$ is seen. In addition, the shapes of the m_t spectrum for protons have a shoulder-arm shape in central collisions at low m_t region. On the other hand, the pion spectra at 11 A GeV have a concave shape at low m_t region, which can be attributed, in part, to the effects of a transverse velocity field of a created system. Observed shoulder-arm shapes of protons and the mass dependence of mean transverse mass are consistent with an expanding source.

In $\pi^+\pi^+$ HBT correlation analysis in YKP parameterization, it is found that the extracted source size parameter in the transverse direction, R_t, decreases from 5.21 ± 0.17 fm to 3.73 ± 0.26 fm with increasing the transverse pair momentum K_T from 0.1 GeV/c to 0.45 GeV/c. This gradual decease of R_T with increasing K_T is also consistent with the expanding source.

Motivated by these observations that both single particle spectra and HBT correlations are qualitatively consistent with the picture of an expanding source, the simultaneous analysis of both data using the finite expanding source model is carried out for the first time at AGS energy. From this analysis, the freeze-out temperature T and the transverse expansion velocity β_t in Au+Au central collisions at 11 A GeV are extracted uniquely; $T = 95 \pm 5$ MeV and $< \beta_t >= 0.53 \pm 0.03$, which can be considered as more reliable values than those from the conventional analysis of single particle spectra alone.

Compared with $T = 120 \pm 12$ MeV and $< \beta_t >= 0.37 \pm 0.08$, reported from the former analysis at CERN-SPS 158 A GeV Pb+Pb collisions, T is larger at SPS than at AGS, while $< \beta_t >$ is larger at AGS than at SPS at the confidence level of 95 %. The softening of equation of state by the quark gluon plasma (QGP) formation is one of the qualitative interpretation for the observed small $< \beta_t >$ at SPS energy than that at AGS. Thus, the reduction of $< \beta_t >$ at SPS dose not contradict the picture of the QGP formation in Pb+Pb collisions at 158 A GeV, which is indicated by the recent observation of anomalous J/Ψ suppression and low-mass dilepton enhancement.

Contents

Acknowledgments

I would like to express my great appreciation to Prof. Y. Miake for his introducing me to the exciting field of physics. His appropriate and valuable advice show me the way to promote the present work, and I could learn a lot from him as an experimental physicist. I express my thanks to Prof. K. Yagi for his encouragement to complete this work.

I wish to express my thanks to Dr. K. Kurita for leading me to the E866 experiment. His appropriate and kind advice helped me a lot to accomplish this work. I appreciate Dr. Y. Akiba for his useful advice and discussions in the data analysis and for his hospitality. I express my special thanks to Dr. K. Shigaki for his advice on this work and for his friendship at BNL. I would like to express my appreciation to Prof. S. Nagamiya for his continuous encouragement.

I wish to express great thanks to Prof. C. Chasman for his gladly accepting me as a member of the E866 collaborator and for his guidance and hospitality as the group leader of Heavy Ion Research Group at BNL and the co-spokes person of the E866 experiment. I appreciate Dr. H. Hamagaki, the co-spokes person of the E866, for his stimulate advice. I express great thanks to all the collaborators of the E866 experiment. I owe Dr. J. H. Lee for his appropriate advice in HBT analysis and data reductions, Dr. K. Ashktorab for his help and advice. I wish to express thanks to Ms. E. Kim for her extensive calibration of the drift chambers and data reductions.

Here I acknowledge all the members of the high energy nuclear physics group at University of Tsukuba. I would like to thank Dr. A. Kumagai for his help in the data analysis, especially the FTOF calibration part. I would like to appreciate to Dr. H. Sako, who gave me useful advice on many aspects of the analysis. I express my thanks to Dr. S. Nishimura for useful discussion of HBT analysis and valuable advice. I express my thanks Dr. M. Nishimura, Mr. S. Sato, Mr. S. Kato and Dr. K. Enosawa for their friendship and discussions on the present work. I appreciate Mr. Y. Okuma, Mr. Y. Yokota, Ms. Y. Miyamoto and Ms. R. Higuchi for their

encouragement and friendship. I appreciate Mr. A. Kiyomichi, Mr. T. Hirano, Mr. T. Yoshikawa, Ms. M. Suzuki, Mr. K. Koseki, Ms. M. Aizawa, Mr. D. Hakozaki, Mr. Y. Akutsu, Mr. M. Ono, Mr. N. Maeda and Mr. H. Tsuruoka for their friendship and kindness.

This work is supported in part by the U.S. Department of Energy under contracts with ANL, BNL, the University of California at Riverside, Columbia University, LLNL, and MIT, in part by NASA under a contract with the University of California, by the U.S.-Japan High Energy Physics Collaboration Treaty, Grant-in-Aid for Scientific Research (Specially Promoted Research and International Scientific Research) of the Ministry of Education, the University of Tsukuba Special Research Projects, and by the Research Fellowships of the Japan Society for the Promotion of Science for Young Scientists.

Finally, I would like to express my great appreciation to my parents for their support and encouragement to accomplish this work.

Chapter 1

Introduction

In this chapter, the physics of high energy heavy-ion collisions are introduced. After reviewing new results observed at CERN-SPS, we present the thesis motivation.

1.1 Physics of High Energy Heavy-Ion Collisions

Heavy-ion collisions at high energies ($E/m \gg 1$) offer an unique opportunity to probe highly excited dense nuclear matter in the laboratory. The driving force for such studies both on experimental and theoretical side, is the expectation that a entirely new form of nuclear matter may be created from relativistic heavy-ion reactions. That form of matter is called the quark-gluon plasma (QGP), which is quantum chromodynamics (QCD) analogue of the plasma phase of ordinary atomic matter.

According to the lattice QCD calculations, it is predicted that the phase transition from hadronic phase to QGP phase occurs at energy densities $\epsilon \approx 2$ GeV/fm^3, corresponding to a critical temperature $T_c = 140 \sim 200$ MeV in baryon-free matter [1, 2]. Fig. 1.1 shows the schematic phase diagram of strongly interacting matter. As the diagram shows, it is expected that a QGP phase transition occurs at a high temperature and/or a high baryon density.

In order to understand the properties of the nuclear matter under the extreme conditions and hopefully to capture the signal of QGP formation, various experiments have been taken place both at the Alternating Gradient Synchrotron (AGS) at Brookhaven National Laboratory (BNL), and the Super Proton Synchrotron (SPS) at CERN. In the near future, the Relativistic Heavy Ion Collider (RHIC) at BNL and

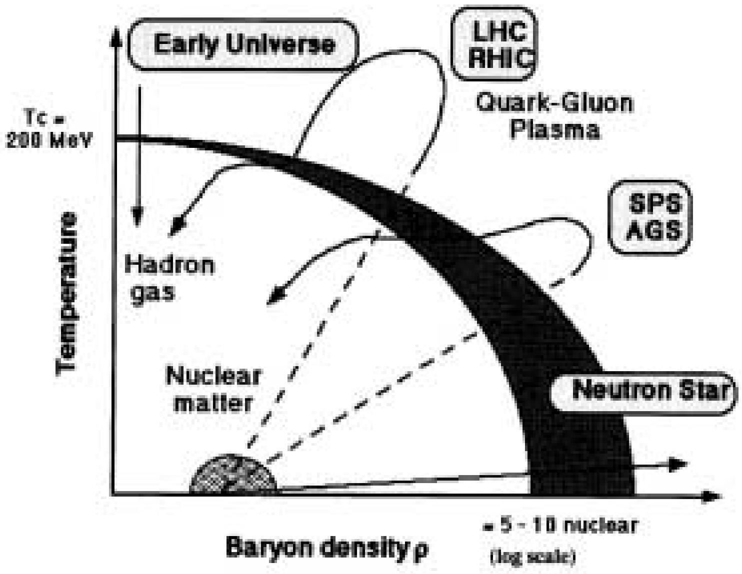

Figure 1.1: The phase diagram of strongly interacting matter, showing the hadronic phase at low temperature and baryon density, the mixed phase (transition region) and the QGP phase. The curves and lines illustrate possible trajectories in supernovae explosions, Big Bang evolution, and in heavy-ion reactions at present (AGS and SPS) and future (RHIC and LHC) accelerators. This picture was produced by LHC-ALICE Collaboration.

the Large Hadron Collider (LHC) at CERN will be operated. Table 1.1 shows the list of current and proposed facilities dedicated to accelerations of heavy-ion beams.

1.1.1 Signatures of the quark gluon plasma

Unlike such ordinary plasmas, however, the deconfined quarks and gluons of a QGP can not be observed directly because of the fundamental confining property of the physical QCD vacuum. What we can observe is hadronic and leptonic remnants of the transient QGP state or hadronic gas state. In order to catch the signals of QGP formation, a variety of probes are proposed. As the distinct signature of the existence of QGP is still under the study, the best way to prove the presence of a QGP phase is to measure several signatures simultaneously. Recent reviews of the possible QGP signatures and experimental status can be found in the literatures [3, 4]. The signatures can be categorized in terms of deconfinement, chiral symmetry restoration and collectivity.

Accelerator	Location	Ion beam	Momentum [A · GeV/c]	$\sqrt{s}$ † [GeV]	Commissioning date
AGS	BNL	^{16}O, ^{28}Si	14.6	5.4	Oct. 1986
		^{197}Au	11.4	4.8	Apr. 1992
SPS	CERN	^{16}O, ^{32}S	200	19.4	Sep. 1986
		^{208}Pb	158	17.4	Nov. 1994
RHIC	BNL	^{197}Au	100	200	Spring 2000
LHC	CERN	^{208}Pb	3150	6300	2005 (project)

Table 1.1: List of current and proposed facilities, the ion beams, the corresponding beam momentum and the center of mass energy. († per nucleon-nucleon pair for a symmetric colliding system.)

(1) Deconfinement

In QGP phase, quarks and gluons are not confined to hadrons but move freely in significantly large volume. In such deconfined medium, long range term of quark potential is expected to be suppressed due to the screening by surrounding quarks. Such effect in electromagnetism is known as Debye screening and the reduced range of potential is characterized by Debye radius. Application of Debye screening effect to the QCD was proposed as a signature of QGP formation by Matsui and Satz [5, 6] in 1986. If radius of a meson is larger than the Debye radius, which is determined by the plasma temperature and density, the meson cannot survive in the plasma. It is proposed that J/Ψ meson made of $c\bar{c}$ quarks is suitable for the detection of Debye screening effect because of the following reasons; 1) as J/Ψ is leptonic decay object, decay products do not interact strongly with other hadrons, thus it is expected penetrative probe for the early stage of the collisions, 2) J/Ψ's are produced in the very early stage of the collision, 3) hadronic interaction of J/Ψ is expected to be not too high ($\sigma_{\Psi N} \sim 6$ mb), thus it has the information of initial state condition of the collisions.

As discussed in 1.2.1, J/Ψ suppression effect is indeed observed in Pb+Pb collisions at the energy of 158 GeV per nucleon [7]. It is highly controversial whether it can be interpreted as "true" signal of QGP formation.

(2) Chiral symmetry restoration

At low temperature, the QCD vacuum is characterized by non vanishing density of virtual quark - anti quark pairs and broken chiral symmetry. At high temperature, not only the deconfinement phase transition takes place, but the chiral symmetry is expected to be restored.

Particle mass is determined by its interaction in the medium. The mass of meson is expected to be modified in high density and high temperature in the medium. This phenomenon is closely related to the restoration of chiral symmetry of the QCD.

Mass of vector mesons have been proposed as a probe of the chiral symmetry restoration. One of the important proposal is detection of the change of ρ meson mass, which is expected to dominate at the low-mass region of dilepton spectrum. As discussed in 1.2.2, strong enhancement in the low-mass region of di-electron spectra are reported in Pb+Au collisions at CERN-SPS [9, 10]. But the same enhancement has been also observed in S+Au collisions, this is the one of the hot subject to interpret the results.

(3) Collision dynamics and equation of state

Study of collective motion of produced hadrons in final state is expected to provide information on the dynamics of heavy ion collisions. With a hydrodynamical view of collisions, collective motion is governed by a pressure gradient of compressed nuclear matter at the early stage of collision. In the case of a phase transition from the ordinal nuclear to the quark gluon plasma, it is expected that the equation of state should exhibit a corresponding softening due to the increased number of degrees of freedom [11]. Thus, the observation of collective motion is crucially important to validate the hydrodynamical description of dynamics.

If the phase transition is the first order, the equation of state will be "softest" at the critical temperature T_c. Such softening is expected to affect the dynamic evolution of the system because the internal pressure drops at T_c. Thus an observation of excitation function of the transverse collective flow can be a probe for the QGP formation; drop in the excitation function of collective flow indicates threshold energy of the QGP formation.

1.2 Features Observed in Heavy Ion Collisions at the Energy of 158 A GeV

Based on the motivation to create QGP in the laboratory, lead ion beams at the energy of 158 GeV per nucleon are accelerated at CERN-SPS. Several interesting features of the observation have been reported, among which are the suppression of J/Ψ production in Pb+Pb collisions, the enhancement of low mass lepton pairs and the collective behavior of hadron production. These features have been interpreted as signatures of QGP formation under the key words of deconfinement, chiral restoration and collectivity, although clear conclusion has not been made yet.

1.2.1 J/Ψ suppression

As we mentioned in 1.1.1, the formation of the $c\bar{c}$ bound states would be suppressed in the QGP due to the screening of the attractive color force which binds the two quarks together. Charmonia are produced in the very early stage of the collision. Strongly bound states, like the J/Ψ, are expected to interact weakly with other hadrons. As a result, and more than other signatures, J/Ψ suppression have its original information through the different stages of the reacting medium.

Recently, NA50 collaboration have been reported the anomalous J/Ψ suppression in central Pb+Pb collisions at 158 A GeV [7]. Fig. 1.2 shows the ratio of the J/Ψ to the Drell-Yan cross-sections divided by the exponentially decreasing function accounting for normal nuclear absorption. The horizontal axis is the mean nuclear path length L. In this figure, the J/Ψ cross-section measured for peripheral Pb+Pb collisions agrees with the general pattern determined from proton, oxygen and sulphur-induced reactions which can be accounted for by nuclear absorption. On the other hand, in central collisions a clear departure from the pattern of the nuclear absorption is observed and is claimed as an anomalous J/Ψ suppression. This experimental finding can be considered as a strong indication of the production of a QGP phase in central Pb+Pb collisions [7].

1.2.2 Low-mass dilepton enhancement

Since leptons interact only electromagnetically and their mean free path is considerably larger than the size of the collision volume, the production of lepton pairs is

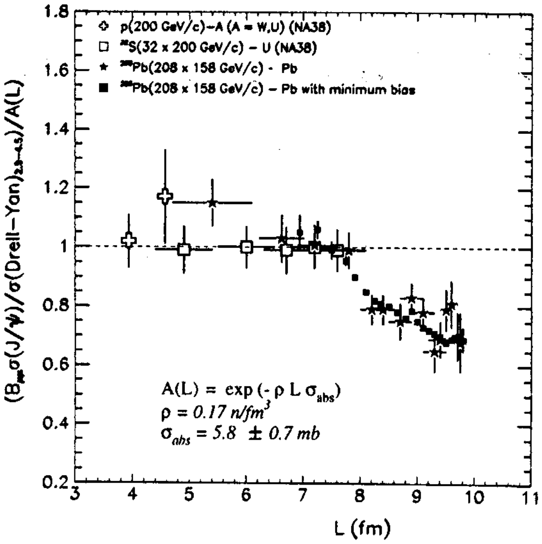

Figure 1.2: The ratio of the J/Ψ to the Drell-Yan cross-sections ($\sigma_{\mathrm{J}/\Psi}/\sigma_{\mathrm{DY}}$) divided by the exponentially decreasing function accounting for normal nuclear absorption [7]. The horizontal axis is the mean nuclear path length L.

commonly accepted as a promising probe to study the dynamical evolution of nuclear collisions [8]. They are created during the entire space-time evolution of the system, beginning at the early hot stage up to the point where the hadrons cease to interact. Because of this penetrative properties, the production of dileptons reflects the initial temperature of the system and the matter created in the reactions, i.e., a QGP through quark annihilation ($q\overline{q} \rightarrow l^+l^-$) or a high density hadron gas through pion annihilation ($\pi^+\pi^- \rightarrow l^+l^-$).

The CERES/NA45 Collaboration have been carried out the systematic study of $\mathrm{e}^+\mathrm{e}^-$ pair productions in low-mass region at CERN energies with proton, S and Pb beams. Fig. 1.3 shows the inclusive $\mathrm{e}^+\mathrm{e}^-$ mass spectrum in Pb+Au at 158 A GeV [9]. The data compared to the sum of the expected contributions from hadron decay (solid curve). It is observed the enhancement at low-mass region in the spectrum compared to the contributions from hadron decay.

This dielectron spectrum at the SPS energy seems explainable in hydrodynamic approach assuming the creation of a thermalized QGP [12]. On the other hand, the same data can be reproduced in the framework of microscopic hadronic transport models incorporating mass shifts of vector mesons [13, 14].

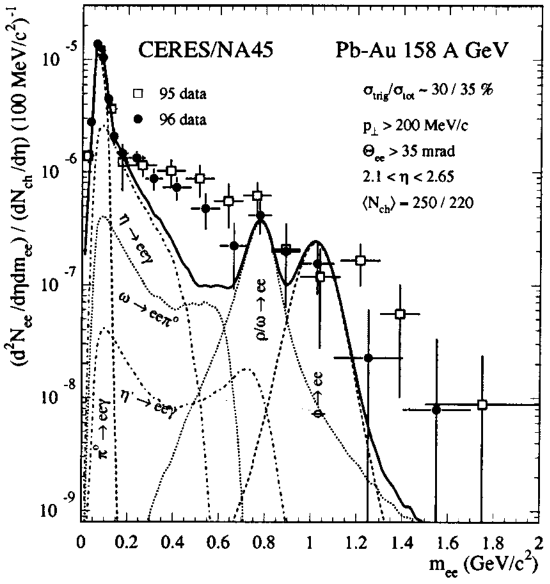

Figure 1.3: Inclusive e^+e^- mass spectrum in Pb+Au collisions at 158 A GeV normalized to the observed charged-particle density [9]. The data compared to the sum of the expected contributions from hadron decays (solid curve).

1.2.3 Collective behavior

Transverse collective expansion is expected to be more prominent in the heavy ion collision than in that of lighter projectiles, owing to the smaller surface-to-volume ratio, the larger “fireball” volume and the longer duration of expansion. Such indication can be visible in the single particle transverse mass spectra. The measured distributions can be reproduced by invoking a radial velocity field in transverse direction with a temperature at freeze-out stage. But the single particle spectra alone can not distinguish between an elevated temperature and a boost due to transverse collective expansion, because of the strong anti-correlation between transverse flow velocity β_t and temperature T in the model. To avoid its uncertainty, the combination of single particle spectra with two-particle correlation results can resolve this essential ambiguity and determine β_t and T uniquely.

Recently the simultaneous analysis of single particle spectra and two particle correlation function have been reported by the NA49 experiment in central Pb+Pb collisions at 158 A GeV [17]. In the analysis, The correlation functions for negative hadrons have been fitted with the Yano-Koonin-Podgoretskii (YKP) parameterization [15] as formulated by Heinz [16] and the extracted source parameters have been

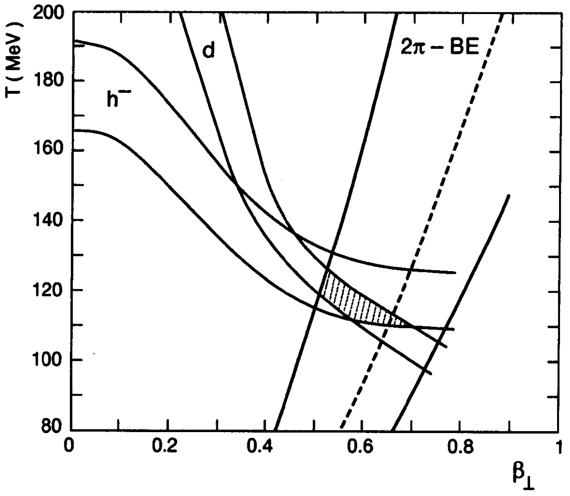

Figure 1.4: Allowed regions of freeze-out temperature T vs. transverse velocity β_t for central Pb+Pb collisions near mid-rapidity [17]. The boundaries are derived from negative hadron two-particle correlation functions and from negative hadron and deuteron transverse mass spectra within the framework of the expanding source model. Contours are drawn at $\pm\sigma$ around fitted values.

studied as a function of rapidity and transverse momentum of the pair.

In the framework of an expanding hadronic source model, the analysis of correlation functions yields information about the source size and the duration of the freeze-out process, as well as the ratio β_t^2/T, where β_t is the transverse velocity and T is the freeze-out temperature. The ambiguity between temperature and expansion velocity implicit in the ratio can then be lifted by considering single particle spectra. Fig. 1.4 shows the allowed regions of freeze-out temperature vs. transverse velocity for central Pb+Pb collisions near mid-rapidity. The boundaries are derived from two-particle correlation functions for negative hadrons and from negative hadron and deuteron transverse mass spectra within the framework of the expanding source model. Contours are drawn at $\pm\sigma$ around fitted values. In the paper [17], they conclude that both features of single particle spectra and the average pair transverse momentum K_T dependence of two-particle correlations can be described by $T = 120 \pm 12$ MeV and $\beta_t = 0.55 \pm 0.12$ at CERN-SPS energy.

1.3 Thesis Motivation

As reviewed in the previous section, it is claimed that the signals of the QGP formation emerge at 158 GeV per nucleon with lead ion beams. To understand the validity of QGP formation in Pb+Pb collisions at CERN-SPS, however, it is important to investigate whether not only a single but also several signals could be explained simultaneously by a consistent model. Furthermore, since transverse expansion velocity β_t and temperature T at freeze-out are the most fundamental values to characterize the system created in the reactions, the observation of these parameters at lower beam energy, for example at AGS, and comparisons of extracted (β_t, T) at the two different energies can provide the important input about the question of QGP formation at SPS energy. From this point of view, the simultaneous analysis of single particle spectra and two-particle correlation at AGS energy can be considered as a suitable experimental observable both for the consistency of the picture of expansion and the evolution of the system from AGS to SPS energy.

In this thesis, we present the results of single particle spectra in Au+Au collisions at the energy of 4 and 11 A GeV, and the first results of high statistic $\pi^+\pi^+$ two-particle correlations in Yano-Koonin Podgoretskii (YKP) parameterization in Au+Au collisions at 11 GeV per nucleon, measured by the E866 experiment using the Alternating Gradient Synchrotron (AGS) at Brookhaven National Laboratory (BNL). Within the framework of the expanding source model, β_t and T are extracted from the two different analysis, then these results are compared to that of other beam energies.

The thesis is organized as follows: Chapter 2 describe the features of relativistic heavy ion collisions, particular emphasis on the single particle spectra and two particle correlation at AGS energy. Chapter 3 describes the experimental setup, Chapter 4 gives the run condition, Chapter 5 gives calibrations of detectors, particle identification and corrections. In Chapter 6, the experimental results of single particle spectra and in Chapter 7, that of two particle correlations are presented. In Chapter 8, it is discussed the transverse velocity field and freeze-out temperature using the finite expanding source model. Finally, conclusions are made in Chapter 9.

1.4 Contributions of Author

The author has contributed to AGS-E866 experiment as following.

- Calibrated the Time Projection Chambers and the Time-of-Fight counter.
- Analyzed the single particle spectra at 4 A GeV beam energy and published the results [18].
- Analyzed single particle spectra and two-particle correlations at 11 A GeV beam energy.

Chapter 2

Relativistic Heavy Ion Collisions

In this chapter, participant-spectator picture are introduced for the understanding of global features of relativistic heavy-ion collisions. Next, we review the results of single particle spectra and its interpretations at AGS energies. For two-particle correlation, the formalism of HBT, existing experimental results and its understanding are shown. Finally, simultaneous interpretation of single particle spectra and HBT with radial flow model are presented.

2.1 Participant-Spectator Picture

Nuclei are extended objects, and therefore their geometry plays an important role in heavy ion collisions. Fig. 2.1 shows a sketch of reaction at a high energy between symmetric Lorentz contracted nuclei in the center of mass frame. The impact parameter b separates the nucleons into *participants* with primary nucleon-nucleon collisions, and *spectators*, which proceed with little perturbation along the original direction. The use of this clear cut geometry between spectators and participants is justified by the fact that at very high energies the size of nucleons is larger than their Compton wavelength and the nuclear radius is larger than the interaction length of ≈ 1.8 fm. Cross sections, number of participants and related kinematic quantities are usually calculated from simple geometrical considerations [19].

Based on Participant-Spectator picture, the centrality of the Au+Au collision are defined by the measurements of the energy deposition of the calorimeter located at zero-degree in the beam direction (see Section 6.3).

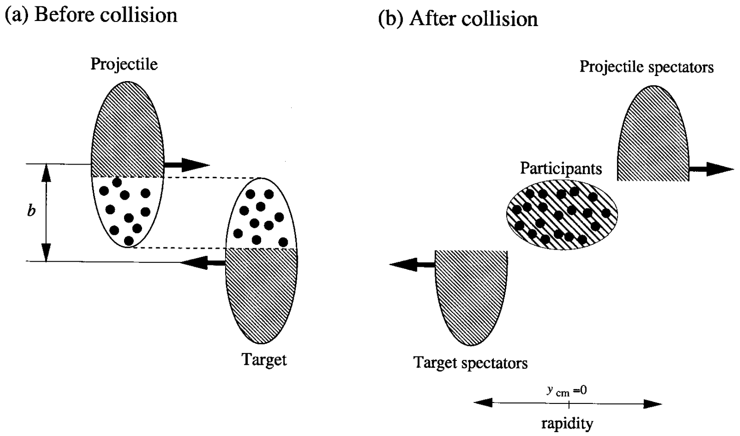

Figure 2.1: Participant-Spectator picture of a high energy heavy-ion collision with impact parameter b. On the left (a), the two incoming nuclei in the center of mass frame are shown. On the right (b), after the collision, the nucleons are separated to participants, projectile spectators and target spectators.

2.2 Single Particle Spectra at AGS Energies

Single particle spectra, i.e., transverse momentum p_t distributions are often used to study the properties of hadrons at the freeze-out stage. The term of freeze-out refers here to the final decoupling of hadrons from the strong interaction. In this section, previous experimental results of single particle spectra in proton-nucleus (pA) collisions and nucleus-nucleus (AA) collisions at AGS energies are reviewed.

2.2.1 m_t spectra in p+A collisions

Transverse momentum spectra are usually presented in terms of the invariant differential cross section,

$$E\frac{d^3\sigma}{dp^3} = \frac{1}{2\pi p_t}\frac{d^2\sigma}{dp_t dy} = \frac{1}{2\pi m_t}\frac{d^2\sigma}{dm_t dy}, \tag{2.1}$$

where p_t is the transverse momentum, y is the rapidity, $m_t = \sqrt{p_t^2 + m_0^2}$ is the transverse mass and m_0 is the rest mass of the particle. The use of the transverse mass is suggested by the experimental fact that the cross section of given particle species in proton-proton collisions is better described by an exponential in m_t rather than p_t [20]. The spectra shape and even the absolute cross sections of different mass particles are similar when plotted as a function of m_t [4]. This observation leads to the notion of "m_t *scaling*". For parameterizations of the invariant cross section, the inverse slope parameter T_0 is used as,

$$E\frac{d^3\sigma}{dp^3} \propto \exp\Bigl(-\frac{m_t}{T_0}\Bigr). \tag{2.2}$$

A number of theoretical explanations have been proposed for m_t scaling [21, 22, 23], often assuming a local thermal equilibrium and the inverse slope parameter T_0 as temperature.

In a model of purely thermalized system, the transverse mass spectrum is obtained by integrating over rapidity using the modified Bessel function K_1, which behaves asymptotically like a decreasing exponential [22]:

$$\frac{1}{m_t}\frac{dN}{dm_t} \sim m_t K_1\Bigl(\frac{m_t}{T_0}\Bigr) \tag{2.3}$$

$$\frac{1}{m_t}\frac{dN}{dm_t} \approx \sqrt{m_t}\exp\Bigl(-\frac{m_t}{T_0}\Bigr) \qquad \text{for} \qquad \frac{m_t}{T_0} \gg 1. \tag{2.4}$$

At the AGS energy, transverse mass spectra for $\pi^{\pm}$, $K^{\pm}$ and protons have been measured by E802 experiment in p+Be and p+Au reactions at 14.6 GeV/c close to mid-rapidity (y = 1.2-1.4). Within the p_t range covered by the experiment, the spectra have a single exponential shape as a function of m_t in both p+Be and p+Au reactions as shown in Fig 2.2 [24]. And all these spectra are almost in parallel, i.e., roughly the same inverse slope parameter. In Fig. 2.3, the inverse slope parameters, extracted by the fitting in the single exponential function for the spectra in p+Be, p+Au and central Si+Au system are summarized. The extracted slopes are 140 $\sim$ 160 MeV for $\pi^{\pm}$, $K^{\pm}$ and protons in proton induced reactions. Thus, so called "m_t scaling" is seen at p+p and p+A reactions at the AGS energy.

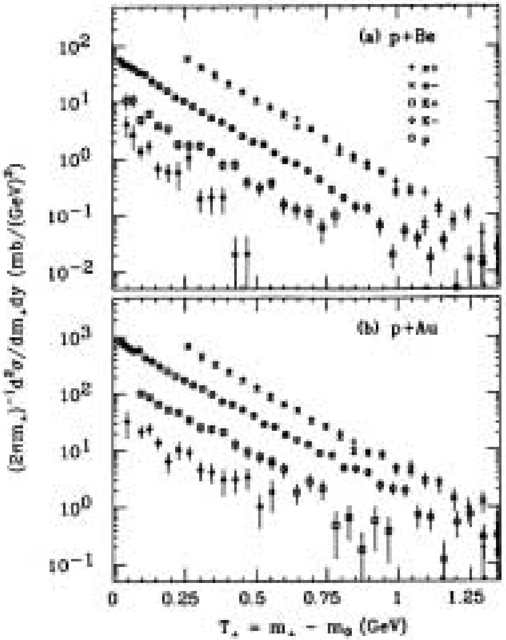

Figure 2.2: Invariant cross sections as a function of transverse kinetic energy $m_t - m_0$ for $\pi^\pm$, $K^\pm$ and protons in (a) p+Be and (b) p+Au collisions at the beam momentum of 14.6 A GeV/c [24]. The rapidity range is $1.2 \leq y \leq 1.4$.

2.2.2 m_t spectra in A+A collisions

In contrast to pA reactions, m_t spectra in nucleus-nucleus central collisions at mid-rapidity do not scale in the same inverse slope parameter for all particle species.

Fig. 2.4 shows the particle mass dependence of inverse slope parameters in p+Au, Si+Al (central) and Au+Au (central) collisions at AGS energies. A distinct difference of the inverse slope parameters between pA and AA system can be seen. While the inverse slope parameter in p+Au system remain almost constant $T_0 \simeq 150$ MeV as a function of particle mass, the parameters in AA system increase as a function of the mass. Furthermore, for a given mass, the heavier the colliding system, the higher the inverse slope parameter.

Fig. 2.5 shows the invariant cross section for pions and proton at mid-rapidity in Au+Au central collisions at 11.6 A GeV/c [25]. The proton spectrum has visibly convex shape at low m_t region ($m_t - m_0 \leq 0.3$ GeV/c^2). Unlike the measured spectra in p+A and Si+A at similar incident energy presented above, the proton spectrum in Au+Au reactions cannot be described by a single exponential function. On the other hand, $\pi^\pm$ spectra show strong rise at low m_t region, and therefore these spectra

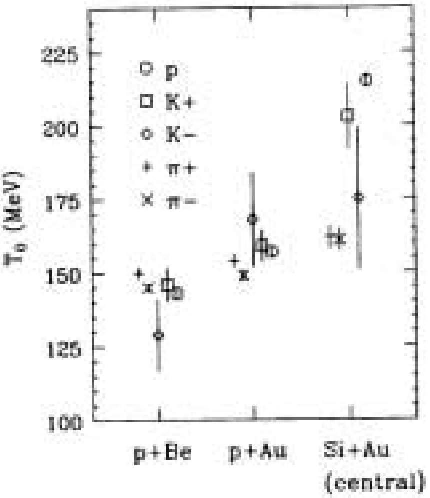

Figure 2.3: Comparison of inverse slope parameters T_0 in p+Be, p+Au and central Si+Au collisions [24]. Inverse slope parameters are obtained by exponential fits with the invariant cross section.

also cannot describe in the single exponential function. The rise of $\pi^{\pm}$ spectra at low m_t might be attributed to, in part, by the decay of resonances, e.g., Δ which tend to produce relatively low momentum pions, and in part by the collective flow phenomenon. The shape of $K^{\pm}$ spectra in these reactions have the single exponential shape [26].

In summary, three important qualitative features in AA collisions can be listed as following.

1. For a given collision system, the inverse slope parameter T_0 is a function of the particle mass, i.e., the heavier the particle, the higher T_0.
2. The values of T_0 is larger for heavier collision systems.
3. The deviation from the single exponential shape in the spectra for protons and pions.

At the next subsection, it will be shown that these features in AA collision system are qualitatively explained by introducing a transverse velocity field in the created system.

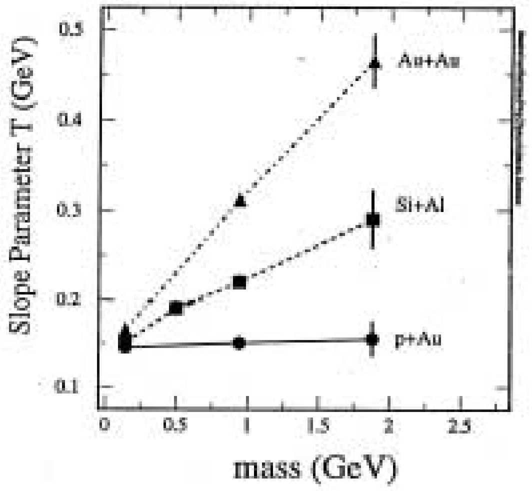

Figure 2.4: Inverse slope parameters as a function of particle mass in p+Au, Si+Al (central) at 14.6 A GeV/c and Au+Au (central) at 11.6 A GeV/c (E802 data).

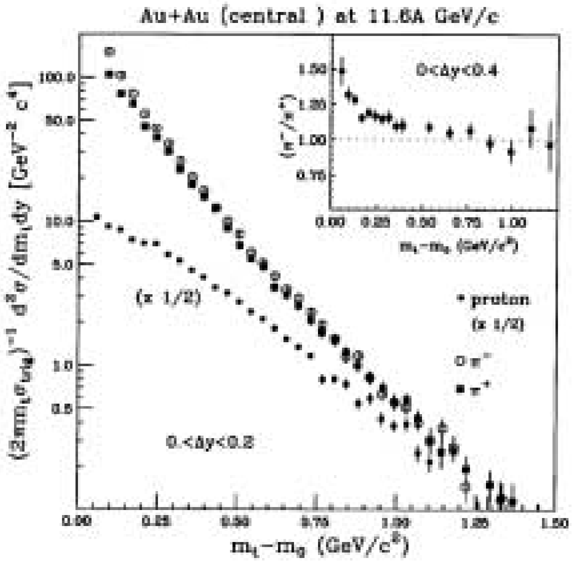

Figure 2.5: Invariant cross section for pions and protons at the mid-rapidity as a function of transverse kinetic energy $m_t - m_0$ in Au+Au central collisions at 11.6 A GeV/c [25]. The data for protons (solid points) is scaled by a factor of 0.5. The open circles are the data for π^- and the solid squares are that for π^+. The inset shows the ratio of π^-/π^+ as a function of $m_t - m_0$.

2.2.3 Interpretation with radial flow model

Most successful description of the different slope parameters and the change of shape observed in m_t spectra in AA collisions is given by the model including the transverse expanding velocity field together with a moderate temperature of a thermalized system. With the presence of the transverse velocity field, the mass dependence of inverse slope parameters can be understood qualitatively as follows.

In case of a purely thermal motion, all particles (irrespective of their mass) would move with the same average kinetic energy determined by the temperature, i.e.,

$$< E_{\mathrm{kine}} > \sim T_{\mathrm{thermal}}. \tag{2.5}$$

On the other hand, in case of a purely collective motion, all particles would move with the same velocity β_c and consequently, the average kinetic energy would increase proportional to their mass m_0, since

$$< E_{\mathrm{collective}} > \sim \frac{m_0 \beta_c^2}{2}. \tag{2.6}$$

Under the assumption of complete decoupling between the thermal and collective motion of the particle, superpositions of both types of motion will give the mass dependence of;

$$\begin{aligned} < E_{\mathrm{kine}} > &= < E_{\mathrm{thermal}} > + < E_{\mathrm{collective}} > \qquad (2.7) \\ &= T_{\mathrm{thermal}} + \frac{m_0 < \beta_t >^2}{2}, \end{aligned}$$

where $< \beta_t >$ is the averaged collective velocity for all particle species. The inverse slope parameter T_0 is proportional to the average transverse kinetic energy and is given as,

$$T_0 \propto T_{thermal} + m_0 \cdot < \beta_t >^2 . \tag{2.8}$$

Furthermore, because of this velocity dependence, for heavier collision system, which presumably stronger collective transverse flow, the value of T_0 is expected to be larger. The above observations are thus qualitatively consistent with the hypothesis of transverse hydrodynamic flow produced in the heavy-ion collisions. Quantitatively, the phenomenological hydrodynamical model proposed by Schnedermann et. al. [27]

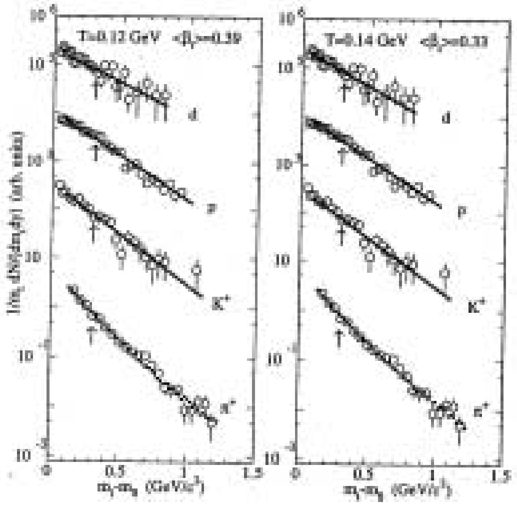

Figure 2.6: Deuteron, proton, K^+ and π^+ spectra in Si+Au at 14.6 A GeV/c (E802 data [28]) at $y = 1.3$ compared to calculated spectra including transverse expansion of the source at temperature T [29]. Dashed lines are the spectra of a source at $T =$ 120 MeV expanding transversely $< \beta_t > = 0.39$ (left) and a source at $T = 140$ MeV and $< \beta_t > = 0.33$ (right). The arrows indicate the lower limit of the fit region.

can be applied to the single particle spectra for the extraction of transverse velocity and temperature at freeze-out.

In this model, collective flow effects are incorporated into transverse mass spectra as following:

$$\frac{\mathrm{d}N}{m_t \mathrm{d}m_t} \propto \int_0^R r\mathrm{d}r m_t I_0(\frac{p_t \sinh(\rho)}{T}) K_1(\frac{m_t \cosh(\rho)}{T}), \tag{2.9}$$

where modified Bessel function I_0 and K_1, a parameter $\rho = \tanh^{-1}(\beta_t)$ and a transverse velocity profile of $\beta_t(r) = \beta_t^{max}(r/R)^\alpha$. In the above equation, the parameter T is interpreted as a temperature at freeze-out stage in the model.

Fig. 2.6 shows the fitting results by the hydrodynamical flow model in central Si+Au data at 14.6 A GeV/c near mid-rapidity. Dashed lines are the spectra of a source at T = 120 MeV and $< \beta_t > = 0.39$ (left) and a source at T = 140 MeV and $< \beta_t > = 0.33$ (right). As show in Fig. 2.6, all the particle spectra from pions to deuterons are shown to be reproduced very well with two parameters, T and β_t. Problem with this fitting is, however, no unique parameter set for (β_t, T); there is strong correlation between β_t and T and it is difficult to determine the unique set of parameter without ambiguity from single particle spectra alone.

2.3 Two Particle Correlation

In addition to single particle spectra of hadrons, two particle correlation of identical particle provides information on the space-time evolution of the system created in heavy-ion collisions at freeze-out [1] .

In a pioneering experiment in 1956, Hanbury-Brown and Twiss measured the angular diameter of a star using the correlation between two photons [30]. Their ideas have been applied to subatomic physics to measure source sizes using different types of particles. The phenomenon of the space-time correlation or the energy-momentum correlation of detected identical particles emitted from an extended source is known as the Hanbury-Brown and Twiss (HBT) effect. HBT effect originates from the symmetrization of the wave function of bosons (Bose-Einstein correlation), or anti-symmetrization for fermions (Fermi-Dirac correlation). In the following subsections, the formalism of two particle correlation function for identical bosons [31], the transverse momentum dependence of source size extracted by HBT measurements and the effect of the expanding source to the extracted source size are described.

2.3.1 Hanbury-Brown and Twiss (HBT) effect

We consider a source of identical bosons (see Fig. 2.7) and describe in plane waves. To calculate the two particle momentum distribution $P_2(p_1, p_2)$, we need the source density $\rho(x)$ in space-time, the random phase $\phi(x)$ of a boson emitted at x and the probability amplitude $A(p, x)$ for production of a boson of momentum p at x. The probability amplitude of detecting a boson of four-momentum p_1 at x'_1 and another boson of four-momentum p_2 at x'_2 which are emitted at x_1 and x_2, is given after symmetrization by:

$$\begin{aligned}
\psi_{12} &= \frac{1}{\sqrt{2}}\{A(p_1,x_1)e^{i\phi(x_1)}A(p_2,x_2)e^{i\phi(x_2)}e^{ip_1(x_1-x'_1)}e^{ip_2(x_2-x'_2)} \\
&\quad + A(p_1,x_2)e^{i\phi(x_2)}A(p_2,x_1)e^{i\phi(x_1)}e^{ip_1(x_2-x'_1)}e^{ip_2(x_1-x'_2)}\} \\
&\equiv e^{i\phi(x_1)+i\phi(x_2)}\Psi(p_1,p_2,x_1,x_2,x'_1,x'_2), \qquad (2.10)
\end{aligned}$$

where the particles are on-shell, $e^{ip_1(x_1-x'_1)}$ and the other similar terms describe the propagation of a particle. As we can not distinguish which points of the source

---

[1] Cease to interact strongly among hadrons in a reaction zone. The particle are emitted freely without final state interaction after freeze-out.

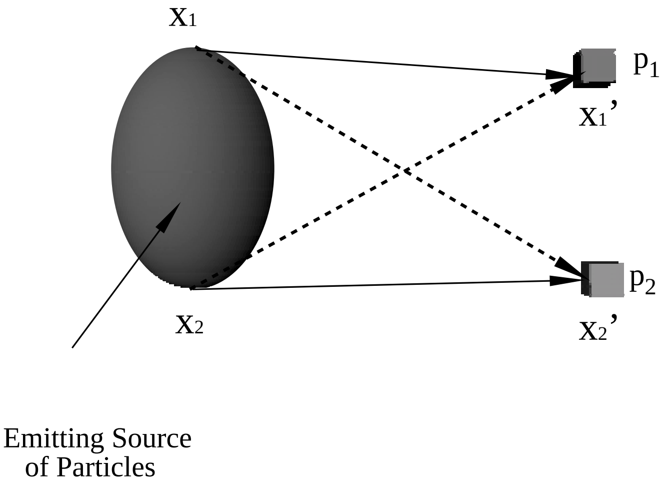

Figure 2.7: A boson of four-momentum p_1 is detected at the space-time point x_1' and another identical boson with four-momentum p_2 is detected at x_2'. They are emitted from the points x_1 and x_2 of an extended source. The solid lines joining x_1 to x_1' and x_2 to x_2' and the dashed lines joining x_1 to x_2' and x_2 to x_1' are possible trajectories for the bosons.

the detected bosons are coming from, we have to integrate the above probability amplitude over all pairs of points of the source. Then we have to take the modulus square to obtain the two-particle momentum distribution:

$$P_2(p_1,p_2) = \frac{1}{2!}\int d^4x_1 d^4x_2 d^4y_1 d^4y_2 \rho(x_1)\rho(x_2)\rho(y_1)\rho(y_2)|\psi_{12}|^2. \tag{2.11}$$

Due to the randomness of the phase ϕ, above integral is non-zero contribution only when $x_1 = y_1$ and $x_2 = y_2$ or $x_1 = y_2$ and $x_2 = y_1$. By using the symmetry of Ψ under exchange of x_1 and x_2 (Bose-Einstein statistics):

$$P_2(p_1,p_2) = \int d^4x_1 d^4x_2 \rho(x_1)\rho(x_2)|\Psi(p_1,p_2,x_1,x_2,x_1',x_2')|^2. \tag{2.12}$$

Using the definition of ψ_{12} in Eq. 2.10, we find:

$$\begin{aligned} P_2(p_1,p_2) \;&=\; \frac{1}{2}\int d^4x_1 d^4x_2 \rho(x_1)\rho(x_2)\{A^2(p_1,x_1)A^2(p_2,x_2) + A^2(p_1,x_2)A^2(p_2,x_1) \\ &\quad + A(p_1,x_1)A(p_2,x_1)e^{-i(p_1-p_2)x_1}A(p_1,x_2)A(p_2,x_2)e^{i(p_1-p_2)x_2} \end{aligned}$$

$$+ A(p_1, x_1)A(p_2, x_1)e^{i(p_1-p_2)x_1}A(p_1, x_2)A(p_2, x_2)e^{-i(p_1-p_2)x_2}\}. \quad (2.13)$$

After same renaming of the integration variables, we finally get:

$$P_2(p_1, p_2) = P_1(p_1)P_1(p_2)\Big(1 + \Big|\int d^4x e^{iqx}\rho_{\text{eff}}(x, p_1, p_2)\Big|^2\Big), \quad (2.14)$$

where

$$\begin{aligned} q &= p_1 - p_2, && (2.15)\\ P_1(p) &= \int d^4x f(p, x), && (2.16)\\ f(p, x) &= A^2(p, x)\rho(x) && (2.17)\\ \text{and} & && \\ \rho_{\text{eff}}(x, p_1, p_2) &= \frac{\sqrt{f(p_1, x)f(p_2, x)}}{\sqrt{\int d^4x_1 f(p_1, x_1)\int d^4x_2 f(p_2, x_2)}} = \frac{\sqrt{f(p_1, x)f(p_2, x)}}{\sqrt{P_1(p_1)P_2(p_1)}} && (2.18) \end{aligned}$$

$P_1(p)$ is the single-particle momentum distribution and $f(p, x)$ is the phase space distribution function.

The two-particle correlation function $C_2(p_1, p_2)$ is defined by the ratio of the probability of observing p_1 and p_2 in coincidence over to the probability of observing them separately:

$$C_2(p_1, p_2) \equiv \frac{P_2(p_1, p_2)}{P_1(p_1)P_1(p_2)} = 1 + |\tilde{\rho}_{\text{eff}}(q, p_1, p_2)|^2, \quad (2.19)$$

where

$$\tilde{\rho}_{\text{eff}}(q, p_1, p_2) = \int d^4x e^{iqx}\rho_{\text{eff}}(x, p_1, p_2) \quad (2.20)$$

is the Fourier transform of ρ_{eff}. Thus, the two particle correlation function $C_2(p_1, p_2)$ is directly related to the Fourier transform of the effective density, as given by Eq. 2.18. In many applications, one parameterizes the effective density in the form of a Gaussian distribution,

$$\rho_{\text{eff}}(x, p_1, p_2) = \frac{N}{4\pi^2 R_x R_y R_z \sigma_t}\exp\Big(-\frac{x^2}{2R_x^2} - \frac{y^2}{2R_y^2} - \frac{z^2}{2R_z^2} - \frac{t^2}{2\sigma_t^2}\Big), \quad (2.21)$$

where the normalization constant N and the standard deviations R_x, R_y, R_z and σ_t depend on p_1 and p_2. The constant coefficients in Eq. 2.21 are chosen in such a way that the effective density is normalized to

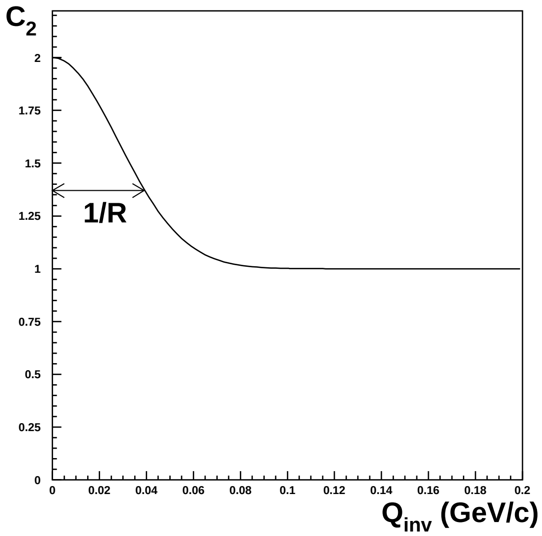

Figure 2.8: Two-particle correlation function of a source with $R_{inv} = 6$ fm and $\lambda = 1$ as a function of q_{inv}.

$$N(p_1, p_2) = \int d^4x \rho_{\text{eff}}(x, p_1, p_2). \tag{2.22}$$

We choose the collision axis as the longitudinal z-axis and we place the source center-of-mass at the spatial origin. The parameter R_z measures the longitudinal 'radius' of the source along the beam direction. R_x measures the transverse radius of the source along the direction towards the detectors and R_y measures the transverse radius of the source perpendicular to the line joining the source and the detector.

The Fourier transform of the effective source density Eq. 2.21 is

$$\tilde{\rho}_{\text{eff}}(q, p_1, p_2) = N \exp\Big(-\frac{R_x^2 q_x^2}{2} - \frac{R_y^2 q_y^2}{2} - \frac{R_z^2 q_z^2}{2} - \frac{\sigma_t^2 q_t^2}{2}\Big). \tag{2.23}$$

Finally, we get the correlation function for identical bosons in Gaussian parameterization by:

$$C_2(q) = 1 + N e^{-R_x^2 q_x^2 - R_y^2 q_y^2 - R_z^2 q_z^2 - \sigma_t^2 q_t^2}. \tag{2.24}$$

In one-dimensional case, correlation function is expressed as a function of q_{inv}:

$$C_2(q_{inv}) = 1 + \lambda e^{-R_{inv}^2 q_{inv}^2}, \tag{2.25}$$

where

$$q_{inv} = \sqrt{q_x^2 + q_y^2 + q_z^2 - q_0^2}, \tag{2.26}$$

where q_0 is the energy difference between two particles, and q_x, q_y and q_z are the momentum difference for each direction. Fig. 2.8 shows a typical two-particle correlation function of a source with $R_{inv} = 6$ fm and $\lambda = 1$ as a function of q_{inv}.

2.3.2 K_T dependence of source radius and its interpretation with radial flow model

Two particle correlations have been first used to study the properties of a hadron emitting system created in hadronic collisions under the assumption of a static source. The expansion of a source that is not static but exhibits a hydrodynamical scaling evolution has been discussed by Shuryak [32] and Bjorken [33]. Within the framework of such models, it has been further shown that the dependence of the correlation function on kinematic variables of the pion pair, such as average transverse momentum of pair K_T, is an important diagnostic tool for the study of an expanding system [34]-[40].

The E877 Collaboration has measured positively charged pion correlation as a function of the transverse mass of the pair as shown in Fig. 2.9 [41]. The transverse radii (R_T) are found to systematically decrease with increasing transverse mass of the pair and increasing rapidity of the pair. This behavior is consistent with the assumption of a collectively expanding system.

Fig. 2.10 shows the transverse mass of the pair $M_T(= \sqrt{K_T^2 + m_0^2})$ dependence of R_T parameter at mid-rapidity in the expanding source model [42]. Solid lines in the figure is for pion pairs and dashed lines is for kaon pairs in different transverse flow in terms of rapidity η_f. As shown in this figure, the decrease of R_T parameter with increasing K_T appear only if the β_t (or η_f) is non-zero. Thus the K_T dependence of R_T parameter can be a diagnostic probe to prove the existence of the transverse flow of the system.

2.4 Simultaneous Interpretation of Single Particle Spectra and HBT with Radial Flow Model

As shown in Section 2.2.3 and 2.3.2, existing results of both single particle spectra and two-particle correlations in Au+Au collisions at AGS energy are qualitatively consistent with the picture of expanding source.

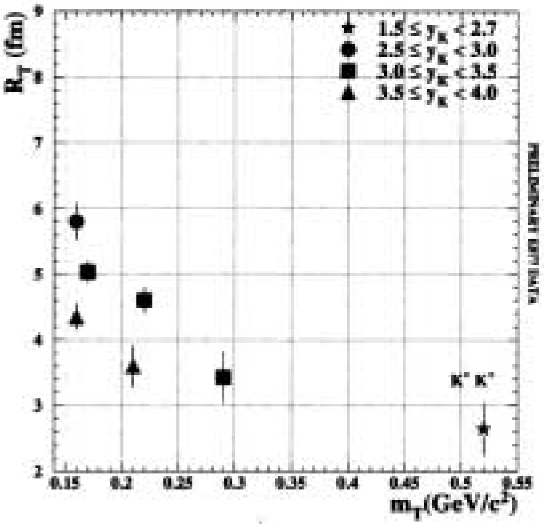

Figure 2.9: Transverse radius R_T from 2-dimensional $\pi^+\pi^+$ correlation as a function of the transverse mass of the pair, M_T for different rapidites from AGS-E877 preliminary data [41]. The data point from K^+K^+ correlations (star) is also shown.

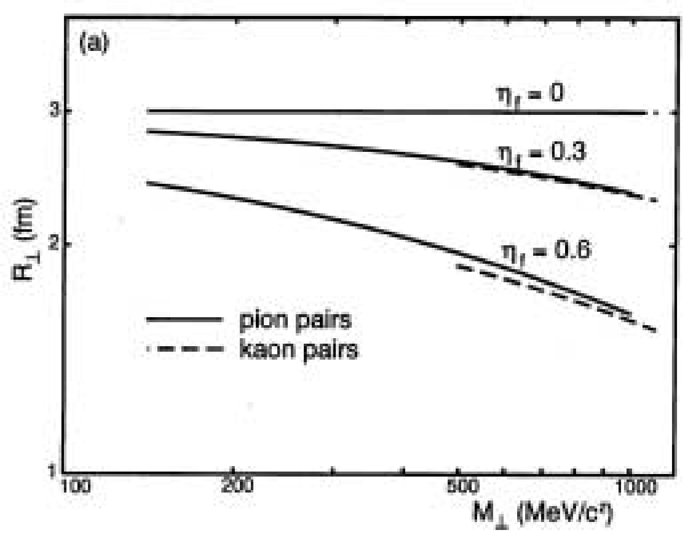

Figure 2.10: R_T as a function of the transverse mass of pair M_T at mid-rapidity of pair in the expanding source model [42]. Solid lines is for pions and dashed lines is for kaons in different transverse flow rapidity η_f.

Motivated by the such experimental observations, simultaneous analysis of single particle spectra and two-particle correlations using the finite expanding source is considered as one of the best way to access to the dynamical parameters, such as transverse velocity β_t and freeze-out temperature T of the system created in relativistic heavy-ion reactions. This simultaneous analysis can resolve the ambiguities between β_t and T of the source, that are unavoidable when single and two-particle spectra are analyzed separately.

At CERN-SPS energy, as we mentioned in Section 1.2.3, NA49 collaboration has measured both single particle spectra and two-particle correlations, and extracted the parameter set of β_t and T by the simultaneous analysis of both type of spectra using the finite expanding source model. The comparison of the (β_t, T) in the same analysis method at AGS with SPS energy is expected to shed light on the understanding of evolution of the collision dynamics with constancy of the model.

Chapter 3

The E866 Experimental Setup

The E866 experimental setup are described in this chapter. AGS accelerator facility, the global detectors, and spectrometer system are explained in each section.

3.1 Overview

In this chapter, the experimental setup of BNL-AGS-E866 experiment is described. Fig. 3.1 shows the plan view of the E866 experiment. We have adopted two-arm spectrometer system to cover the wide kinematic acceptance. The upper part with respect to the beam line in Fig. 3.1 is called the Henry Higgins spectrometer (HH), the lower part is the Forward Spectrometer (FS). In addition to these spectrometer system, the global detectors are equipped to determine the event geometry of the collision; the beam counter system (BTOT and HOLE), the zero-degree $\check{C}$erenkov counter (Bull's Eye), the zero-degree calorimeter (ZCAL), and the multiplicity counter (NMA). By using the apparatus, E866 experiment focus on the studies of systematic measurements of hadron production in Au+Au collisions at ~ 11 A GeV as described below [43].

1. To measure particle spectra as a function of rapidity and transverse momentum.
2. To study the dependence of these spectra on centrality of the collisions by utilizing the event characterization detectors.
3. To measure two particle correlations.

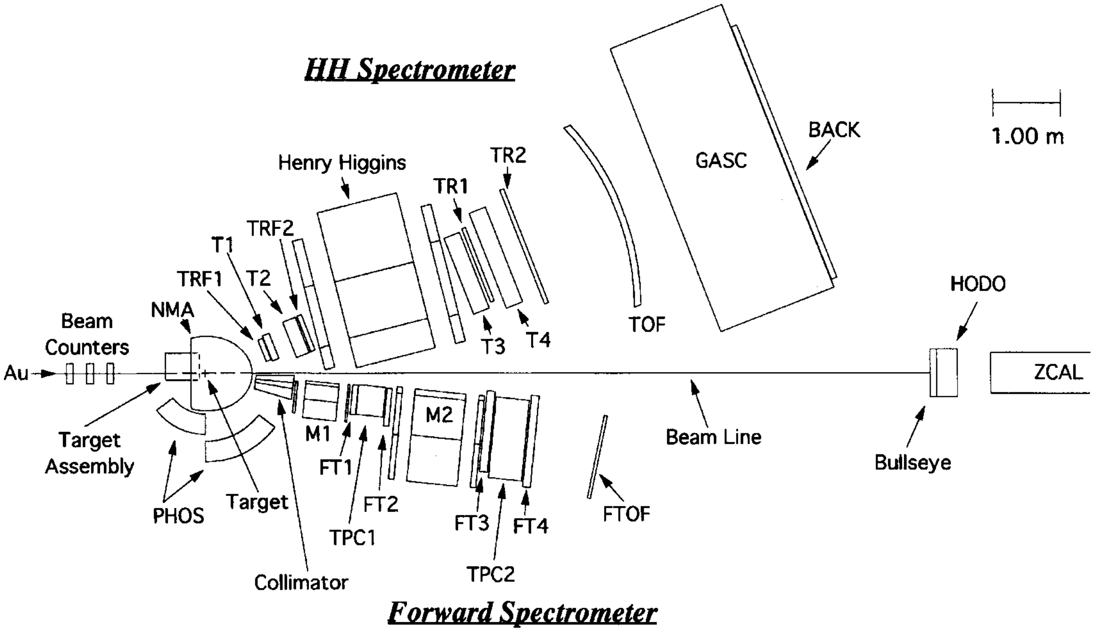

Figure 3.1: The plan view of the E866 spectrometer. The upper part with respect to the beam line is called the Henry Higgins spectrometer (HH), the lower part is the Forward Spectrometer (FS).

4. To look for systematic variations of cross sections with different beams and targets for understanding of the reaction dynamics.
5. To search an evidence for production of highly dense nuclear matter, or ultimately, the QGP.

In the following sections, features and specifications of above detectors are described. In section 3.2, AGS accelerator facility is explained. Section 3.3 is on the global detectors, and section 3.4 is on the Forward Spectrometer, which is used for the analysis. In section 3.5, only the features of the Henry Higgins spectrometer (HH) are concisely described. Finally, in section 3.6, the data acquisition system are mentioned.

3.2 AGS Accelerator Facility

Alternating Gradient Synchrotron (AGS) at Brookhaven National Laboratory is one of the accelerator to be able to accelerate heavy ions like Au up to 10 $\sim$ 15 A GeV

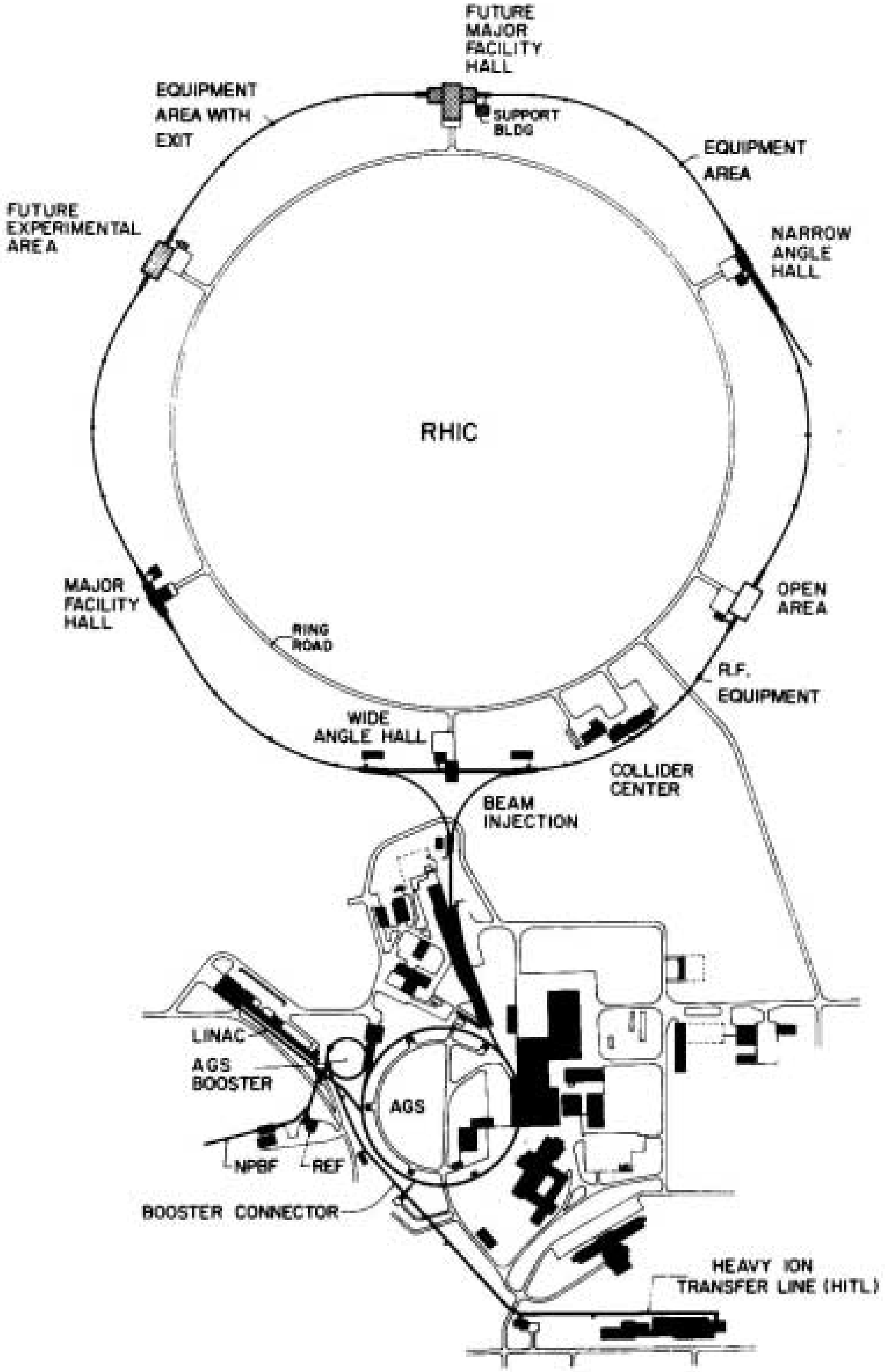

Figure 3.2: A schematic diagram of the AGS accelerator facility. The future collider ring, RHIC, is also shown in the upper part of the figure.

beam energy. The schematic diagram of the AGS accelerator facility is shown in Fig. 3.2. The AGS complex consists of Tandem Van de Graaff, the AGS Booster and the AGS main ring.

In order to extract Au beams at 11 A GeV/c, the Au ions are accelerated up to 1 A MeV at the Tandem Van de Graaff with a charge state of 13+, first. Then the Au beams are transfered to the Booster and accelerated to 192 A MeV with a charge state 33+. Before the injection to the AGS main ring, Au^{+33} ions are stripped their electrons up to Au^{+77}, then are transported to the AGS main ring and accelerated up to the final momentum, i.e., 11 A GeV/c [45]. At the experimental area, Au beams are transported with a charge 79 with $3{\sim}7 \times 10^4$ per spill at the target position. The repetition cycle is ~4 sec, and flat top is 1 sec/spill. In 1995/1996 run, in addition to 11 A GeV/c beam energy, two different lower energy of Au beams are available for the first time. The exact numbers of these energy in the 1995/1996 run are 2.003 and 4.04 GeV per nucleon in terms of a kinematic energy and 11.69 GeV/c per nucleon in terms of a momentum [46].

3.3 Global Detectors

In this section, the beam counter system (BTOT and HOLE), Bull's Eye counter (BE), the zero-degree calorimeter (ZCAL) and the New multiplicity array (NMA) are described. BTOT and HOLE are used to define the $BEAM$ trigger (see Section 4.3). BE is set to determine the interaction trigger (INT) by means of a measurement of the total number of projectile spectator's charges. ZCAL is placed to measure the total kinetic energy of the charged and neutral particles and give an information for a event characterization. NMA is placed around the target to measure the multiplicity of pions and it also give a measure of the centrality event by event.

3.3.1 Beam counter system (BTOT and HOLE)

The beam counter system consists of BTOT and HOLE counters. BTOT is a $\check{C}$erenkov counter with a quartz radiator to detect the incoming Au beam signals. The quartz has 51 mm height, 76 mm width and 200 μm thickness and positioned at 171 cm upstream of the target. Two 2-inch photo-multiplier tubes, Hamamatsu R2083, are equipped on its both sides for readout the signals. The resolution (σ_q/q) is estimated to be $\sim$ 1.9 %. BTOT provides a time-zero signal for the time-of-flight

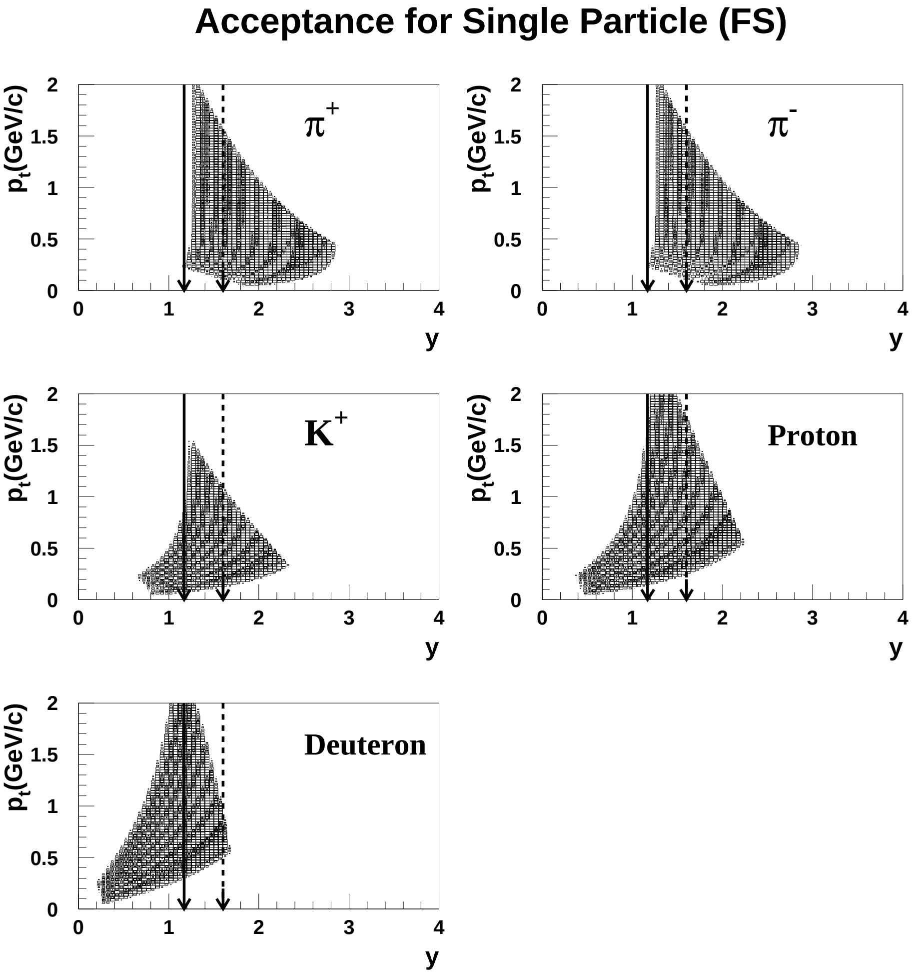

Figure 3.3: The coverage in the rapidity y and transverse-momentum p_t space of the Forward Spectrometer; for π^+ (top left), π^- (top right), K^+ (middle left), protons (middle right) and deuterons (bottom left). In each panel, mid-rapidity of 4 A GeV (solid arrow) and 11 A GeV (broken arrow) are also shown.

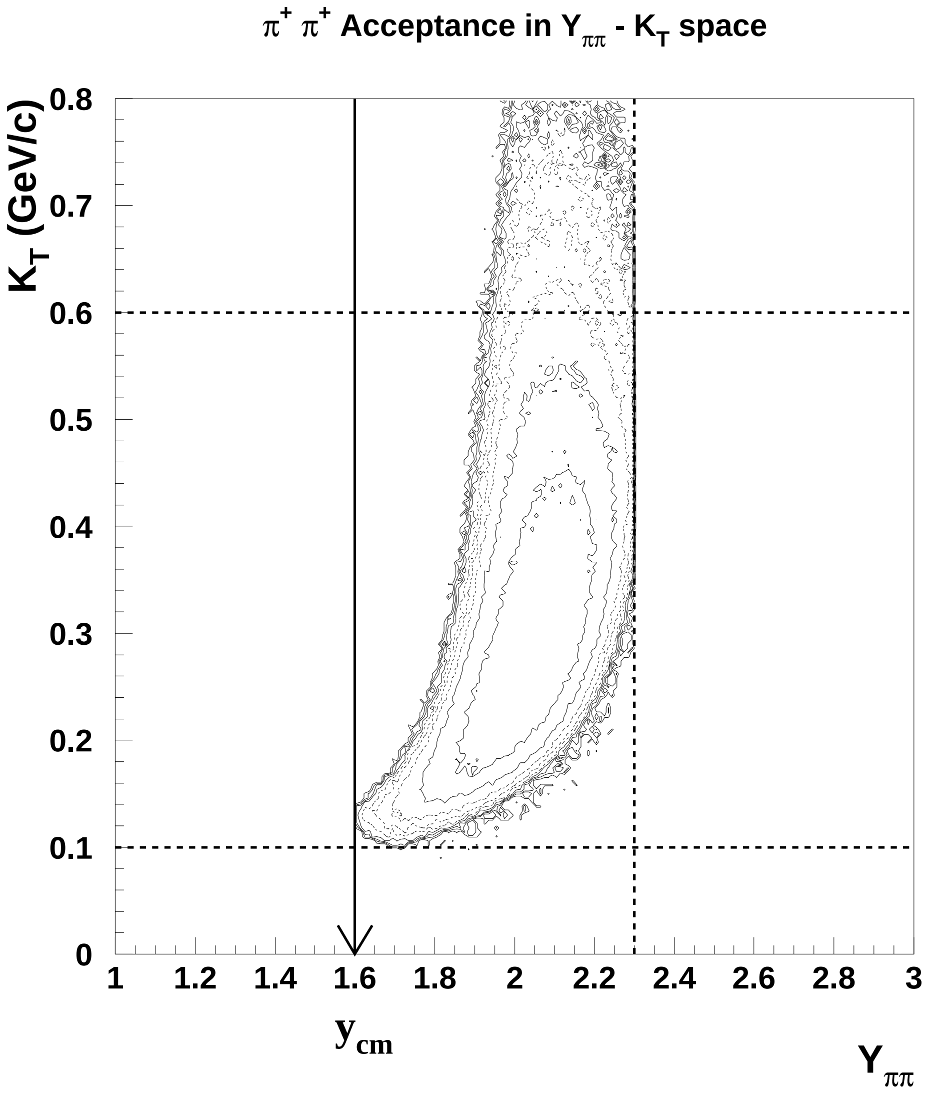

Figure 3.4: The acceptance of $\pi^+\pi^+$ pairs. The horizontal axis is the rapidity of pair, and the vertical axis is the average transverse momentum of pair. The arrow indicates the mid-rapidity $y_{\rm cm}$ at the energy of 11 A GeV.

counter. HOLE is a scintillation counter with a circular 10 mm diameter hole at the center, positioned at 145cm upstream from the target. To reject beam halo, only particles passing through its 10 mm hole are regarded as valid Au beams. Specifications of the beam counter system is listed in Table 3.1.

Counter	BTOT	HOLE	BE
Material	Quartz	Plastic Scintillator	Quartz
Thickness [mm]	0.2	3.2	0.3
Width [mm]	76.2	76.2	20 cm diameter
Height [mm]	50.8	50.8	–
Hole Diameter [mm]	–	10.	–
Distance from the Target [cm]	-171	-145	950

Table 3.1: Specifications of the beam counter system (BTOT and HOLE) and Bull's Eye counter (BE). A negative value in the row of "distance from the target" denotes upstream of the target.

3.3.2 Bull's eye counter (BE)

Bull's Eye counter, located at 9.5 m downstream from the target, is equipped to define an interaction trigger of beam particles with target nucleus by means of measurements of the total number of projectile spectator's charges. BE is a $\check{C}$erenkov counter, using a quartz (20 cm diameter and 300 μm thickness) as a radiator, with a light diffuser on the surface. As shown in Fig. 3.5, the $\check{C}$erenkov light is read out by eight 2-inch photo-multiplier tubes, Hamamatsu H1161, arranged radially around the radiator. The measured charge smaller than that of the beam particle provides the minimum bias interaction trigger. The resolution, σ_q/Z is $\sim$ 6.7 % [47]. Specifications of Bull's Eye counter is also listed in Table 3.1.

3.3.3 Zero-degree calorimeter (ZCAL)

To determine a geometry of a Au+Au collisions, Zero Degree Calorimeter (ZCAL) is placed at the zero degree in the laboratory frame, 11.7 m downstream from the target. ZCAL is the Fe-Scint. sandwiched-type hadronic calorimeter. ZCAL measured the energy of projectile fragments after collisions and it provides an estimation of the

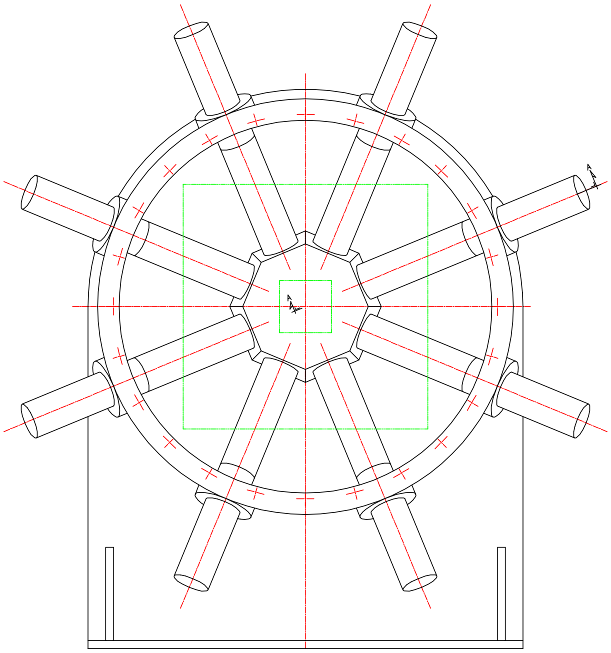

Figure 3.5: A beam view of Bull's Eye counter [47].

impact parameter of the interaction. ZCAL has 1.8 m length in the beam direction, which is divided into two components, called H1 and H2. The basic stacking unit is composed of a 10 mm iron plate followed by a 3 mm scintillator sheet, sandwiched between two TiO_2 coated Mylar sheets in order to diffuse the light and to protect the surfaces [48]. There are 32 stacking units in H1, 106 in H2. Eight light signals from each section are transmitted via wave length shifter plates to photo-multipliers at the rear of ZCAL. The sizes of the ZCAL have 60 cm height, 60 cm width and 193 cm length corresponding to 8.9 interaction lengths. The energy resolution of the ZCAL was $\sigma_E/\sqrt{E} = 2.88 \pm 0.02$ [GeV$^{1/2}$] in 1993 run [49].

3.3.4 New multiplicity array (NMA)

In addition to the Zero-degree colorimeter (ZCAL), an additional global detector, the New Multiplicity Array (NMA) has been built for E866 [50, 51, 52]. It is designed with the aim of providing a measure of the total number of particles and pseudo-rapidity distributions in a large solid angle. A second goal is to obtain a measure of the reaction plane for intermediate impact parameter reaction.

The NMA is an array of 346 $\check{C}$erenkov light detecting modules. A typical module

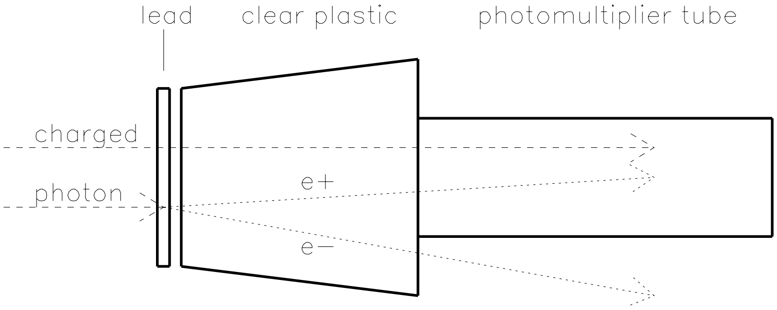

Figure 3.6: New Multiplicity Array (NMA) module [51].

shown in Fig. 3.6. Each module is composed of a clear plastic mated directly to a photo-multiplier tube. Since the index of refraction of the plastic is about 1.5, the $\check{C}$erenkov light begins to turn on at $\beta = v/c = 0.67$. This feature allows the detector to be sensitive mostly to fast charged particles, bulk of which are the produced charged pions. Furthermore, we need the detector to be sensitive to the produced neutral pions as well. We achieved this by placing a sheet of lead in front of the clear plastic. The photons from the decayed π^0s would then convert to e^+e^- pairs in the lead. The thickness of lead is chosen so that the conversion probability is 25 %. This yields, on the average, one particle response for each π^0, thus putting π^0 roughly on equal footing with the charged pion. The lead sheet does not affect the charged hadrons much, since the nuclear interaction length in lead is much longer. The added benefit of having a lead sheet in front of the module is that essentially all of the low-energy $\delta-$electrons from the target are blocked out.

The modules are arranged in close-packed fashion to cover the polar angle θ from 7^o to 112.3^o. Instead of using the variable θ, we usually use the variable pseudo-rapidity $\eta = -\ln(\tan(\theta/2))$. For relativistic particles, ($\beta \approx 1$), $\eta \approx y$, the rapidity variable. In our case, particle identification is not possible, we resort to using η. The array is segmented in such a way that the $\eta-$bite $\Delta\eta$ is some convenient number, most of them begin 0.20. The array covers the azimuth angle ϕ, with gaps left open for free passage of particles from the target to the spectrometers. The array is also segmented in ϕ, with most of the modules having a ϕ-bite $\Delta\phi$ of 10^o. Fig. 3.7 shows a schematic view of New Multiplicity Array (NMA). The response of each module is such that it can distinguish a single hit, double hits, etc. One then adds up hits from all the modules to yield a raw multiplicity. The segmentations in η and ϕ allow us to obtain the $dN/d\eta$ and $dN/d\phi$ (reaction plane) on an event-by-event basis.

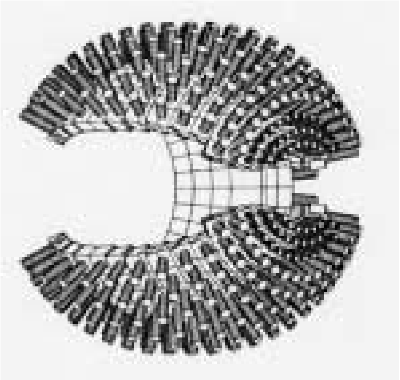

Figure 3.7: A schematic view of New Multiplicity Array (NMA) [50].

3.4 Forward Spectrometer (FS)

To cover the mid-rapidity region in Au+Au collisions at 11 A GeV/c, the Forward Spectrometer (FS) is newly equipped in 1993. FS is the rotatable spectrometer from 6 degrees to 27 degrees. In order to handle high multiplicity events and to achieve a reasonable tracking and particle identification, the Forward Spectrometer has been designed by considering the following points.

- Small solid angle (5 msr).
- Sweeping magnet (FM1) and heavy metal shields.
- Combination of time projection chambers and drift chambers.
- Finely segmented Time-of-flight wall detector.

The small solid angle reduces the number of tracks per event in the tracking chambers. The sweeping magnet and heavy metal shields reject background particles. Time projection chambers reconstruct tracks efficiently under high multiple tracks. The finely segmented Time-of-flight wall reduces inefficiencies caused by pile-up events. The performance of the spectrometer is summarized in Table 3.2 [44].

The Forward Spectrometer consists of heavy metal shields, dipole magnets, two tracking stations and finely segmented high resolution Time-of-flight wall. Each tracking station has a TPC with two drift chambers on both sides. In the following sections, each detector of FS is described.

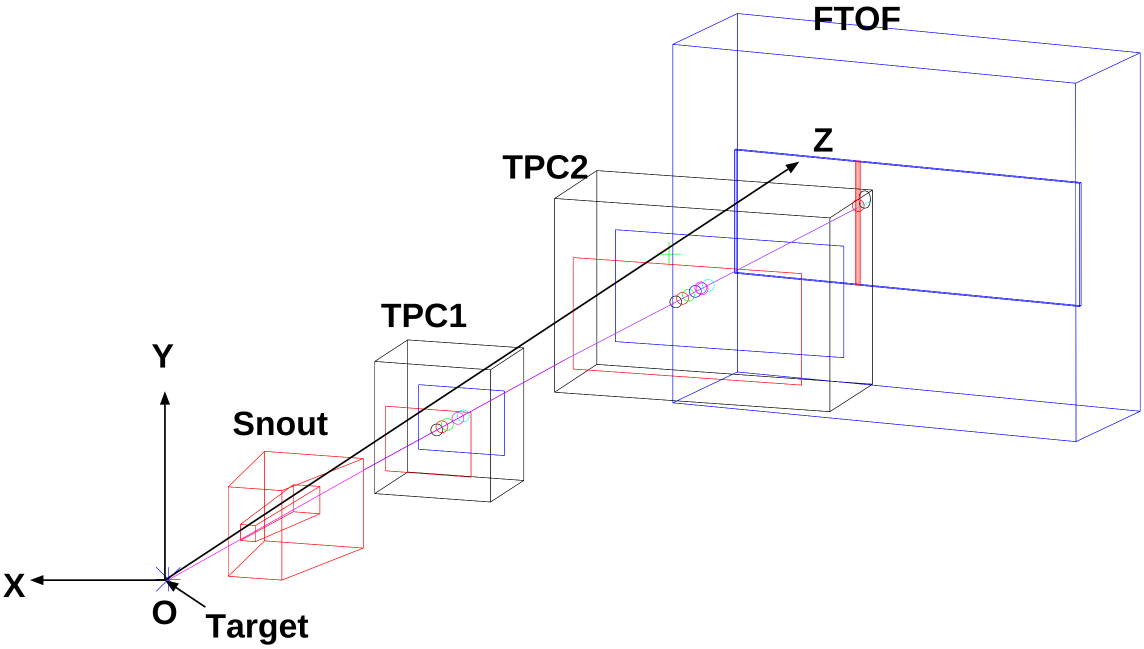

Figure 3.8: The Forward spectrometer coordinate.

3.4.1 Forward spectrometer coordinate

A Forward Spectrometer (FS) coordinate is defined as follows: The origin is at the target position; the z-axis called the 6-degree line is a line perpendicular to the surfaces of the magnets and the tracking chambers, the y-axis is upward direction; the x-axis is taken so that the coordinate system to be the right handed system. The spectrometer angle is defined as the angle between the incident beam line and the z-axis of the FS coordinates.

3.4.2 Dipole magnets (FM1 and FM2)

The Forward Spectrometer has two dipole magnets, named FM1 and FM2, respectively. FM1 is placed in front of the first tracking chamber station to remove background particles with low momentum. FM2 is placed between the tracking chamber stations as an analyzing magnet. FM2 has an 94 cm effective length and about 0.9 T·m bending power at its full strength. Field maps of FM1 and FM2 are measured with Hall probes. The specifications are summarized in Table 3.3.

	Performance
Solid angle	5 [msr]
Setting angle	6 – 27 [degree]
Momentum resolution (σ_p/p) (proton, $0 < p \leq 5$[GeV/c])	1.5 – 5 [%]
Time of flight resolution, $\sigma_{TOF}(\pi)$	~76 [psec]
$\pi - K$ PID separation (2.5σ)	$0 < p \leq 2.5$ [GeV/c]
$K - p$ PID separation (2.5σ)	$0 < p \leq 3.5$ [GeV/c]

Table 3.2: Performance of the Forward Spectrometer [44].

Magnet	FM1	FM2
Distance from the target [mm]	1754.	3505.
Field Gap Size ($x \times y \times z$) [mm^3]	229. × 159. × 508.	597. × 283. × 762.
Yoke Size ($x \times y \times z$) [mm^3]	546. × 616. × 800.	1346. × 1442. × 1156.
Effective Field Length [cm]	623.2	943.4
Maximum $B \cdot \mathrm{d}L$ [T·m]	0.249 (at 4 kG setting)	0.572 (at 6 kG setting)

Table 3.3: Specifications of the dipole magnets.

3.4.3 Tracking detectors (FT and TPC)

The spectrometer has two tracking chamber stations, named FTR1 and FTR2 in front and behind the analyzing magnet, FM2. Each tracking station has one TPC with two drift chambers on both sides of a TPC. The time projection chambers are used as the primary track-finding devices, using three-dimensional track information. Drift chambers improve spatial resolution of the tracks.

Time projection chamber (TPC)

A time projection chamber (TPC) is able to get three-dimensional hit positions of a charged particle's trajectory by simultaneous measurements a drift time and a hit position on an end cap Multi Wire Proportional Chambers (MWPC). TPC has an excellent pattern recognition capability even under the multi-track events, compared with a two dimensional chamber, *e.g.* a drift chamber.

TPC consists of a field cage, an end-cap wire chamber, a gating grid plane and a gas cage, as shown in Fig. 3.9 [53] with the coordinate system. There are two TPCs

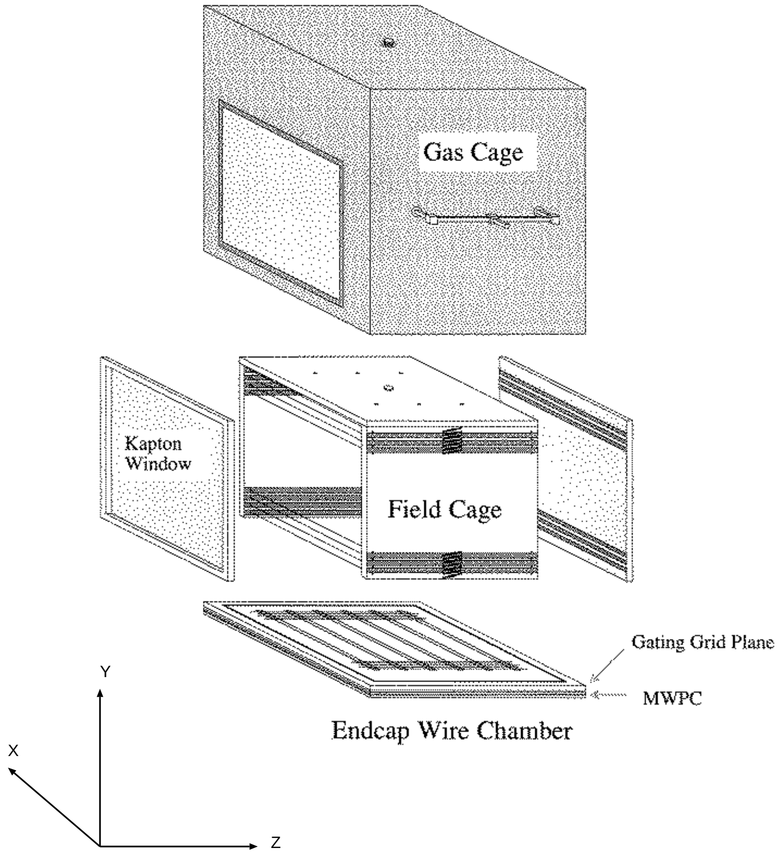

Figure 3.9: A schematic structure of the time projection chamber [54].

at each tracking station, called TPC1 and TPC2, placed upstream and downstream of FM2, respectively. We use Ar-isobutane (75:25) gas mixture for TPC1 and P-20 for TPC2 [54].

After the passage of charged particles in a TPC cage, electron-positive ion pairs are created along the path, and electrons drift in the field cage along the drift field to the gating grid plane. When the gating grid is opened by a trigger signal, the electrons pass through to the Multi Wire Proportional Chamber (MWPC). Strong field around the anode wires multiplies electrons and form an avalanche of secondary electrons. These electrons are observed as the anode current output. A field distortion due to the positive ions from the anode wires are suppressed by the gating grid systems. The performance of TPC1 and TPC2 is summarized in Table 3.4.

Chamber	TPC1	TPC2
Frame Size ($x \times y \times z$) [mm^3]	406. × 450. × 352.	965. × 660. × 450.
Field Cage Size ($x \times y \times z$) [mm^3]	300. × 248. × 280.	800. × 409. × 330.
Window Size ($x \times y$) [mm^2]	300. × 220. × 280.	800. × 380.
Effective Field Length [cm]	623.2	943.4
Effective Volume ($x \times y \times z$) [mm^3]	290 × 200 × 280	770 × 350 × 330
Number of Rows	6	6
Row-to-Row Pitch [mm]	46.	54.
Drift Field [V/cm]	800.	640.
Maximum Drift Length [cm]	26.	42.
Anode-to-Anode Pitch [mm]	3.	4.
Anode-to-Cathode Gap [mm]	3.	4.
Effective Anode Wire Length [mm]	7.	7.
Anode Wire Diameter [μm]	15.	15.
Operation Voltage [-kV]	1.90	2.15 − 2.20
Number of Anode Wires [/row]	96	192
Total Number of Readout	576	1152
Gating Grid Wire Pitch [mm]	1.	1.
Grid-to-Cathode Distance [mm]	8.	8.
Gating Grid Operation Voltage [V]	±50.	±80.

Table 3.4: Specifications of the time projection chambers.

Drift chambers (FT)

Four drift chambers, FT1, FT2, FT3 and FT4, are equipped for determination of precise hit positions of tracks using its good spatial track defining capability. The typical resolution is 250 μm $\sim$ 370μm. The specifications of drift chambers are listed in Table 3.5 and the plane configuration of the drift chambers are summarized in Table 3.6. FT1 and FT2 have 10 planes with the wire configuration of ($xx'uu'yy'vv'xx'$), and FT3 and FT4 have 8 planes with ($xx'uu'vv'xx'$). Each pair planes are staggered by a half cell to cover inefficient region near wires and to solve the left-right ambiguity. The gas mixture are Ar-isobutane (50:50) for each FT. FT2 and FT3 are also used to define the Forward Spectrometer trigger ($FSPEC$) (see Section 4.3).

Chamber		FT1	FT2	FT3	FT4
Frame Size	x [mm]	338.	503.	844.	1003.
	y [mm]	394.	394.	520.	520.
	z [mm]	60.	60.	81.	81.
Window Size	x [mm]	238.	353.	644.	803.
	y [mm]	174.	233.	320.	360.
Number of Planes		10	10	8	8
Anode Plane Pitch [mm]		3.2	3.2	4.8	4.8

Table 3.5: Specifications of the drift chambers.

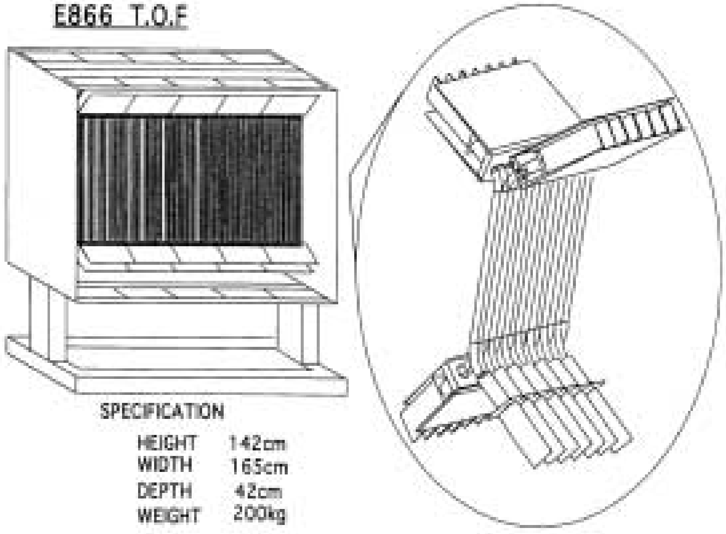

Figure 3.10: The schematic view of the Time-of-flight wall, FTOF.

3.4.4 Time-of-flight wall (FTOF)

The Time-of-flight wall, FTOF, is used to measure the time-of-flight of particles from the target to the FTOF wall. By combining the time-of-flight with the momentum and the path length of the particles, the particle identification is carried out. Fig. 3.10 shows the schematic view of FTOF. FTOF is positioned at 6 m from the target, most downstream of the Forward Spectrometer. FTOF consists of 100 slats of plastic scintillator, BC404 of Bicron. The dimensions of the slat is 1.24 cm × 42 cm × 1.25 cm (width × hight × depth). The specifications of FTOF are summarized in Table 3.7.

Each slat is read out with two 3/4 inch photo-multiplier tubes (PMT), Hamamatsu-

Chamber	Plane Order	Wire	Orientation	# Wires	Drift Length
FT1	$xx'uu'yy'vv'xx'$	x	0. deg.	56	2.0 mm
		y	90. deg.	40	2.0 mm
		u	$-30.$ deg.	64	2.0 mm
		v	30. deg.	64	2.0 mm
FT2	$xx'uu'yy'vv'xx'$	x	0. deg.	56	3.0 mm
		y	90. deg.	36	3.0 mm
		u	$-30.$ deg.	64	3.0 mm
		v	30. deg.	64	3.0 mm
FT3	$xx'uu'vv'xx'$	x	0. deg.	78	4.0 mm
		u	$-30.$ deg.	80	4.0 mm
		v	30. deg.	80	4.0 mm
FT4	$xx'uu'vv'xx'$	x	0. deg.	78	5.0 mm
		u	$-30.$ deg.	80	5.0 mm
		v	30. deg.	80	5.0 mm

Table 3.6: Plane configuration of the drift chambers.

R3478S, through light guides on its both ends. Each PMT is mounted on a board which have a bleeder circuit for PMT and a discriminator, called on-tube discriminator [55]. The on-tube discriminator have two outputs: passively internally split analog signal and discriminated output. The discriminated signals are re-discriminated in the counting house to reshape the signals before sending them to TDC, and then are recorded with Phillips CAMAC TDC model 7186 with 25 psec/bin. The analog signals are transfered to LeCroy FASTBUS ADC 1882N in the counting house. ADC values are used in off-line analysis for a slewing correction as well as for a charge cut.

Distance from the target [m]	6.0
Effective Area ($x \times y$) [mm^2]	1260×420
Number of Slats	100
Slat Size ($x \times y \times z$) [mm^3]	$12.4 \times 419. \times 12.5$

Table 3.7: Specifications of FTOF.

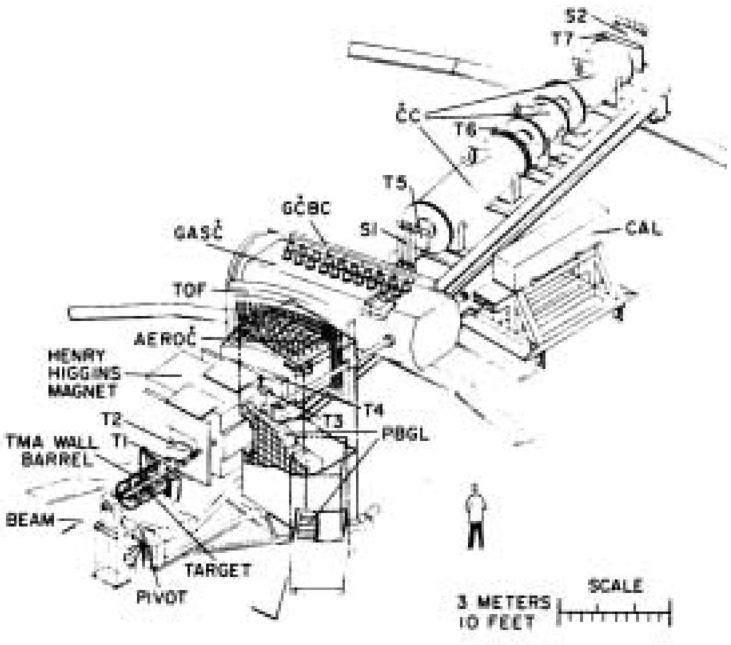

Figure 3.11: A schematic view the Henry Higgins spectrometer system [56].

3.4.5 Heavy metal shields

To shield particles from chamber frames of the first tracking station (FTR1) and the return yoke of FM1 magnet, the collimator made of Tungsten is put between the target and FM1. The heavy metal shield is also equipped on the beam side wall of FM1 to reject the particles from the beam pipes to the first tracking station.

3.5 Henry Higgins Spectrometer (HH)

The Henry Higgins Spectrometer is placed on the opposite side of the Forward Spectrometer with respect to the beam line. It has been used for the E802/E859 experiments as an main spectrometer, and for the E866 experiment, and it is used to cover the backward region from $\sim$ 20 degrees with respect to the beam line. By combining these two spectrometers, it is possible to cover a wide $y - p_t$ acceptance. The aperture is 25 msr. In the analysis, the data taken by HH is not used. Details of the Henry Higgins Spectrometer are described in [56].

3.6 Data Acquisition System

The data acquisition system consists of 11 CPU's in a single VME create, and gathered data from 8 CAMAC crates and 6 FASTBUS crates [57]. The DAQ system is managed by two Tadpole TP40V 68040-based CPU's which function together as event builder, data reformatter, network interface, and tape logger. Data from CAMAC modules are read by crate controllers based on SBE VPU25 modules with 68020 CPU's. FASTBUS data are collected by a LeCroy 1821 Segment Manager in each FASTBUS crate, and transferred via fiber-optic link to a custom-built interface to the VME bus. Data transferred from CAMAC and FASTBUS crates are assembled and finally recorded on 8 mm tape using an Exabyte Model 8510 drive with write speed up to 500 kByte/sec.

Chapter 4

Run Conditions

In this chapter, run conditions used for 4 and 11 A GeV data analysis are summarized. The beam energy, targets, trigger definition, the spectrometer setting and data statistics are described in the following sections.

4.1 Beam Energy

In 1995/1996 run, two different lower energy of Au beams have been available for the first time in addition to 11 A GeV/c beam energy. The exact beam energy is 2.003 and 4.04 GeV per nucleon in terms of a kinematic energy and 11.69 GeV/c per nucleon in terms of a momentum [46]. In the analysis, the data taken from 4 and 11 A GeV beam energy run are used.

4.2 Targets

For 4 A GeV run, ^{197}Au target, 1.961 g/cm^2 thickness, corresponding to the 3.0% interaction rate is used. For 11 A GeV run, targets of 1.5%, 3.0%, 4.0% and 5.0% interaction rate are used. Data without a target, called empty target is also taken for the background subtraction.

4.3 Trigger Conditions

We have collected data with four different triggers defined as follows.

1. $BEAM$ trigger

The first one is the $BEAM$ trigger for a good beam particle. It is defined with the beam counters as;

$$BEAM \equiv \overline{PRE} \cap BTOT \cap \overline{HOLE}, \tag{4.1}$$

where $\overline{PRE}$ shows that there is no other particle arrived within 500 nsec [46] (pile-up rejection).

2. INT trigger

The second is the interaction trigger, INT, defined with Bull's Eye counter for an event in which a beam particle interact with a target particle. The definition is as follows;

$$INT \equiv BEAM \cap \overline{BE}, \tag{4.2}$$

where $\overline{BE}$ indicates that the measured charge of particle with Bull's Eye counter is lower than a threshold.

3. $FSPEC$ trigger

The third is $FSPEC$ for an event in which at least one particle enter the Forward Spectrometer. The definition is as follows;

$$FSPEC \equiv INT \cap FT2 \cap FT3, \tag{4.3}$$

where $FT2$ ($FT3$) is required to have at least one of all wires on the first and second planes of the FT2 (FT3).

4. $\overline{ZCAL}$ trigger

This defines central events, which means a beam particle and target particle collide with a small impact parameter.

$$\overline{ZCAL} \equiv INT \cap \overline{HZCAL}, \tag{4.4}$$

where $\overline{HZCAL}$ means an event with the hardware sum of ZCAL signals below the threshold, which is set that the ratio of trigger counts, $\overline{ZCAL}/INT$ is $8 \sim 11\%$.

Angle	Polarity	No. of $FSPEC$ triggers
6	2A/4A	0.2 M
	2B/4B	3.2 M
9	2A/4A	0.2 M
	2B/4B	3.5 M
12	2A/4B	2.6 M
15	2A/4B	2.6 M
18	2A/4B	1.5 M
21	2A/4B	1.5 M
24	2A/4B	1.5 M
27	2A/4B	1.5 M
Total	–	18.3 M

Table 4.1: The statistics of $FSPEC$ trigger at 4 A GeV beam energy. These data set are used for the single particle spectra analysis.

4.4 Analyzed Data Set

We have taken data of $FSPEC$ trigger with 8 spectrometer angle settings from 6 to 27 degrees in 3 degrees step for 4 A GeV run, 10 angle setting from 6 to 24 degrees in 2 degrees step for 11 A GeV run. For $\overline{ZCAL}$ trigger, we have taken data only 10 degrees angle setting at the energy of 11 A GeV. We have also taken data with 0k G/0 kG, called zero-field run, for geometry calibration of tracking chambers and for background subtraction. Table 4.1 and 4.2 summarize the data statistics of $FSPEC$ trigger at 4 and 11 A GeV beam energy. In Table 4.3, statistics of $\overline{ZCAL}$ trigger at 11 A GeV beam energy are summarized. In this thesis, the data with $FSPEC$ trigger are used for single particle analysis in order to evaluate in various centrality, and the high statistic data with $\overline{ZCAL}$ are used for HBT analysis.

The polarity which bent positive particles toward the beam is called as A polarity, which is the negative-favor setting for the Forward Spectrometer; the other polarity is called as B polarity. The magnetic field of FM1 is set at 0.2 [T] except for zero-field runs, and that of FM2 is at 0.4 [T] (0.249 [T·m]) and 0.6 [T] (0.572 [T·m]).

Angle	No. of $FSPEC$ triggers			
	A-polarity			B-polarity
	2A/4A	2A/6A	A Total	2B/4B
6	3.2M	0.8M	4.0M	2.7M
8	3.4M	1.1M	4.5M	2.6M
10	3.3M	0.9M	4.2M	3.2M
12	2.7M	0.7M	3.4M	2.4M
14	4.3M	0.5M	4.8M	2.4M
16	4.4M		4.4M	2.7M
18	4.6M		4.6M	1.6M
20	4.3M		4.3M	0.1M
22	1.3M		1.3M	0.3M
24	1.7M		1.7M	0.2M
Total	33.2M	4.0M	37.2M	18.2M

Table 4.2: The statistics of $FSPEC$ trigger at 11 A GeV beam energy. These data set are used for the single particle spectra analysis.

Angle	Polarity	No. of $\overline{ZCAL}$ triggers
10	2A/4B	23.6 M
Total	–	23.6 M

Table 4.3: The statistics of $\overline{ZCAL}$ trigger at 11 A GeV beam energy. These data are used for the two-particle correlation analysis.

Chapter 5

Data Reductions

The outline of this chapter is as follows. In section 5.1, the geometry calibration and chambers and the time-of-flight counter calibrations are explained. In section 5.2 to 5.4, the methods of track reconstruction, momentum determination and particle identification are described. In section 5.5, Tracking efficiency correction, in section 5.6, the time-of-flight counter detection efficiency, in section 5.7 decay corrections are described.

5.1 Calibration

A position alignment, called geometry calibration, is carried out at the first stage of the data reduction in order to reconstruct tracks and momenta. After the geometry calibration, drift chambers (FT), time projection chambers (TPC) and time-of-flight counter (FTOF) are calibrated.

5.1.1 Geometry calibration

Before the run started, the positions of each detector have been surveyed in x-, y- and z- directions and placed at the designed positions. We assume that the z- positions of each detector is correct, since there is no way to calibrate in this direction. In x- and y- directions, the geometry of FT and TPC are calibrated so as to reconstruct the straight tracks using the data of zero-field run for each angle setting. The calibration procedure is as follows. First, hit positions on four drift chambers are fitted to a straight line, and adjust its x and y position so as to have minimum χ^2 values for reconstructed tracks. At this stage, TPC information is not used in order to avoid affection by non-calibrated TPC tracks to FT's geometry calibration. Next, TPC's geometry in x direction is calibrated by using the calibrated geometry parameters of FT. All six rows at each TPC are aligned so as to reconstruct straight line. This calibration is carried out at each row and at each TPC for all zero-field run, independently.

5.1.2 FT calibration

A drift time t, a drift velocity v and a distance from an anode wire l are calibrated for each drift chamber, and v and l are parameterized as following;

$$\begin{aligned} t &= TDC - t_0, & (5.1)\\ v(t) &= \frac{a_0}{2\sqrt{t}} + a_1 + 2a_2 t, & (5.2)\\ l(t) &= a_0\sqrt{t} + a_1 t + a_2 t^2, & (5.3) \end{aligned}$$

where TDC is the TDC value, t_0 is the time-offset, and a_i are fitting parameters. The calibration constants and t_0 are calibrated on plane-by-plane every angle setting by using straight tracks of zero-field run.

5.1.3 TPC calibration

After the FT's geometry calibrations, each TPC's geometry is calibrated at every angle setting using zero-field run. At this stage, every rows on each TPC are aligned so as to be consistent with FT. For calibration of y-position of a track in TPCs, time-zero t_0 and drift velocity of electrons v are adjusted at each row. y-position of a track in TPC is given as

$$y(t) = v(t - t_0), \tag{5.4}$$

as a function of drift time t. In addition to these calibration, TPC2 needed more calibration parameters, because of shift of a hit position due to the drift field distortion and the magnet fringing field. Here, we summarize the TPC calibration procedure. The procedure can be divided into four categories as follows.

1. X-offset, x_0, calibration at each raw for the geometry calibration.
2. Time-zero, t_0, and drift velocity, v_0 calibration at each row.
3. Field distortion correction in x- direction, $X_{cor}(x, y)$, as a function of the x- and y-coordinates depending on the FM2 field at each row of TPC2.

4. Field distortion correction in y- direction, $Y_{cor}(y)$, as a function of the y-coordinate at each row of TPC2.

The dependence of these calibration parameters are summarized in Table 5.1. In the analysis, TPC is calibrated as the same way that was carried out in '94 run data analysis. See [58] for detail description.

parameter	applied TPC name	dependence
x_0	TPC1, TPC2	angle
t_0	TPC1, TPC2	angle, time
v	TPC1, TPC2	time
X_{cor}	TPC2	FM2 field
Y_{cor}	TPC2	–

Table 5.1: The calibration parameters of TPC and its dependence on angle setting, time and magnetic field setting of FM2.

5.1.4 FTOF calibration

FTOF calibration is performed after the track reconstruction and the momentum determination (see Section 5.2 and 5.3). Time of flight, TOF, and y position of a charged particle, y_{TOF}, are calculated as follows,

$$TOF = \frac{t_{S_{\mathrm{top}}} + t_{S_{\mathrm{bot}}}}{2} - BTOT - t_0, \tag{5.5}$$

$$y_{\mathrm{TOF}} = \frac{(TDC_{\mathrm{bot}} - TDC_{\mathrm{top}})}{2} \cdot v + y_0, \tag{5.6}$$

$$t_{S_i} = TDC_i \cdot C_i - \frac{S_i}{\sqrt{ADC_i - PED_i}}, \tag{5.7}$$

$$BTOT = \frac{TDC_{\mathrm{L}} \cdot C_{\mathrm{L}} + TDC_{\mathrm{R}} \cdot C_{\mathrm{R}}}{2}, \tag{5.8}$$

where

TDC_i : TDC value
ADC_i : ADC value
PED_i : ADC pedestal [ADC bin]
t_0 : time offset [nsec]
y_0 : y-position offset [mm]
C_i : TDC time conversion factor [nsec/TDC bin]
v : propagation velocity of light in plastic scintillator [mm/TDC bin]
S_i : slewing correction factor [nsec/(ADC bin)$^{1/2}$]

and suffices $i =$ “top” or “bot” denotes a PMT mounded on the top or bottom of the slat of FTOF wall, suffices ”L” or “R” denotes a PMT mounted on the left or right side of BTOT counter. The y_0 is calibrated with the FS tracks (see Section 5.2) for each slat. The slewing correction factors are calibrated with pions, roughly identified with squared mass of $-0.2 < m^2 < 0.15$, for each PMT. After the slewing correction, the t_0 are re-calibrated with $\pi^{\pm}$. The calibration of the t_0 or y_0 is performed every $10 \sim 15$ runs.

5.2 Track Reconstruction

A track reconstruction code for the Forward Spectrometer, called FAReAST [1] has been developed for the E866 collaboration. The basic algorithm of the track reconstruction code is follows. First, the tracks are formed independently in each TPC complex, called TPC tracks. Second, TPC tracks are extended to the both upstream and downstream drift chambers, and are associated with the hits of drift chambers and can be reconstructed tracks at each tracking stations, called FTR1 and FTR2 tracks, respectively. Third, if distances between a FTR1 and a FTR2 are close within 3σ of their distributions, FTR1 and FTR2 tracks are connected at the mid-plane of FM2 and formed FS tracks. Then their momenta are calculated using a transfer matrix. Finally, the track is traced back to the target z position through FM1 magnet using the calculated momentum. And they are also associated to the FTOF position. FAReAST searches for FTOF hits which have within a 3σ of the track positions.

---

[1] Forward Arm Reconstruction Algorithm Starting from the TPC’s.

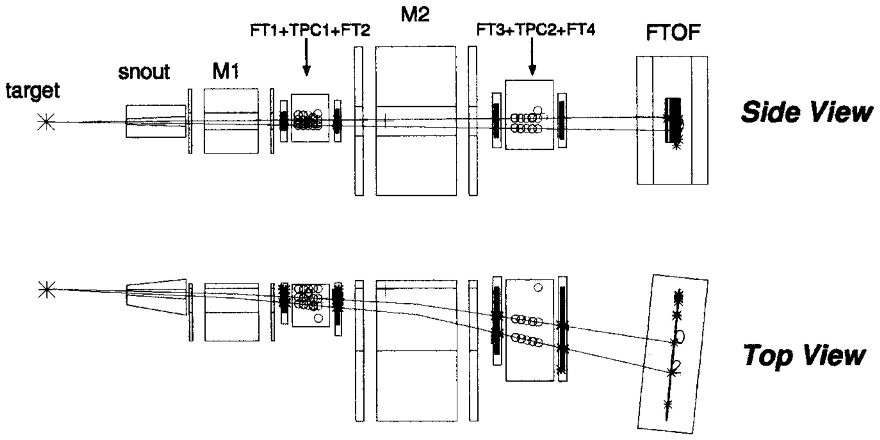

Figure 5.1: A typical event at the 14 degree, 2A/4A magnetic setting with two reconstructed tracks. A side view and a top view of the Forward Spectrometer are shown.

5.2.1 Track finding by TPC

TPC is used as an initial track finder, taking advantage of its high three dimensional pattern recognition performance. As the drift electrons diffuse in both x- and y-directions while drifting in the chambers, a few wires on a row could be fired due to their finite cluster size in x-direction. And because of the feature of the amplifiers, a few pulses could be made in the y-direction. We perform a clustering from several close hits and calculate the incident particle position as the center of the clusters. After the clustering, TPC track is formed by searching hit rows which have aligned clusters and combining them. These series of clusters are fitted by a straight line to calculate a track position and a track vector. For the reconstruction of TPC tracks, at least 3 rows hits are required.

5.2.2 Track confirmation by FT

TPC tracks are extrapolated onto FTs on both sides of accompanying TPC in order to get more precise position information of tracks. If the number of planes without close FT hits (missing planes) is ≤ 4, the track is combined with the closest FT hits, and regarded as FTR tracks at each tracking station. Each FTR track is re-fitted with a straight line using the position information of both TPC and FT. The left/right ambiguity on each plane of FTs is solved at the same time, in an iterative way to

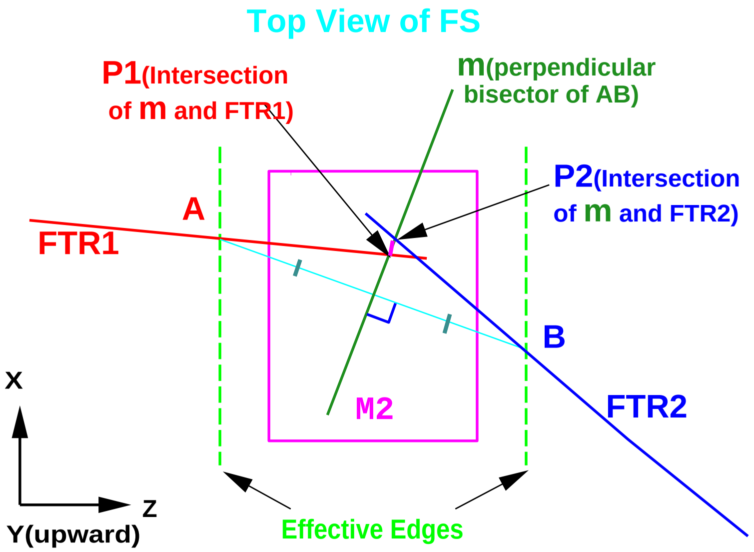

Figure 5.2: A illustration of the definition of track matching at FM2. Points A and B are intersections of FTR1 and FTR2 with entrance and exit edges of FM2, respectively. Plane "m" is the perpendicular bisector of $\overline{AB}$. P1 and P2 are intersections of FTR1 and FTR2 with m. Coordinates of P1 and P2 are P1(x_1, y_1), P2(x_2, y_2), where x_i and y_i are defined in Eq. 5.9 and 5.10, respectively.

minimize the χ^2 of the fitting.

5.2.3 Track matching at analyzing magnet

After reconstruction of FTR tracks, FTR1 and FTR2 are extended to FM2 magnet and connected on the plane m in the FM2. Fig. 5.2 shows the definition of the plane m. The track position matchings in the x- and y-directions (Δx and Δy) and the vector matching in y-direction ($\Delta\theta_y$) are defined as follows.

$$\Delta x \equiv x_2 - x_1, \tag{5.9}$$

$$\Delta y \equiv y_2 - y_1, \tag{5.10}$$

$$\Delta\theta_y \equiv \frac{dy_2}{dz_2} - \frac{dy_1}{dz_1}, \tag{5.11}$$

where x_i and y_i are the x- and y-position of FTRi track projected onto the plane m, and dy_i/dx_i is the slope of the track in the y-z plane. The cut criteria of distance between FTR1 and FTR2 track at the matching plane should depend on momentum due to multiple Coulomb scattering. Since the momenta of the tracks are not determined yet at this stage, the cut are set loose as,

$$\begin{aligned} \Delta x &< 5\sigma_{\Delta x}, && (5.12) \\ \Delta y &< 5\sigma_{\Delta y}, && (5.13) \\ \Delta\theta_y &< 5\sigma_{\Delta\frac{dy}{dz}}, && (5.14) \end{aligned}$$

where σ is the width in r.m.s of their distributions. The pairs of FTR1 and FTR2 tracks which fulfilled the loose criteria, are regarded as FS tracks. The widths of their distributions are determined by their intrinsic detector resolutions and the multiple Coulomb scattering. The widths are fitted with a function as follows,

$$\sigma_i(\beta p) = \sqrt{a_0 + \frac{a_1}{(\beta p)^2}} \qquad (5.15)$$

where i is x or y or dy/dz, a_0 and a_1 are fitting parameters. After momentum determination and TOF association, Eq. 5.12- 5.14 are replaced to refined 3σ cuts.

5.2.4 Target cut

To reject the wrong combination between FTR1 and FTR2, the target cut is applied. After momentum determination, each FS track is traced back to the target position through FM1. The width of the target image in x- and y-directions also depended on momentum. The widths are also fitted with Eq. 5.15, and the target cut is applied using the widths as a function of βp. Target position residuals in x- and y-directions, Δx_t and Δy_t are defined as follows;

$$\begin{aligned} \Delta x_t &\equiv x_t - \overline{x_t}, && (5.16) \\ \Delta y_t &\equiv y_t - \overline{y_t}, && (5.17) \end{aligned}$$

where x_t (y_t) is the target position in x (y)-direction, and $\overline{x_t}$ ($\overline{y_t}$) represents their mean values. The target position is defined as the track position at $z = 0$, which calculated by tracing back the FTR1 track M1, using a ray-tracing method.

5.2.5 Fiducial cut

As the acceptance of the spectrometer is determined by the collimator, the emission angles of the accepted particles should have a clear cutoff both in the x- and y- directions. But in practice, the spectrometer has the finite angular resolution,

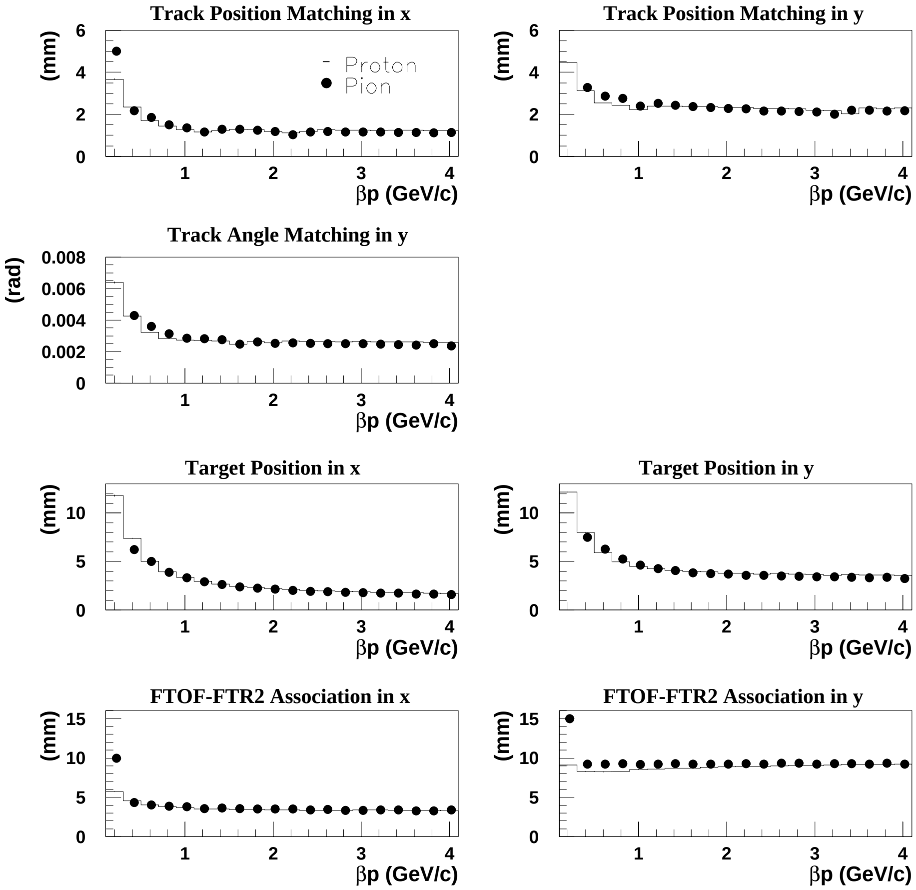

Figure 5.3: Widths of seven cut parameters in r.m.s as a function of βp [GeV/c] for protons (solid line), π^+ (filled circle). These plots show from the top left figure; widths of the track matching [mm] in the x-direction (the first row left), in the y-direction (the first row right), the track angle matching [rad] in the y-direction (the second row left), target positions [mm] in the x-direction (the third row left), in the y-direction (the third row right), and the FTOF hit residual [mm] with respect to the track position in the x-direction (bottom row left), and in the y-direction (bottom row right).

the measured distribution of emission angle has blunt edges. In order to avoid the distortion of the particle distribution near the edges of the geometrical acceptance, a fiducial cut is applied on the emission angle at the target.

5.2.6 Association with FTOF

Each FS track is extrapolated onto FTOF wall for association with FTOF hits. FTOF position residuals with respect to FTR2 track positions in the x- and y- directions, Δx_{TOF} and Δy_{TOF} are defined as;

$$\Delta x_{\mathrm{TOF}} \equiv x_{\mathrm{TOF}} - x_{\mathrm{FTR2}}, \tag{5.18}$$

$$\Delta y_{\mathrm{TOF}} \equiv y_{\mathrm{TOF}} - y_{\mathrm{FTR2}}. \tag{5.19}$$

The cut for the association between FTOF hit and FTR track is applied as the same way as the track matching cut at FM2 and the target cut using Eq. 5.18 and 5.19 in both x- and y- directions.

5.3 Momentum Determination

Using the field map of FM2 which is measured with the Hall probe, the momentum calculation of the FS tracks are performed.

In general, the relation between the momentum kick of a track passing through magnetic field is as follows,

$$\Delta \mathbf{p} = q \oint \mathbf{B} \times d\mathbf{s}, \tag{5.20}$$

where q is the charge of a particle, $\mathbf{B}$ the magnetic field, and $\mathbf{s}$ the path of the particle in the magnetic field. If we take units of them as $\mathbf{p}$[GeV/c], $\mathbf{B}$[T], $\mathbf{s}$[m], and $q[e]$, the above equation becomes as follows;

$$\Delta \mathbf{p} = 0.29979 \cdot q \oint \mathbf{B} \times d\mathbf{s} \ [\mathrm{GeV/c}], \tag{5.21}$$

where c is the velocity of light. For the x-component, the following equation is derived;

$$\begin{aligned} \Delta p_x &= 0.29979 \cdot q \oint (B_y dz - B_z dy) \\ &\simeq 0.29979 \cdot q \oint B_y dz \ [\mathrm{GeV/c}]. \end{aligned} \tag{5.22}$$

We ignore $\oint B_z dy$ for the following reasons. The main component of $\mathbf{B}$ both in M1 and M2 is B_y. Typically B_x and B_z are less than 100 G, which are only a few percent

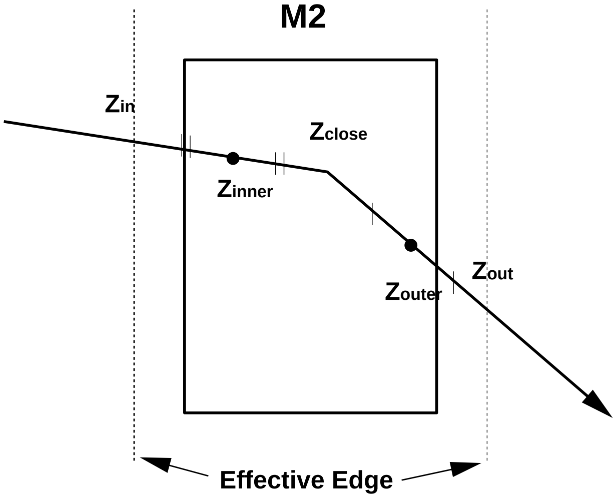

Figure 5.4: A demonstration of $\oint B_y dz$ sampling points for the momentum calculation.

of B_y (2 kG for M1, 4 or 6 kG for M2). Furthermore, the main component of $\mathbf{s}$ in the magnetic field is z. The path length $\oint dz$ is 508 mm for M1, and 762 mm for M2, while $\oint x$ and $\oint y$ are less than 100 mm. As a consequence, $\oint B_z dy$ is 3 order smaller than $\oint B_y dz$. We make the table of $\oint B_z dy$ for every (x_i, y_i) mesh point, along z-axis from entrance effective edge to exit effective edge. In order to calculate $\oint B_z dy$ with a reasonable accuracy, we take two points, $\mathrm{x}_{\mathrm{inner}}$ and $\mathrm{x}_{\mathrm{outer}}$ as shown in Fig. 5.4. The two points are defined as,

$$\mathbf{x}_{\mathrm{inner}} = \frac{\mathbf{x}_{\mathrm{in}} + \mathbf{x}_{\mathrm{close}}}{2}, \tag{5.23}$$

$$\mathbf{x}_{\mathrm{outer}} = \frac{\mathbf{x}_{\mathrm{close}} + \mathbf{x}_{\mathrm{out}}}{2}, \tag{5.24}$$

where $\mathbf{x}_{\mathrm{in}} = (x_{\mathrm{in}}, y_{\mathrm{in}}, z_{\mathrm{in}})$ is the FTR1 track position at z_{in} (entrance effective edge), $\mathbf{x}_{\mathrm{out}} = (x_{\mathrm{out}}, y_{\mathrm{out}}, z_{\mathrm{out}})$is the FTR2 track position at z_{out} (exit effective edge), and $\mathbf{x}_{\mathrm{close}}$ is the closest approach point between a pair of FTR1 and FTR2 tracks. The momentum kick in the x-direction is calculated with the average of the two field integration $\oint B_y dz$, as follows.

$$\Delta p_x = \frac{0.29979q(\oint By\mathrm{d}z_{(\mathrm{inner})} + \oint By\mathrm{d}z_{(\mathrm{outer})})}{2}, \tag{5.25}$$

where $\oint By\mathrm{d}z_{(\mathrm{inner})}$ is calculated along z-axis through the point ($\mathrm{x}_{\mathrm{inner}}$, $\mathrm{y}_{\mathrm{inner}}$), so as

$\oint By\mathrm{d}z_{(\mathrm{outer})}$. Finally, the momentum of the particle is calculated as

$$p = \frac{\Delta p_x}{u_x^2 - u_x^1} \tag{5.26}$$

where u_x^i denotes dx/dz of FTR$_i$ track (i=1,2).

As the check of the absolute value of calculated momentum, we examine a lambda mass peak formed from $p - \pi^-$ pairs. Fig. 5.5 shows the invariant mass distribution of $p - \pi^-$ pairs observed in 4 A GeV Au+Au collisions. The peak corresponds to Λ, and it is fitted by a Gaussian function. We obtained the mean (m_Λ) and the width (σ_{m_Λ}) as,

$$\begin{aligned} m_\Lambda &= 1116.0 \pm 0.1 \text{ [MeV}/c^2], && (5.27) \\ \sigma_{m_\Lambda} &= 3.25 \pm 0.19 \text{ [MeV}/c^2], && (5.28) \end{aligned}$$

The error of the peak position relative to the rest mass (1115.7 MeV/c^2) is 0.3 ± 0.1 MeV/c^2. By the kinematics of decay ($\Lambda \rightarrow p + \pi^-$), the momentum of decayed p and π^- in the rest frame of Λ, p_{cm} is expressed as,

$$p_{cm} = \frac{M_\Lambda \sqrt{1 - (\frac{m_p + m_\pi}{M_\Lambda})^2}}{2} = 0.106 \text{ [GeV}/c], \tag{5.29}$$

where M_Λ, m_p and m_π are mass of Λ, p and π^-, respectively. The relation between the error of momentum Δp_{cm} and the error of the Λ mass peak, ΔM_Λ, is derived by Eq. 5.29 with p_{cm} as,

$$\frac{\Delta p_{cm}}{p_{cm}} = \Big(\frac{M_\Lambda^2}{2p_{cm}^2} - 1\Big)\frac{\Delta M_\Lambda}{M_\Lambda}. \tag{5.30}$$

Using Eq. 5.30, the corresponding momentum error is estimated as 1.5 ± 0.5 %.

5.4 Particle Identification

The particle species are identified by its squared mass, m^2 and momentum. The squared mass is calculated from momentum p, time-of-flight TOF and path length L as,

$$m^2 = p^2\{\Big(\frac{TOF}{L}\Big)^2 - 1\}. \tag{5.31}$$

Fig. 5.6 shows a scatter plot of squared mass versus signed momentum, positively charged particles (+ sign); negatively charged particles (− sign), in a 9 degrees angle setting at 4 A GeV beam energy.

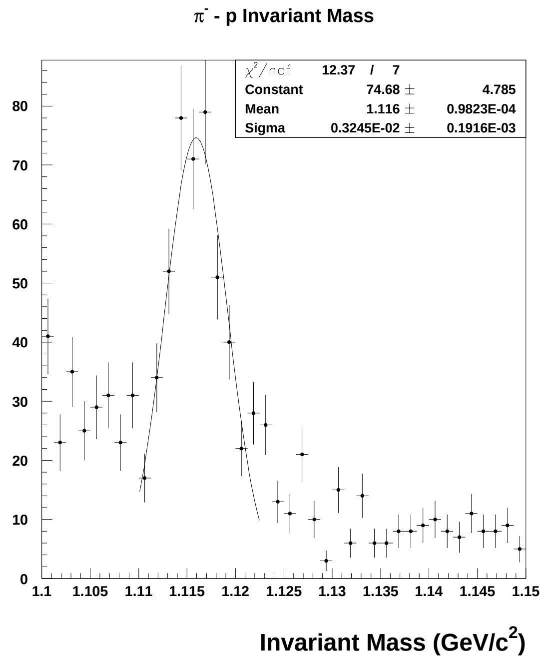

Figure 5.5: The invariant mass distribution of $p - \pi^-$ pairs observed in 4 A GeV Au+Au collisions. The peak corresponds to Λ particle. The peak is fitted to Gaussian function.

The resolution of m^2 is determined by two factors; the momentum resolution of the tracking system and the timing resolution of the time-of-flight system. The momentum resolution σ_p is calculated as,

$$\begin{aligned}
\left(\frac{\sigma_p}{p}\right)^2 &= (C_{ang}p)^2 + \left(\frac{C_{mult}}{\beta}\right)^2, && (5.32)\\
C_{ang} &= \frac{\sigma_\theta}{\Delta p_x} && (5.33)\\
C_{mult} &= \frac{0.0136Z}{\Delta p_x}\sqrt{\frac{x}{X_0}}\left(1 + 0.038ln\frac{x}{X_0}\right), && (5.34)\\
\Delta p_x &= 0.29979 \oint Bydz, && (5.35)
\end{aligned}$$

where p, β, and Z are the momentum [GeV/c], velocity, and the charge of the particle, σ_θ is the intrinsic angular resolution of the tracking system, x/X_0 is the thickness of material in radiation lengths, and C_{ang} and C_{mult} are the contributions of the angular resolution and Multiple Coulomb scattering, respectively. Then the resolution of squared mass σ_{m^2} is written as,

$$\sigma_{m^2}^2 = 4m^4\left(\frac{\sigma_p}{p}\right)^2 + \frac{4p^4}{\beta^2}\left(\frac{\sigma_{TOF}}{L}\right)^2 \qquad (5.36)$$

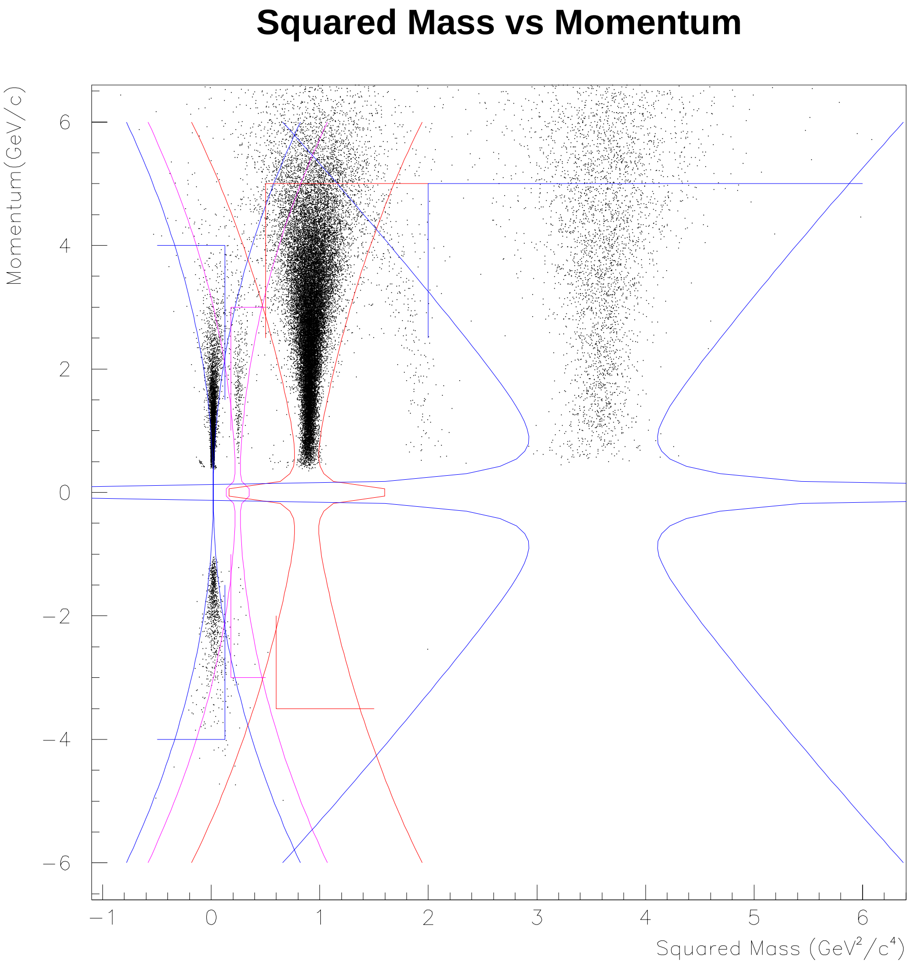

Figure 5.6: A scatter plot of measured squared mass versus signed momentum, positively charged particles (+ sign); negatively charged particles (− sign), in a 9 degrees angle setting at 4 A GeV beam energy. Solid lines represents the applied particle identification cuts.

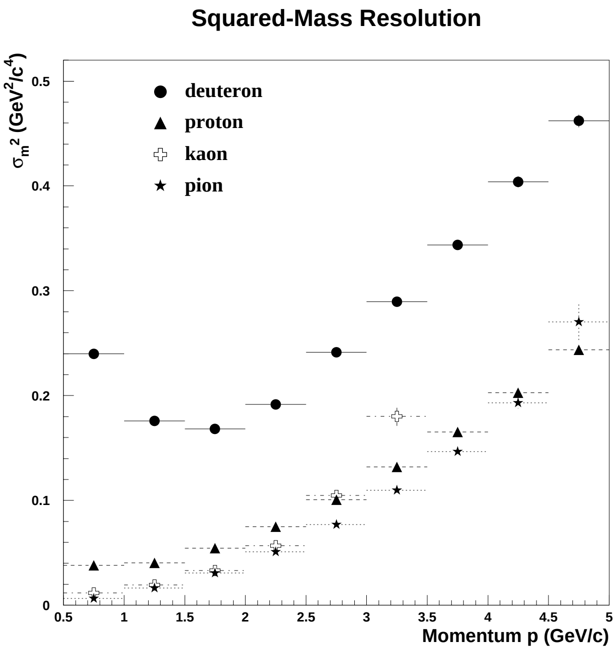

Figure 5.7: The resolution of squared mass for 10 degree run at 11 A GeV beam energy, as a function of momentum for deuterons, protons, kaons and pions. See text for details.

$$= 4m^4p^2 \cdot C_{ang}^2 + 4m^4\left(1+\frac{m^2}{p^2}\right) \cdot C_{mult}^2 + 4p^2(m^2+p^2) \cdot C_{tof}^2 \quad (5.37)$$

$$C_{tof} = \frac{\sigma_{TOF}}{L}, \quad (5.38)$$

where m is the mass of the particle, σ_{TOF} is the time-of-flight resolution, and L is the flight-path length. Fig. 5.7 shows the width of squared mass as a function of momentum for deuterons, protons, K^+ and π^+ using the real data.

The basic boundary of the particle identification is determined using the squared mass resolution as a function of momentum as follows;

$$|m_{\text{measured}}^2 - m_{\text{real}}^2| < 2.5\sigma_{m^2}, \quad (5.39)$$

where m_{measured}^2 is the squared mass calculated from the measured momentum and the measured time-of-flight, m_{real} is the real mass of the particle.

In addition to the boundaries determined with mass square widths, the following boundaries are applied to suppress the contamination of other particle species as in Table 5.2.

Particle	Squared mass boundary [GeV^2/c^4]	Momentum boundary [GeV/c]
π	< 0.125	$0.45 - 4.0$
K	$0.18 - 0.5$	$0.45 - 3.0$
p	$0.5 - 2.0$	$0.45 - 5.0$
d	$2.0 - 6.0$	$0.45 - 5.0$

Table 5.2: Particle identification boundary of squared mass and momentum for π, K, p and d.

5.5 Tracking Efficiency Correction

Track reconstruction efficiency, ϵ_{track} is divided into three parts as,

$$\epsilon_{track} = \epsilon_{FT} \cdot \epsilon_{TPC} \cdot \epsilon_{soft} \tag{5.40}$$

where

ϵ_{FT} : FT hardware efficiency
ϵ_{TPC} : TPC hardware efficiency
ϵ_{soft} : track reconstruction software efficiency.

FT hardware efficiency is regarded as 100 % because the efficiency per plane of FT's is higher than 95 %. FT1 and FT2 are required to have hits at least 6 out of 10 planes, and for FT3 and FT4, they are at least 4 out of 8 planes. Therefore ϵ_{FT} is evaluated as 100 %.

5.5.1 TPC hardware efficiency

TPC hardware efficiency depends on the position of the hits and the momentum of the particle. The position dependence in x-direction of the TPC hardware efficiency is due to field distortion. The y-position dependence of the efficiency is regarded as due to electron diffusion and absorption during drift. The momentum dependence of the efficiency is due to the change of energy deposit of the particle in TPC, dE/dx. Thus the momentum dependence of the efficiency is estimated as a function of $\beta\gamma$, where $\beta = v/c$, and $\gamma = 1/\sqrt{1-\beta^2}$. The TPC hardware efficiency per row is written as;

$$\epsilon_{TPC_{r,x,y}}(\beta\gamma) = 1 - A_{r,x,y} \cdot \mathrm{Ineff}(\beta\gamma), \tag{5.41}$$

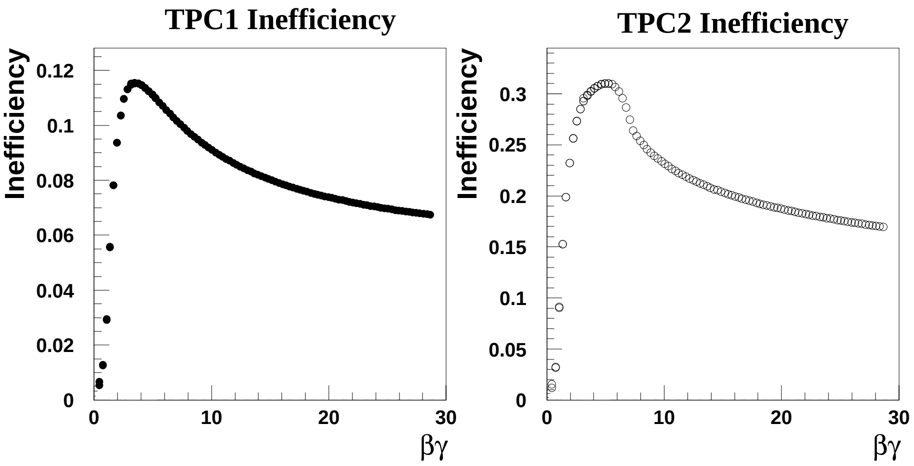

Figure 5.8: Inefficiency of TPC1 and TPC2 as a function of $\beta\gamma$ for deuterons, protons and pions. Inefficiency is averaged in all raws of TPCs.

where suffices r, x and y denote the row number of the TPC, hit position in x-direction and y-direction at each row, respectively, A is the normalization factor indicating the degree of inefficiency, and Ineff$(\beta\gamma)$ is TPC hardware inefficiency averaged over row and hit position. The TPC inefficiency of row i, Ineff$_i$ is calculated as follows;

$$\begin{aligned}\mathrm{Ineff}_i &= 1-\epsilon_{TPC_i}, &(5.42)\\ \epsilon_{TPC_i} &= \frac{\text{No. of tracks with hits on all row } i}{\text{No. of tracks with hits on all rows except row } i}. &(5.43)\end{aligned}$$

Fig. 5.8 shows the averaged inefficiency as a function of $\beta\gamma$ of TPC1 and TPC2, respectively. The TPC hardware efficiency is calculated track by track with $\epsilon_{TPC_{r,x,y}}$ of the hit position as,

$$\epsilon_{TPC} = \epsilon_{TPC^0}+\epsilon_{TPC^1}+\epsilon_{TPC^2}+\epsilon_{TPC^3}, \tag{5.44}$$

where

$$\begin{aligned}\epsilon_{TPC^0} &= \epsilon_1\cdot\epsilon_2\cdot\epsilon_3\cdot\epsilon_4\cdot\epsilon_5\cdot\epsilon_6 &(5.45)\\ \epsilon_{TPC^1} &= (1-\epsilon_1)\cdot\epsilon_2\cdot\epsilon_3\cdot\epsilon_4\cdot\epsilon_5\cdot\epsilon_6\\ &+ \cdots\\ &+ \epsilon_1\cdot\epsilon_2\cdot\epsilon_3\cdot\epsilon_4\cdot\epsilon_5\cdot(1-\epsilon_6) &(5.46)\\ \epsilon_{TPC^2} &= (1-\epsilon_1)\cdot(1-\epsilon_2)\cdot\epsilon_3\cdot\epsilon_4\cdot\epsilon_5\cdot\epsilon_6\\ &+ \cdots\\ &+ \epsilon_1\cdot\epsilon_2\cdot\epsilon_3\cdot\epsilon_4\cdot(1-\epsilon_5)\cdot(1-\epsilon_6) &(5.47)\end{aligned}$$

$$\begin{aligned}\epsilon_{TPC^3} &= (1-\epsilon_1)\cdot(1-\epsilon_2)\cdot(1-\epsilon_3)\cdot\epsilon_4\cdot\epsilon_5\cdot\epsilon_6 \\ &+ \cdots \\ &+ \epsilon_1\cdot\epsilon_2\cdot\epsilon_3\cdot(1-\epsilon_4)\cdot(1-\epsilon_5)\cdot(1-\epsilon_6) \qquad (5.48)\end{aligned}$$

where n of ϵ_{TPC^n} denotes the number of missing rows, ϵ_i $(1 = 1, 2, 3, 4, 5, 6)$, denotes the efficiency at row i.

5.5.2 Track Reconstruction Software Efficiency

Track reconstruction software efficiency due to the multiple Coulomb scattering is evaluated using a Monte Carlo single track of each particle species. A thousand events with single track with a fixed βp are generated with simulation code with multiple scattering switched on or off, respectively. The energy loss is always considered. Furthermore the output of simulation is converted to same data format with real data. Then the track reconstruction is performed with the same tracking code. The software efficiency due to the multiple scattering for a fixed βp is evaluated as;

$$\epsilon_{\text{soft}} = \frac{\text{No. of reconstructed tracks with multi. scattering on}}{\text{No. of reconstructed tracks with multi. scattering off}} \qquad (5.49)$$

In the simulation, Forward Spectrometer is set at 6 degree and the magnetic strength is set to 2 K Gauss and 4 K Gauss for FM1 and FM2, respectively. The magnetic field is set to bent positive particles away from the beam line. Then the single tracks of deuteron, proton or positive pion are generated with a fixed emission angle with θ of 6.5^o and ϕ of 180^o with each βp from 0.2 to 5 GeV/c. The efficiency is parameterized as,

$$\epsilon_{\text{soft}} = a_0 + a_1 log(\beta p), \qquad (5.50)$$

where a_0 and a_1 are fitting parameters. The fitting parameters a_0 and a_1 are 0.967 and 0.0306, respectively. It is found that the efficiency goes down as the βp decreasing, from 99 % to 94 %.

In former analysis by Sako [44], the track multiplicity dependence of the track reconstruction software efficiency has been studied. Fig. 5.9 shows the track reconstruction efficiency as a function of βp for multiplicity 1 (solid), 5 (dashed) and 9 (dotted). The efficiency decreases as the multiplicity increases at momentum higher than 2 GeV/c, while it is stable at momentum less than 2 GeV/c. The number of

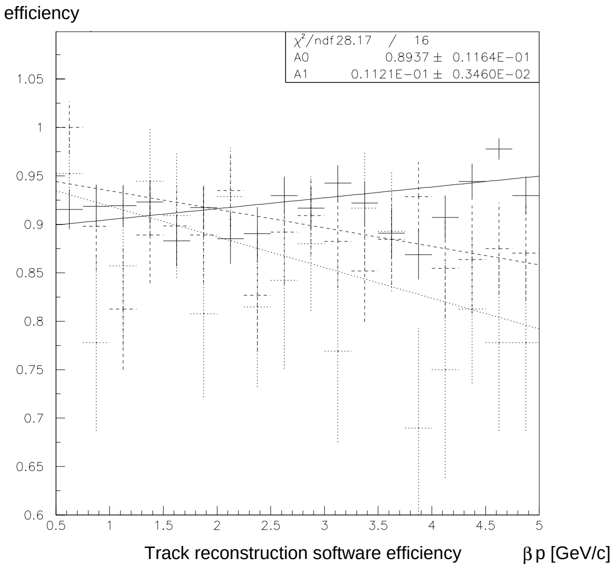

Figure 5.9: Track reconstruction efficiency of anti-protons as a function of βp [GeV/c] for reconstructed track multiplicity of 1 (solid), 5 (dashed), and 9 (dotted) [44]. The efficiency at high βp decreases as the multiplicity increases.

tracks in the inclusive events is less than 2. Thus, the track multiplicity dependence of the software efficiency is small.

5.6 FTOF Detection Efficiency

Since FTOF TDC's do not have a multiple hit capability, if two particles hit the same FTOF slat, only the earlier hit is recorded. We evaluated the inefficiency due to the FTOF occupancy. The inefficiency depends not only on the angle and magnet settings but also on the trigger types.

The efficiency is written as follows;

$$\epsilon_i^{TOF}(t) = 1 - \frac{\int_0^t \frac{dN(t)}{dt} dt}{N_{\mathrm{event}}}, \tag{5.51}$$

where i is a slat number ($0 \le i \le 99$), t is a TDC value [nsec], $\frac{dN(t)}{dt}$ is the particle rate [nsec^{-1}]. One can understand this equation by resolving the inefficiency into two factors as follows;

$$1 - \epsilon_i^{TOF}(t) = \frac{\int_0^t \frac{dN(t)}{dt} dt}{N_i} \times \frac{N_i}{N_{\mathrm{event}}}, \tag{5.52}$$

where N_i represents the number of tracks on slat i. The first factor is the probability that a hit is observed on a slat i at a time earlier than t, namely, the probability that

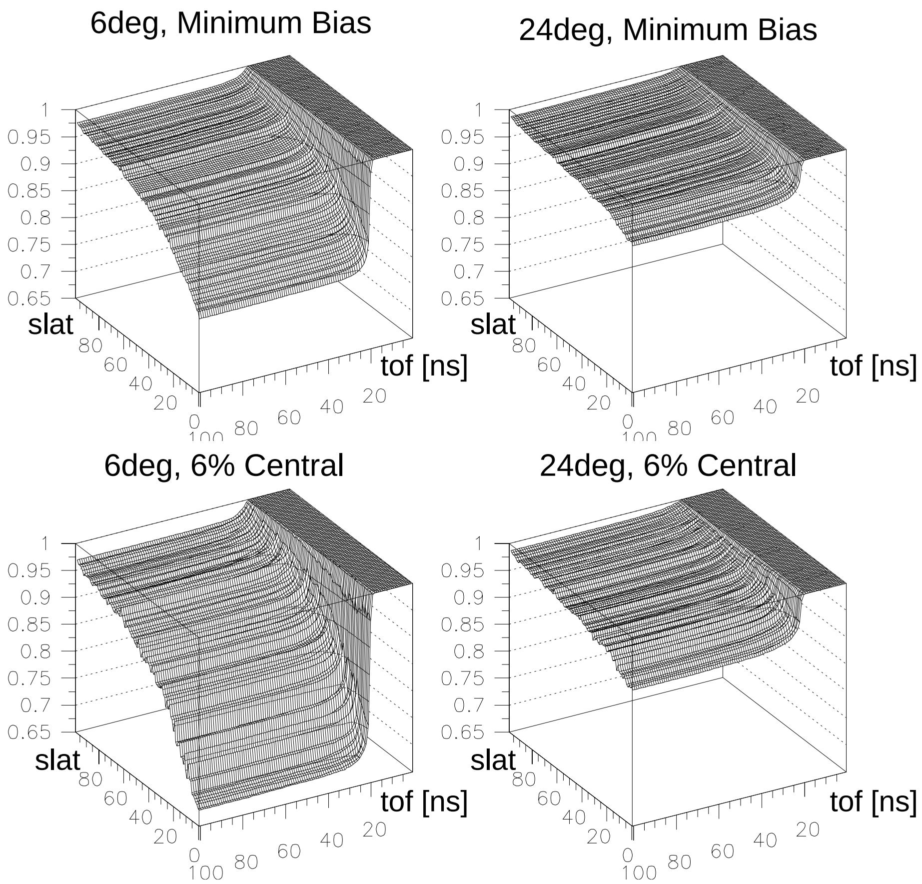

Figure 5.10: FTOF detection efficiency as a function of the slat number (the left-side axis) and a time-of-flight in nsec (the right-side axis). Four plots correspond to $FSPEC$ events at 6 degrees (top left), at 24 degrees (top right), 6 % central events at 6 degrees (bottom left), and at 24 degrees (bottom right) [44].

suppose the first particle hits on slat i at t and the second particle hits the slat, the second particle hits earlier than the first particle. The second factor is the probability that the second particle hits the same slat, i.

We calculate $\epsilon_i^{TOF}(t)$ for all the angle and magnet settings and for minimum bias and several centrality events. Fig. 5.10 shows FTOF detection efficiency as a function of the slat number and the time-of-flight. The efficiency decreases as the TDC value increases, and as the slat number decreases, namely, the slat is closer to the beam. Also the efficiency is lower for central events.

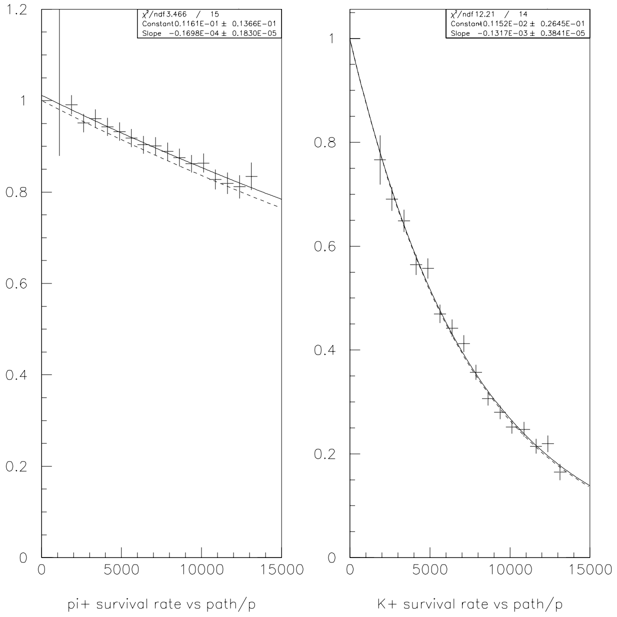

Figure 5.11: Survival rates of π^+ and K^+ after track reconstruction and PID as a function of L/p [mm·c/GeV]. Solid lines show fitted curves, and dashed lines show expected curves from the decay time constants [44].

5.7 Decay Correction

For pions and kaons, we estimate the effect of decay on efficiency. We use Monte Carlo single tracks with and without decay, and calculated the survival rate of them after track reconstruction. The efficiency is defined as follows;

$$\epsilon^{decay} \equiv \frac{\text{No. of PID'ed tracks with decay}}{\text{No. of PID'ed tracks without decay}}. \tag{5.53}$$

We calculate ϵ^{decay} as a function of L/p, where L is the path length, p is the momentum. Fig. 5.11 shows ϵ^{decay} as a function of L/p for π^+ and K^+.

Chapter 6

Experimental Results I – Single Particle Spectra

In this chapter, the procedure to calculate the cross sections and the experimental results of single particle spectra of deuterons, protons, K^+ and $\pi^\pm$ in Au+Au collisions at 4 and 11 A GeV are presented. In Section 6.1, the interaction trigger cross section is defined. In Section 6.2, procedures to evaluate the invariant cross sections is given. The centrality cut criteria is given in Section 6.3. The centrality dependence of transverse mass spectra for d, p, K^+ and $\pi^\pm$ at 4 and 11 A GeV beam energy are presented in Section 6.4. The centrality dependence of rapidity distribution dN/dy and mean transverse mass $< m_t > -m_0$ are presented in Section 6.5 and 6.6, respectively. Finally, the results of single particle spectra are summarized in Section 6.8.

6.1 Interaction Trigger Cross Section

The trigger cross section σ_{trig} of the interaction trigger (INT) is defined as follows.

$$\sigma_{trig} \equiv \left(\frac{S_{trig} N_{trig}}{N_{beam}} - \frac{S^{bg}_{trig} N^{bg}_{trig}}{N^{bg}_{beam}} \right) \frac{10^{24} A}{N_A D} \text{ [barn]}, \tag{6.1}$$

where

N_{beam} : number of beam particles
N_{beam}^{bg} : number of beam particles with empty target
N_{trig} : number of triggers
N_{trig}^{bg} : number of triggers with empty target
S_{trig} : scale-down factor
S_{trig}^{bg} : scale-down factor with empty target
A : mass number of the target nuclei [amu]
N_A : Avogadro's number (6.02×10^{23} [mol^{-1}])
D : the target thickness [g/cm^2].

The calculated the interaction trigger cross section σ_{trig} is 5.3 ± 0.2 barn, which is smaller than the total geometrical cross section (∼ 6.8 barn). This will be due to some of peripheral events are dropped by the BE threshold.

6.2 Invariant Cross Sections

The Lorentz invariant cross section of particle production is described as,

$$E\frac{d^3\sigma}{dp^3} = \frac{d^3\sigma}{p_t dp_t dy d\phi} = \frac{d^3\sigma}{m_t dm_t dy d\phi} \tag{6.2}$$

with transverse momentum p_t or transverse mass $m_t = \sqrt{p_t^2 + m_0^2}$, where m_0, p, E, y, ϕ, is the rest mass, momentum, total energy, rapidity, and azimuthal angle of the particle, respectively. The invariant cross section is evaluated at each rapidity bin and transverse momentum bin, as

$$E\frac{d^3\sigma}{dp^3} = \frac{S_{trig} N_i(y,p_t)}{N_{beam}} \cdot \frac{10^{24} A}{N_A D} \cdot \frac{1}{\epsilon} \cdot \frac{1}{p_t \Delta y \Delta p_t \Delta\phi_i(y,p_t)} \, [\mathrm{barn} \cdot \mathrm{GeV}^{-2}\mathrm{c}^3], \tag{6.3}$$

where S_{beam}, N_{beam}, N_A, and D are as defined in Section 6.1, and $N_i(y,p_t)$ is number of particles ($i = \pi^{\pm}, p, \cdots$), ϵ is total analysis efficiency, Δy is bin size in rapidity, Δp_t is bin size in transverse momentum and $\phi_i(y,p_t)$ is azimuthal acceptance.

For geometrical acceptance calculation, we make acceptance maps for each $y - p_t$ bin by Monte Carlo method. Around the spectrometer aperture, 2 M particles of both charges are generated and tracked using the GEANT [59] without the physical interaction. If the particles are in heavy materials such as the collimator or the frames of the tracking chambers, these particles are forced to stop there. By counting the number of particles which passed all detectors of the Forward Spectrometer, the geometrical acceptance $\Delta\phi/2\pi$ is calculated as a function of momentum and polar emission angle with respect to the incident beam. Then $\Delta\phi/2\pi$ is converted to a function of rapidity and transverse momentum for each particle species. The fiducial cut and the momentum cutoffs are included. The analyzed momentum ranges for various particle species are listed in Table 6.1. Left figures in Fig. 6.1 show samples of the acceptance map, for pions and protons at the 12 degrees angle setting. Right figures in Fig. 6.1 show the statistical errors associated with the calculation of the maps. If the statistical errors are larger than 5% at the edges of the maps, the corresponding bins are rejected.

Particle	Momentum Cutoff range [GeV/c]
$\pi^{\pm}$	0.45 – 4.0
$K^{\pm}$	0.45 – 3.0
p	0.45 – 5.0
d	0.45 – 5.0

Table 6.1: The analyzed momentum ranges for each particle species.

6.3 Centrality Cut Criteria

We define the centrality of events with the total kinetic energy of beam spectators deposited in ZCAL. The procedure to define the centrality is as follows. We first subtract the ZCAL spectrum normalized with $BEAM$ trigger counts in an empty target run from that in a Au target run. We calculate the integral of the ZCAL energy spectrum (software sum), over the ZCAL energy from 0 to z_c. We define the centrality with the integrals as follows;

$$\text{Centrality} \equiv \frac{\int_0^{z_c} \frac{d\sigma_{INT}}{dz} dz}{\int_0^{z_{max}} \frac{d\sigma_{INT}}{dz} dz}. \tag{6.4}$$

Fig. 6.2 shows ZCAL energy spectra for INT events, with a 6-degree, 2A/4A run. Table 6.2 shows the relation between the centrality and its corresponding ZCAL energy at the beam energy of 11 A GeV. We set 4 centrality windows; 0 – 10%, 10 – 30%, 30 – 50%, and 50 – 100% of interaction trigger cross section. Table 6.3 shows the ZCAL energy ranges and mean ZCAL energies in the 4 centrality windows.

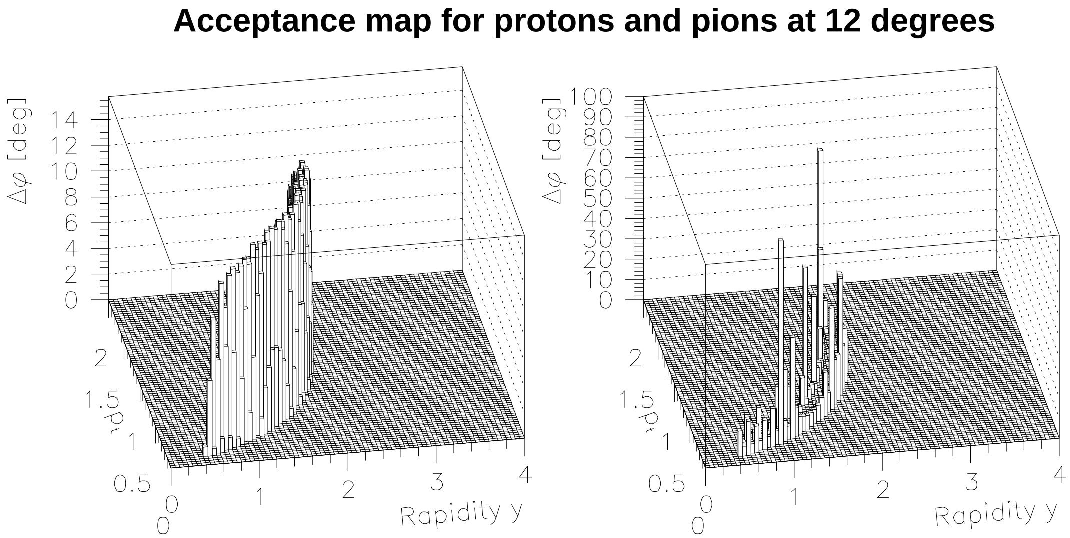

protons **protons, error %**

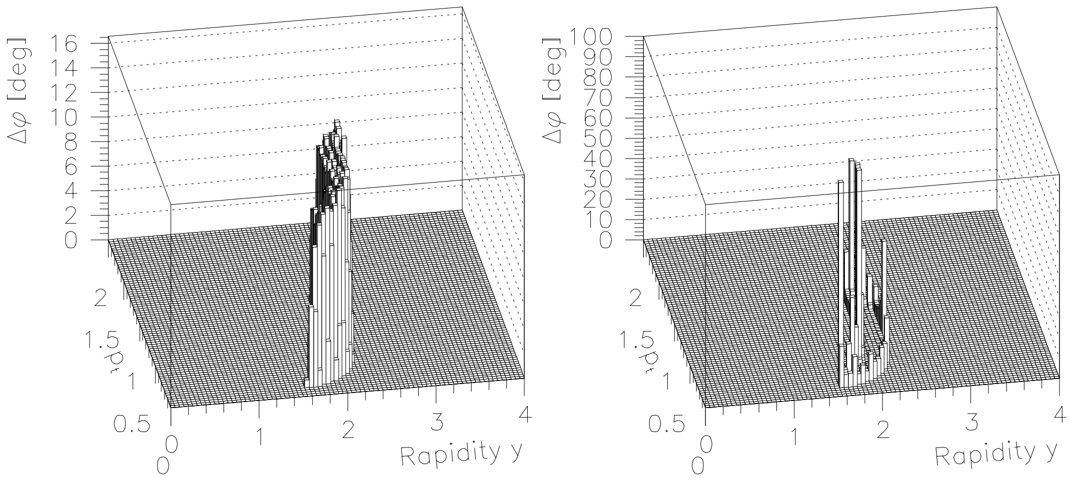

pions(+) **pions(+), error %**

Figure 6.1: Samples of acceptance maps for protons and pions at 12 degrees

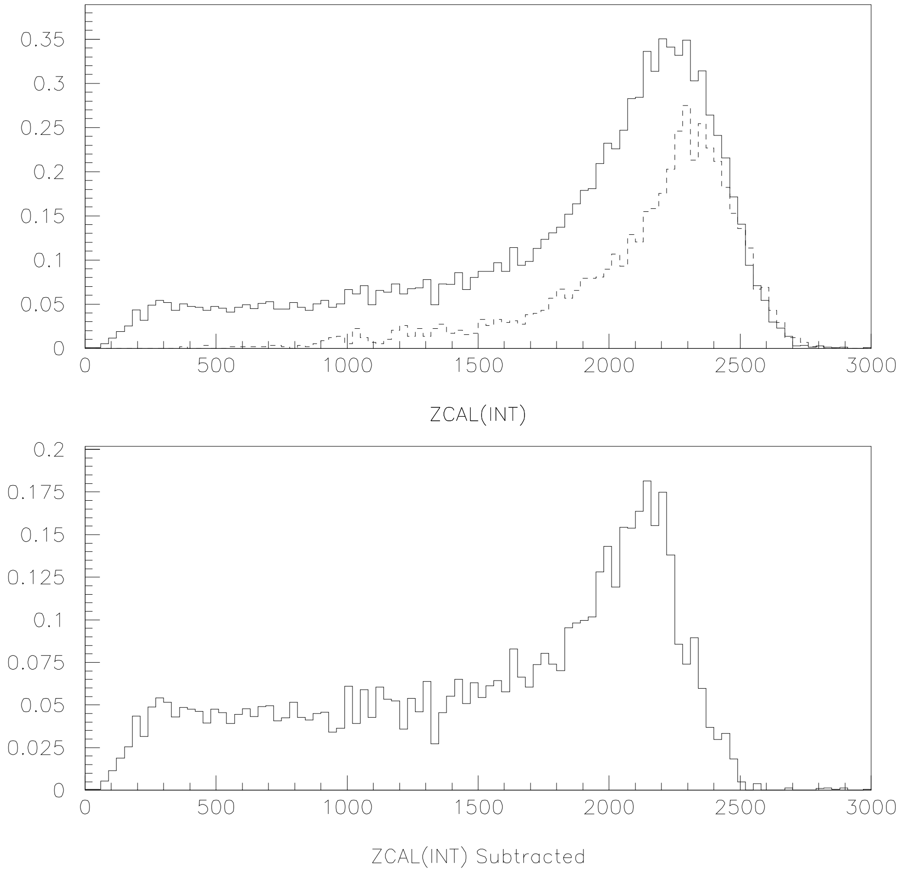

Figure 6.2: ZCAL spectra [GeV] for INT events (top figure, solid line) and for run without the target (top figure, dashed line), normalized with $BEAM$ counts at 11 A GeV beam energy. The net ZCAL spectrum obtain by subtracting the two spectra (bottom figure).

Centrality (0=most central)	ZCAL energy [GeV]
10 %	461
20 %	821
30 %	1114
40 %	1417
50 %	1679
60 %	1845
70 %	1968
80 %	2057
90 %	2147
100 %	3000

Table 6.2: Centrality and ZCAL cut energy.

Centrality range	ZCAL energy range [GeV]	Mean ZCAL energy [GeV]
0 – 10 %	0 – 461	307
10 – 30 %	461 – 1114	803
30 – 50 %	1114 – 1679	1412
50 – 100 %	1679 – 3000	2044
0 – 100 % (Minimum Bias)	0 – 3000	1517

Table 6.3: Centrality ranges and corresponding ZCAL energy ranges and mean ZCAL energies.

At lower beam energy, i.e., $E_{beam} = 4$ A GeV, ZCAL energy is not a good measure for the centrality, because of the aggravation of ZCAL resolution at lower energy. Fig. 6.3 (top) shows the correlation between NMA multiplicity and ZCAL spectra [GeV] at the beam energy of 4 A GeV. The non-linearity can be seen at lower energy of ZCAL spectra. For this reason, NMA multiplicity is used for the centrality cut at 4 A GeV beam energy. Fig. 6.3 (bottom) is the NMA multiplicity distribution after subtraction of the distribution in empty target in INT events. Table 6.4 shows the NMA multiplicity range in the 4 centrality windows.

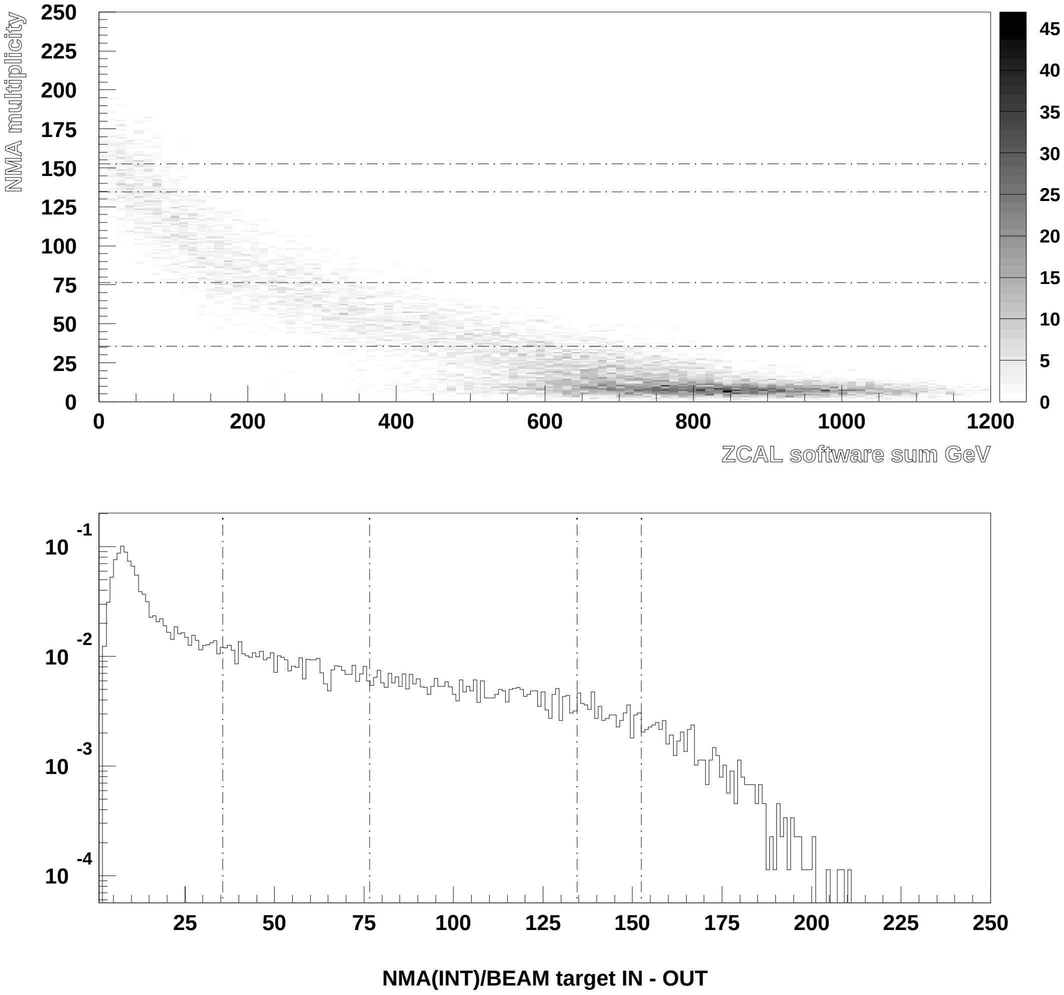

Figure 6.3: The correlation between NMA multiplicity and ZCAL spectra [GeV] at the beam energy of 4 A GeV (top figure). The centrality is defined by the NMA multiplicity distribution after subtraction of NMA distribution in empty target in *INT* events (bottom figure).

6.4 Transverse Mass Spectra

6.4.1 Centrality dependence at $E_{beam} = 4$ A GeV

Fig. 6.4 shows the invariant differential cross sections of protons and deuteron in four centrality bins as a function of transverse kinetic energy near mid-rapidity in Au+Au collisions at 4 A GeV. The invariant differential cross section of $\pi^{\pm}$ and K^{+} are shown in Fig. 6.5 and Fig. 6.6, respectively. Each successive spectrum is divided by 10.

6.4.2 Centrality dependence at $E_{beam} = 11$ A GeV

Fig. 6.7 shows the invariant differential cross sections of protons and deuteron in four centrality bins as a function of transverse kinetic energy near mid-rapidity in Au+Au collisions at 11 A GeV. The invariant differential cross section of $\pi^{\pm}$ and K^{+} are shown in Fig. 6.8 and Fig. 6.9, respectively. Each successive spectrum is divided by 10.

Centrality range	NMA multiplicity
0 – 10 %	134 – 225
10 – 30 %	76 – 134
30 – 50 %	35 – 76
50 – 100 %	0 – 35
0 – 100 % (Minimum Bias)	0 – 225

Table 6.4: Centrality ranges and corresponding NMA multiplicity at 4 A GeV beam energy.

6.5 Rapidity Density Distributions

It is empirically known that the differential cross sections of particles produced from p+p, p+A, and A+A collisions generally show a shape of a single exponential or double exponentials of $m_t - m_0$, where m_0 is mass of each particle species.

When a transverse mass spectrum shows a single exponential form, as is in the case of kaons, we parameterize the spectrum as follows;

$$\frac{d^2\sigma}{2\pi m_t dm_t dy} = N_0 \exp\left(-\frac{m_t - m_0}{T_0}\right), \tag{6.5}$$

where T_0 [GeV/c^2] is called the inverse slope parameter, which is a measure of the temperature of each particle species. The N_0 is obtained by integrating Eq. 6.5 over m_t;

$$\frac{d\sigma}{dy} = \int_{m_0}^{\infty} \frac{d^2\sigma}{2\pi m_t dm_t dy} \cdot 2\pi m_t dm_t = 2\pi N_0 T_0 (T_0 + m_0). \tag{6.6}$$

By substituting N_0 to the Eq. 6.5, we obtain a parameterization of the transverse mass spectrum;

$$\frac{1}{\sigma_{trig}} \cdot \frac{d^2\sigma}{2\pi m_t dm_t dy} = \frac{1}{2\pi T_0 (T_0 + m_0)} \cdot \frac{dN}{dy} \cdot \exp\left(-\frac{m_t - m_0}{T_0}\right), \tag{6.7}$$

where $\frac{dN}{dy} \equiv \frac{1}{\sigma_{trig}} \frac{d\sigma}{dy}$ is called the rapidity density. We obtain dN/dy and T_0 as fit parameters.

When a transverse-mass spectrum is clearly deviated from a single exponential form, as is in the case of protons and pions, we parameterize the spectrum with a double exponential form as follows;

$$\begin{aligned} \frac{1}{\sigma_{trig}} \cdot \frac{d^2\sigma}{2\pi m_t dm_t dy} &= \frac{1}{2\pi T_1 (T_1 + m_0)} \cdot \frac{1}{1+w} \cdot \frac{dN}{dy} \cdot \exp\left(-\frac{m_t - m_0}{T_1}\right) \\ &+ \frac{1}{2\pi T_2 (T_2 + m_0)} \cdot \frac{w}{1+w} \cdot \frac{dN}{dy} \cdot \exp\left(-\frac{m_t - m_0}{T_2}\right). \end{aligned} \tag{6.8}$$

We obtain dN/dy, w, T_1, and T_2 as fit parameters.

6.5.1 Centrality dependence at E_{beam} = 4 A GeV

Fig. 6.10 shows the rapidity density distributions of protons and deuteron in four centrality bins. The rapidity density distributions of $\pi^{\pm}$ and K^{+} are shown in Fig. 6.11 and Fig. 6.12, respectively.

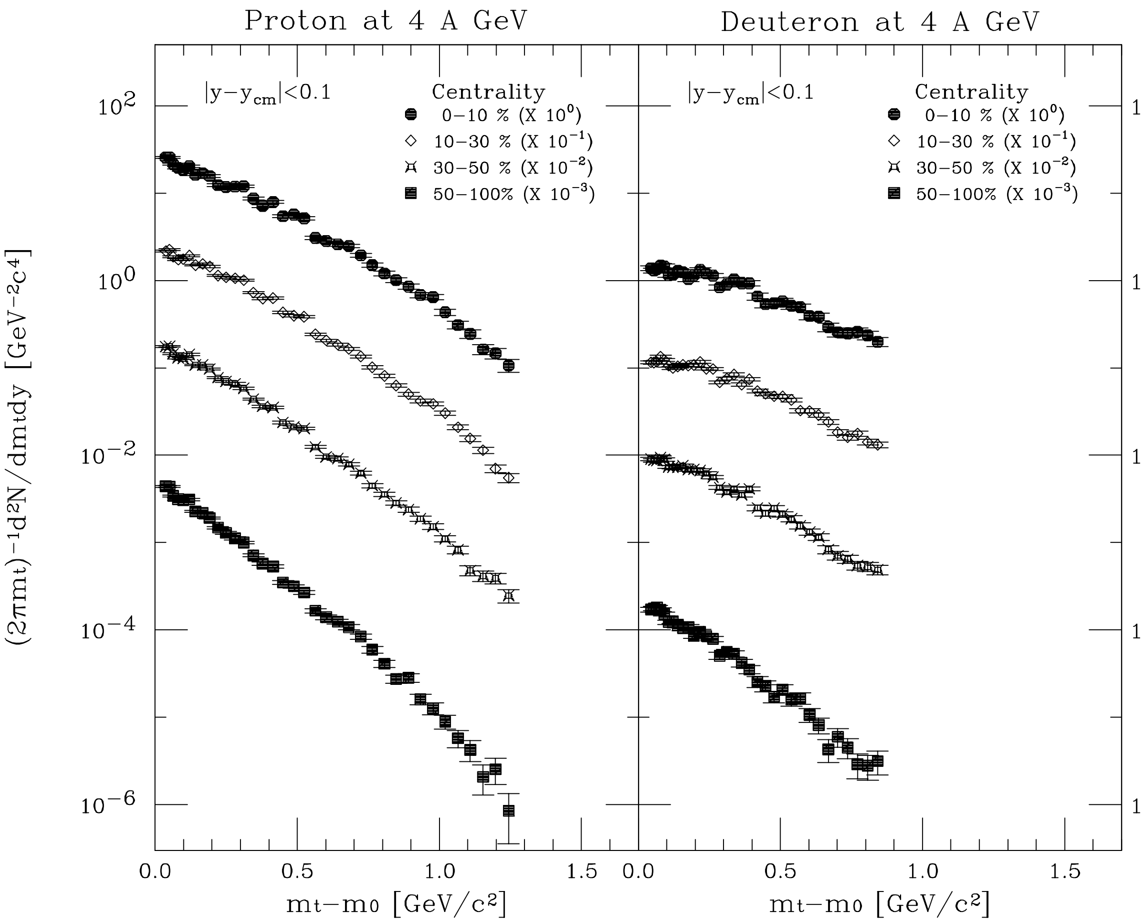

Figure 6.4: Transverse mass spectra of protons (left) and deuterons (right) in four centrality ranges, 0 - 10 %, 10 -30 %, 30 - 50 % and 50 - 100 % near mid-rapidity at 4 A GeV beam energy. The units of the horizontal and the vertical axes are GeV/c^2 and GeV$^{-2}c^4$, respectively. Each successive spectrum is divided by 10.

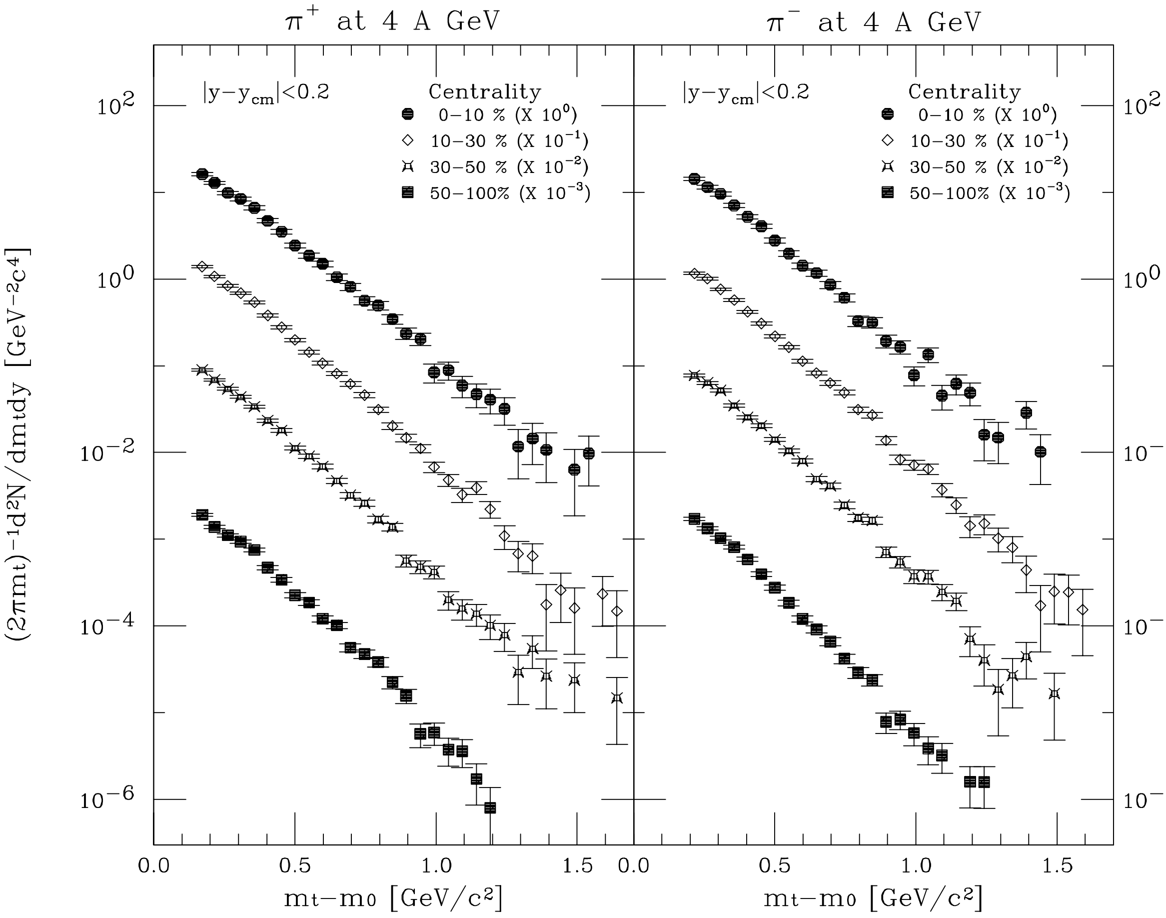

Figure 6.5: Transverse mass spectra of π^+ (left) and π^- (right) in four centrality ranges, 0 - 10 %, 10 -30 %, 30 - 50 % and 50 - 100 % near mid-rapidity at 4 A GeV beam energy. The units of the horizontal and the vertical axes are GeV/c^2 and GeV$^{-2}c^4$, respectively. Each successive spectrum is divided by 10.

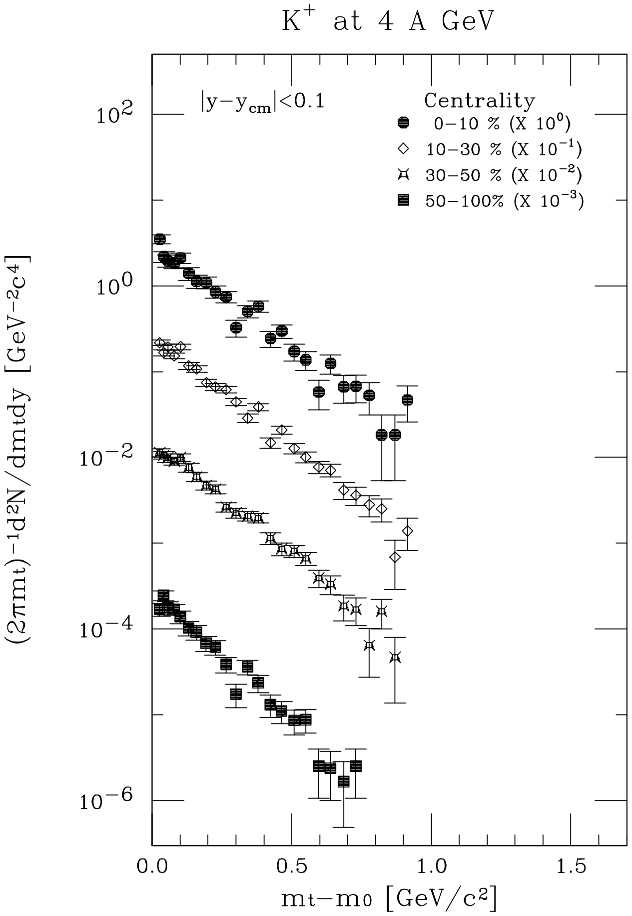

Figure 6.6: Transverse mass spectra of K^+ in four centrality ranges, 0 - 10 %, 10 -30 %, 30 - 50 % and 50 - 100 % near mid-rapidity at 4 A GeV beam energy. The units of the horizontal and the vertical axes are GeV/c^2 and GeV$^{-2}c^4$, respectively. Each successive spectrum is divided by 10.

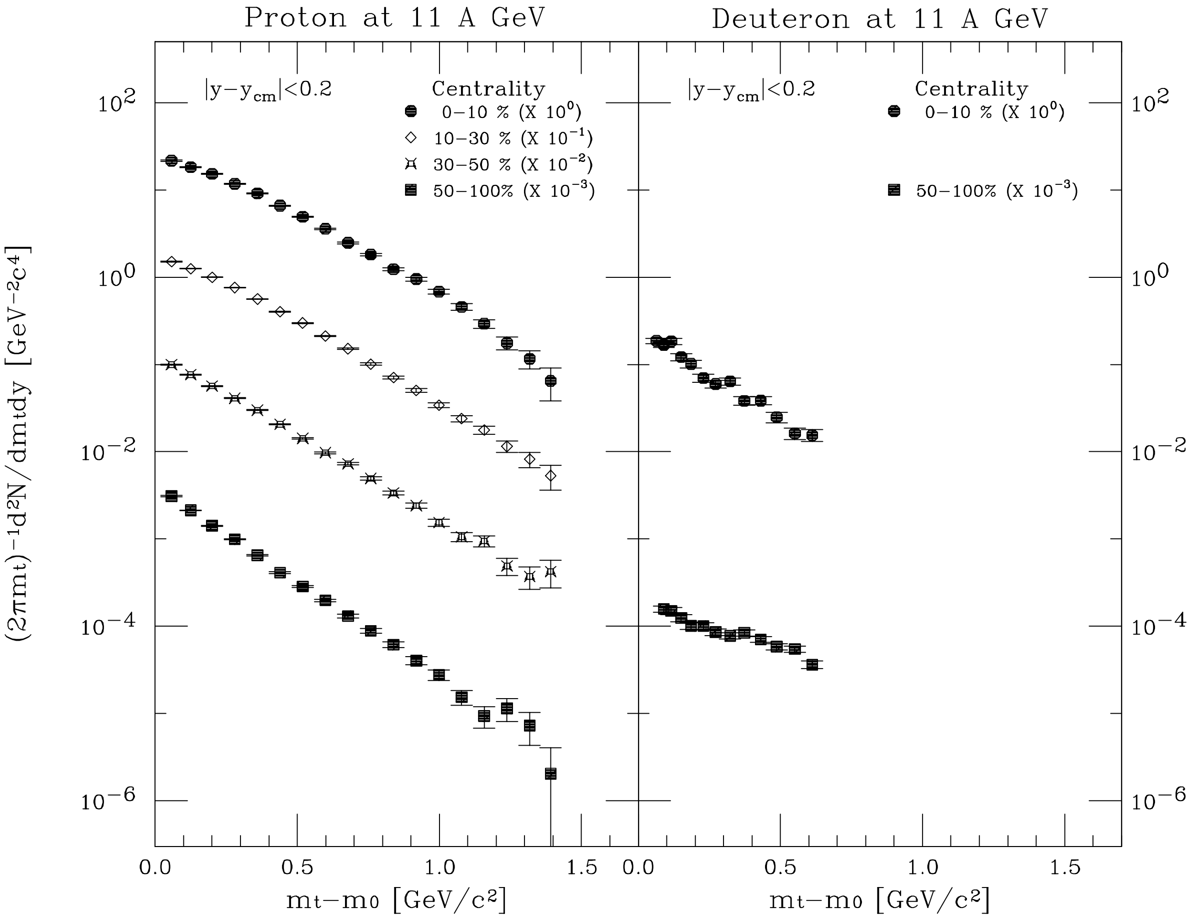

Figure 6.7: Transverse mass spectra of protons (left) and deuterons (right) in four centrality ranges, 0 - 10 %, 10 -30 %, 30 - 50 % and 50 - 100 % near mid-rapidity at 11 A GeV beam energy. The units of the horizontal and the vertical axes are GeV/c^2 and GeV$^{-2}c^4$, respectively. Each successive spectrum is divided by 10.

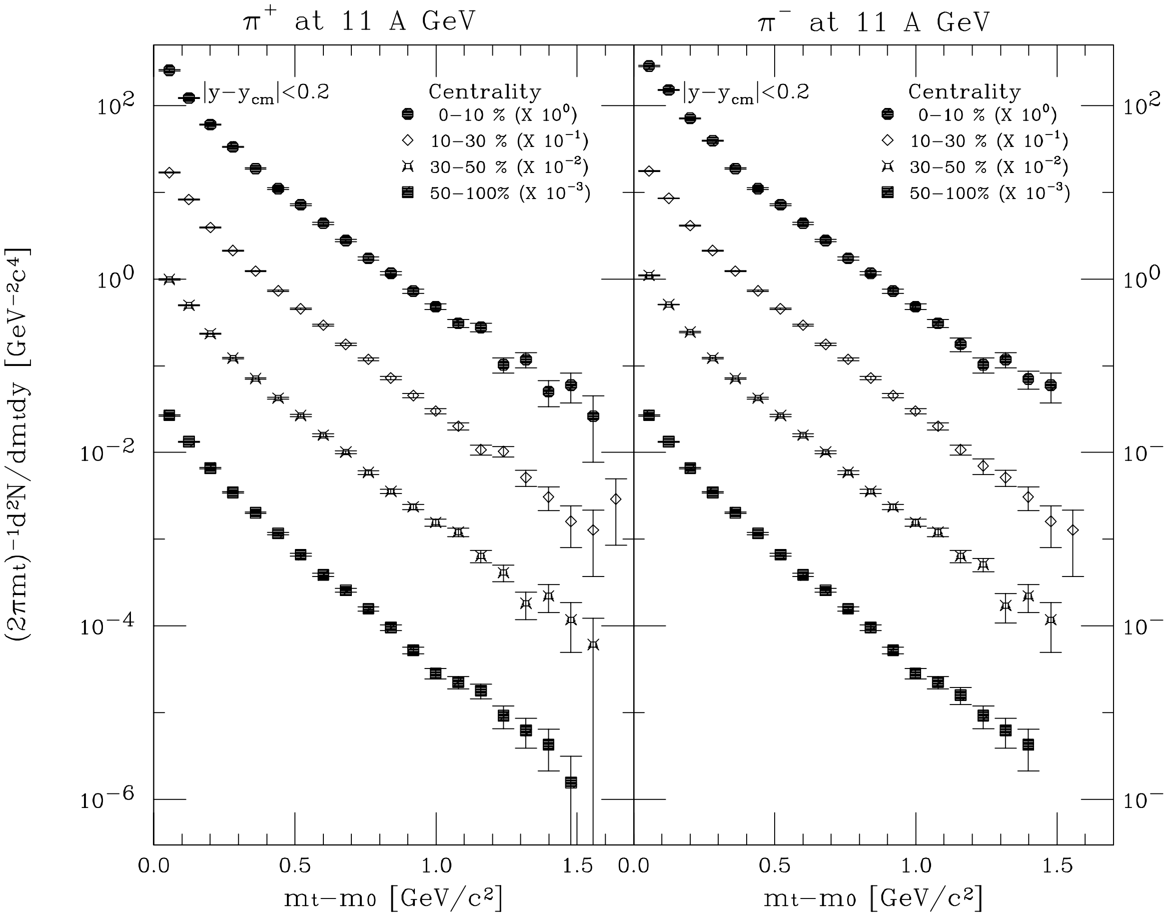

Figure 6.8: Transverse mass spectra of π^+ (left) and π^- (right) in four centrality ranges, 0 - 10 %, 10 -30 %, 30 - 50 % and 50 - 100 % near mid-rapidity at 11 A GeV beam energy. The units of the horizontal and the vertical axes are GeV/c^2 and GeV$^{-2}c^4$, respectively. Each successive spectrum is divided by 10.

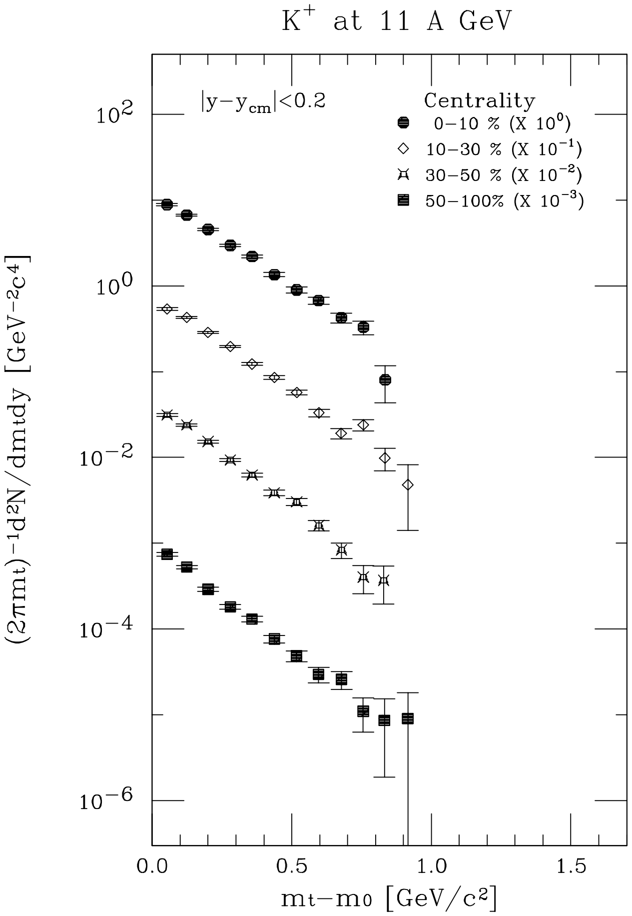

Figure 6.9: Transverse mass spectra of K^+ in four centrality ranges, 0 - 10 %, 10 -30 %, 30 - 50 % and 50 - 100 % near mid-rapidity at 11 A GeV beam energy. The units of the horizontal and the vertical axes are GeV/c^2 and GeV$^{-2}c^4$, respectively. Each successive spectrum is divided by 10.

6.5.2 Centrality dependence at $E_{beam} = 11$ A GeV

Fig. 6.13 shows the rapidity density distributions of protons and deuteron in four centrality bins. The rapidity density distributions of $\pi^{\pm}$ and K^{+} are shown in Fig. 6.14 and Fig. 6.15, respectively.

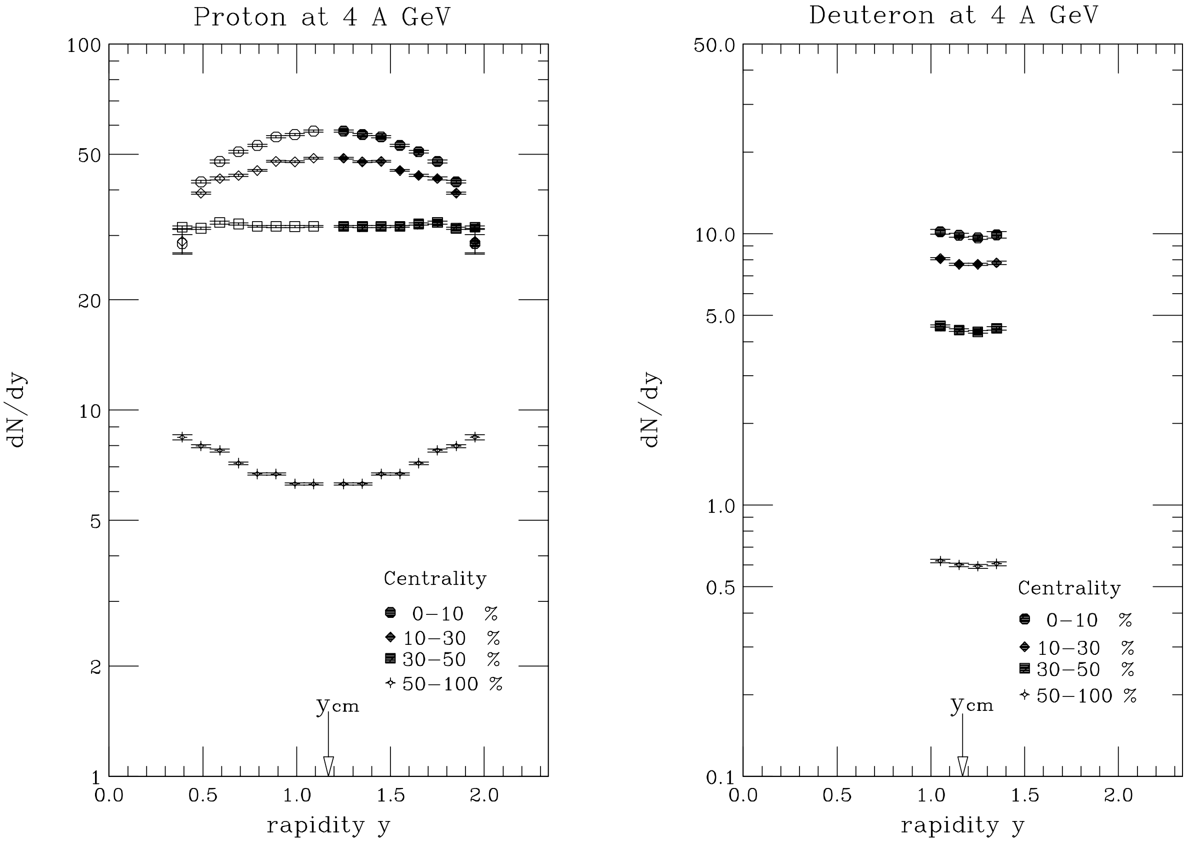

Figure 6.10: Rapidity density distributions of protons(left) and deuterons (right) in four centrality ranges, 0 - 10 %, 10 -30 %, 30 - 50 % and 50 - 100 % at 4 A GeV beam energy.

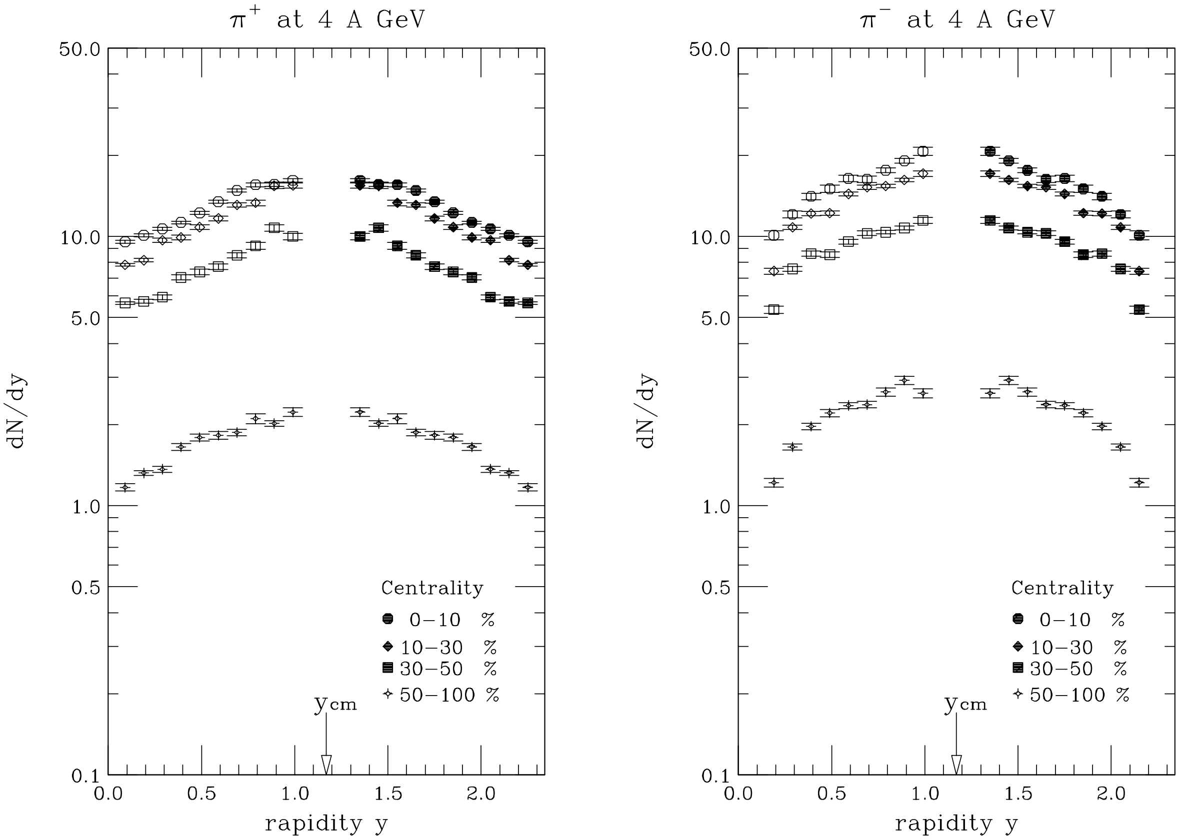

Figure 6.11: Rapidity density distributions of π^+ (left) and π^- (right) in four centrality ranges, 0 - 10 %, 10 -30 %, 30 - 50 % and 50 - 100 % at 4 A GeV beam energy.

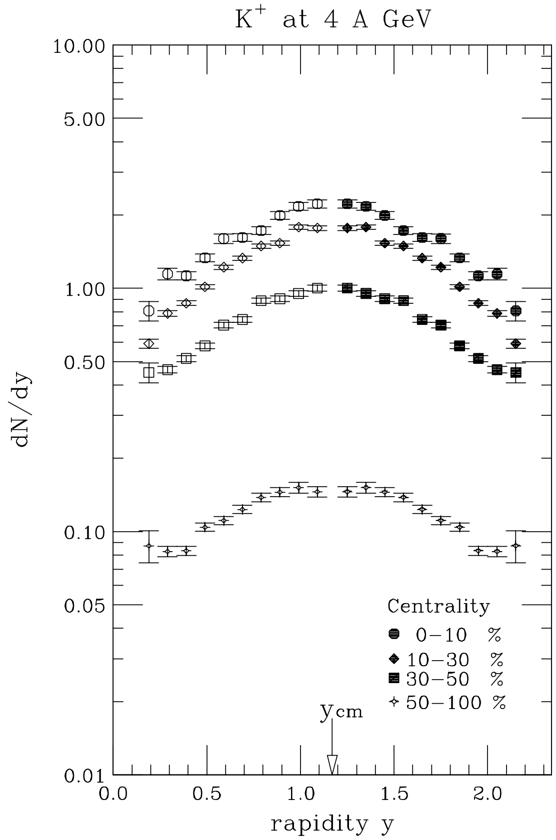

Figure 6.12: Rapidity density distributions of K^+ in four centrality ranges, 0 - 10 %, 10 -30 %, 30 - 50 % and 50 - 100 % at 4 A GeV beam energy.

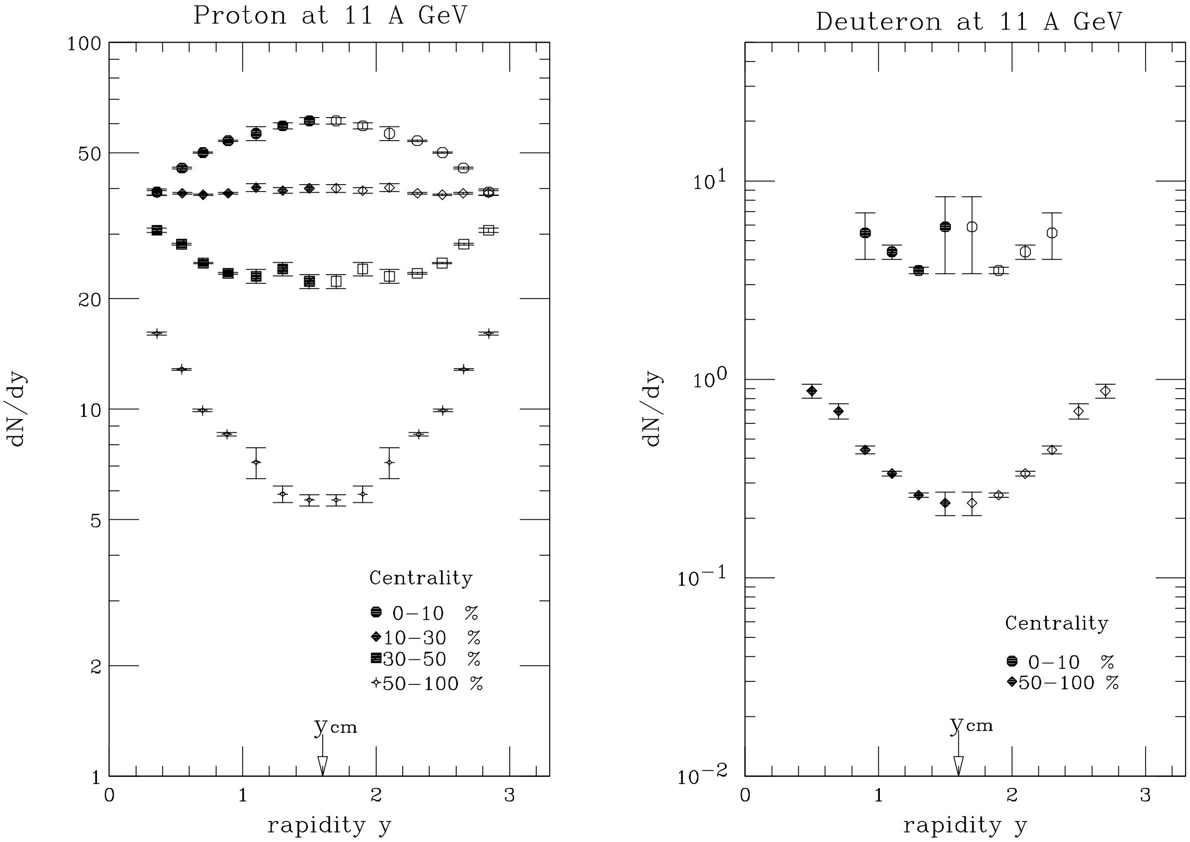

Figure 6.13: Rapidity density distributions of protons (left) and deuterons (right) in four centrality ranges, 0 - 10 %, 10 -30 %, 30 - 50 % and 50 - 100 % at 11 A GeV beam energy.

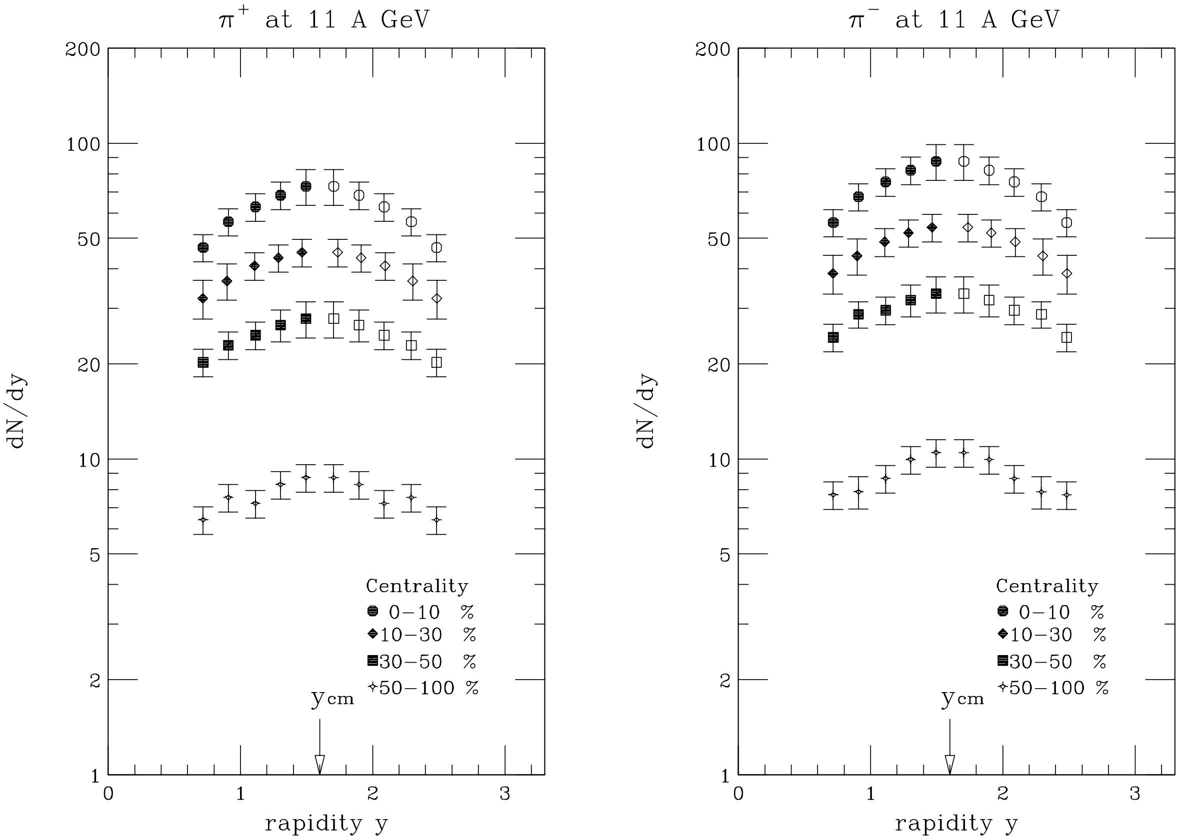

Figure 6.14: Rapidity density distributions of π^+ (left) and π^- (right) in four centrality ranges, 0 - 10 %, 10 -30 %, 30 - 50 % and 50 - 100 % at 11 A GeV beam energy.

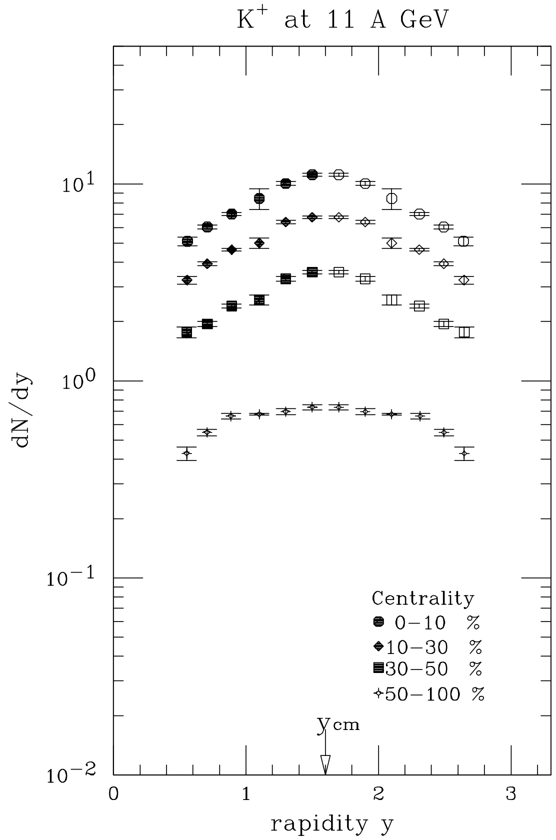

Figure 6.15: Rapidity density distributions of K^+ in four centrality ranges, 0 - 10 %, 10 -30 %, 30 - 50 % and 50 - 100 % at 11 A GeV beam energy.

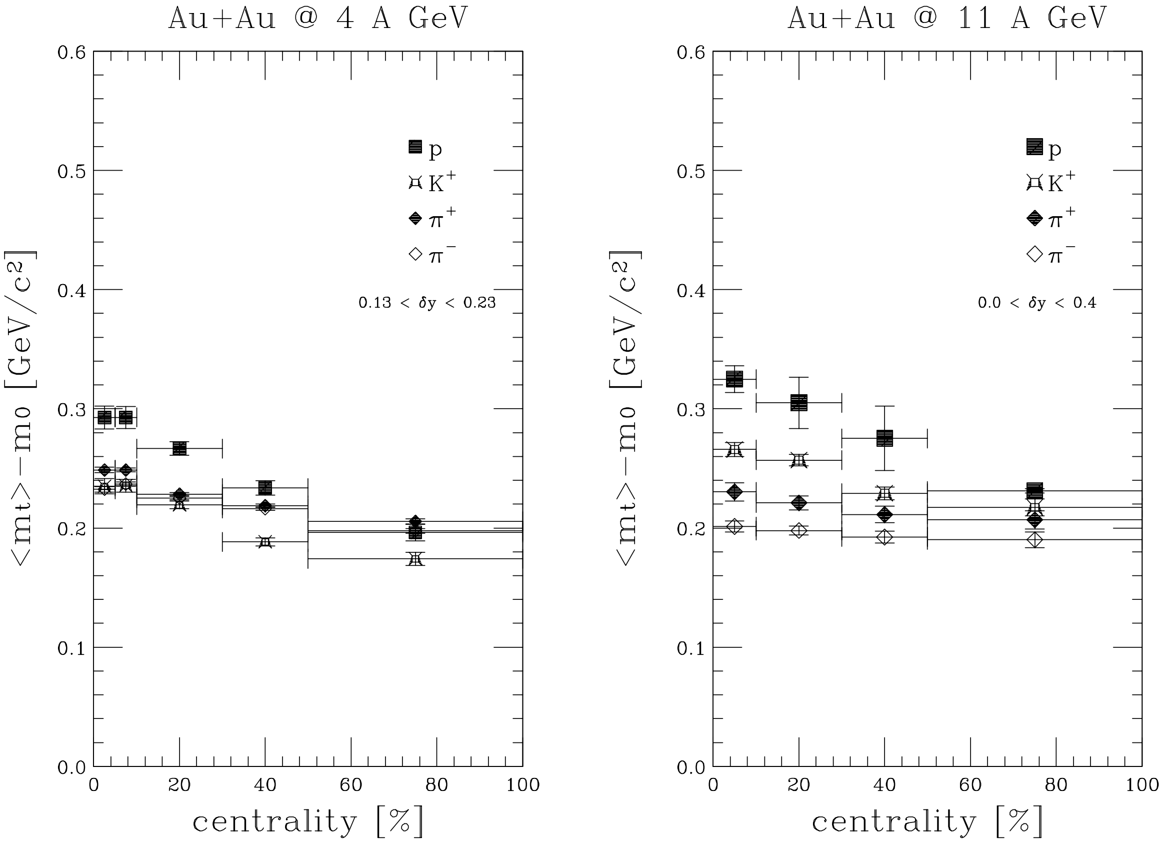

Figure 6.16: $< m_t > -m_0$ [GeV/c^2] of protons, K^+ and $\pi^\pm$ at 4 A GeV beam energy (left) and that at 11 A GeV(right) as a function of centrality given in percentage of interaction trigger cross sections.

6.6 Centrality Dependence of Mean Transverse Mass

In this section, mean transverse mass $< m_t > -m_0$ as a function of centrality. We obtained $< m_t > -m_0$ with the fit parameter of transverse mass spectra of either Eq. 6.7 or Eq. 6.8 for each particle species. Fig. 6.16 shows $< m_t > -m_0$ [GeV/c^2] of deuterons, protons, K^+ and $\pi^\pm$ at 4 A GeV beam energy (left) and protons, K^+ and $\pi^\pm$ at 11 A GeV(right) as a function of centrality near mid-rapidity.

6.7 Systematic Errors

The systematics of the single particle analysis is checked using the kinematic symmetry of the collision system with respect to the center of mass rapidity $y_{\mathrm{cm}} \simeq 1.17$. Fig 6.17 shows the ratios of invariant differential cross sections between kinematic

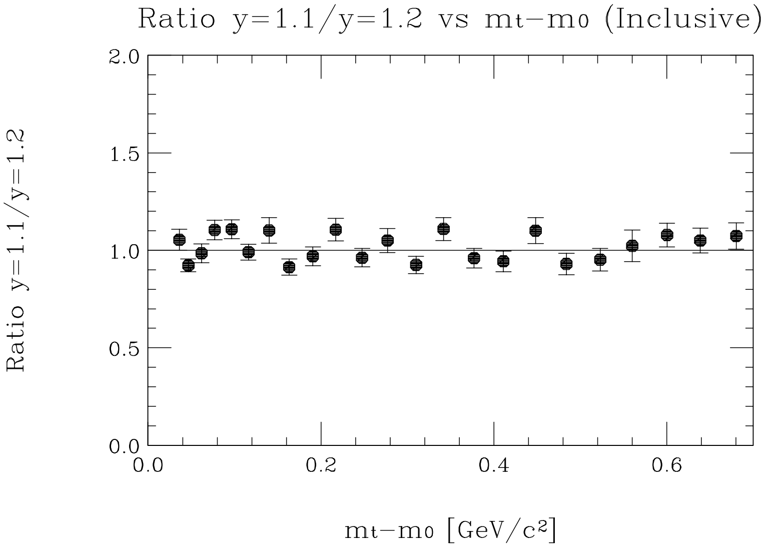

Figure 6.17: Ratio of inclusive proton differential yield at 4 A GeV beam energy between $1.1 < y < 1.2$ and $1.2 < y < 1.3$ as a function of transverse kinetic energy $m_t - m_0$.

reflected rapidity regions as a function of transverse kinetic energy for protons. The error in the figure are the statistical errors of the ratios. The proton differential cross section in the range $1.1 < y < 1.2$ is consistent to that in $1.2 < y < 1.3$ within $\sim 10\%$. The applied corrections and the systematic errors in the analysis are summarized in Table. 6.5. The overall systematic error of the invariant cross sections is estimated to be 8%.

6.8 Summary of the Results for Single Particle Spectra

For single particle analysis, we have measured transverse mass spectra and rapidity distributions dN/dy for $\pi^{\pm}$, K^{+}, protons and deuterons in Au+Au collisions at 4 and 11 A GeV as a function of centrality. For the transverse mass spectra, we have observed the mass dependence of mean transverse mass $< m_t > -m_0$; for the particle with heavier mass, the larger $< m_t > -m_0$ is seen. For the shapes of the spectra, m_t spectra of protons have shoulder-arm shape in central collisions at low m_t region, On the other hand, the pion spectra have an enhancement at low m_t, in other words, the concave shape at low m_t region at 11 A GeV beam energy. Though the enhancement of pions could be explained in part by the contribution from baryon resonances such

	Correction Range	Typical Correction Inclusive	Sys. Error
TPC Hardware Eff.	0 – 7 %	2 %	1 %
Track Recon. Soft. Eff.	1 – 7 %	2 %	5 %
FTOF Detection Eff.	0 – 30 %	7 %	2 %
PID	1 %	1 %	1 %
Sub total	1 – 40 %	12 %	6 %
Acceptance	–	–	5 %
Centrality Cut	–	–	2 %
INT Cross Section	–	–	3 %
Total	1 – 40 %	12 %	8 %

Table 6.5: The table of correction amplitude and systematic errors. The typical corrections are at 14 degrees, with momentum of 2.5 GeV/c.

as Δ, the concave shape can be also reproduced by invoking a transverse velocity field of the system with a freeze-out temperature. This expanding source picture can also explain observed shoulder-arm shapes in m_t spectra for protons and deuterons, and the mass dependence of the mean transverse mass. For the proton's dN/dy, the distributions have a maximum at mid-rapidity at both 4 and 11 A GeV beam energy in central events, which indicates a large baryon stopping in Au+Au collisions at AGS energies.

Chapter 7

Experimental Results II – Two-Particle Correlations

In this chapter, experimental results of two-particle correlations for $\pi^+\pi^+$ pairs in Au+Au central collisions at 11 A GeV beam energy are presented. After the descriptions of Coulomb correction and cut criteria applied in the analysis, the experimental results of two-particle correlations are shown in two different frame.

7.1 Coulomb Correction

Experimentally, the normalized two-particle correlation function is obtained from the ratio between correlated and uncorrelated particle distribution as,

$$\begin{aligned} C_2(Q \equiv p_1 - p_2) &= \frac{dN/d^3p_1 d^3p_2}{dN/d^3p_1 \cdot dN/d^3p_2} && (7.1) \\ &= A(Q)/B(Q). && (7.2) \end{aligned}$$

where $A(Q)$ is the measured two particle probability distribution as a function of relative four-momentum $Q = p_1 - p_2$, and $B(Q)$ is the uncorrelated (background) distribution, calculated in the same way but using two particles taken from different events.

First, we consider the two particle as $p_1 = (E_1, p_{x1}, p_{y1}, p_{z1}) = (E_1, \vec{p_1})$ and $p_2 = (E_2, p_{x2}, p_{y2}, p_{z2}) = (E_2, \vec{p_2})$. We define the variable $\vec{Q}, Q_0$ and Q_{inv} as,

$$\vec{Q} = \vec{p_1} - \vec{p_2} = (Q_x, Q_y, Q_z), \qquad (7.3)$$

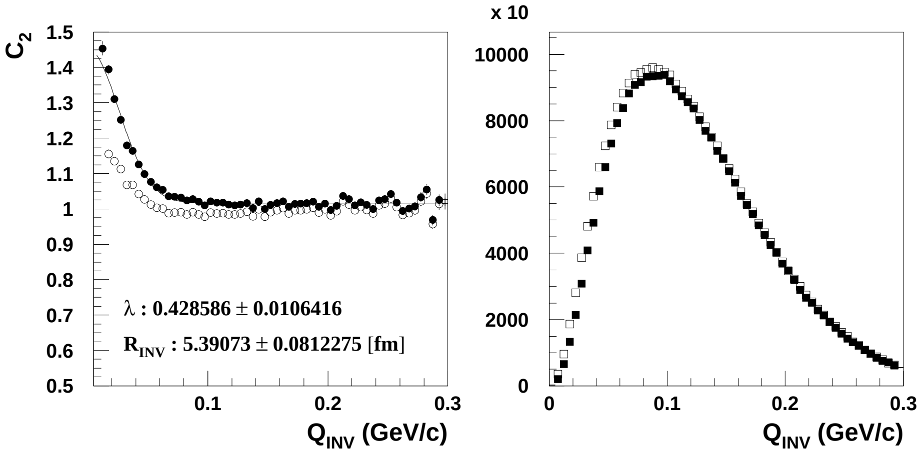

Figure 7.1: Left panel: Correlation functions for $\pi^+\pi^+$ pairs as a function of Q_{inv}. Open circles correspond to the data before Coulomb correction, filled circles correspond to that of after standard Gamov Coulomb correction. Right panel: Q_{inv} distribution of real data with standard Gamov Coulomb correction (open square) and normalized mixed background (filled square).

$$\begin{aligned} Q_0 &= E_1 - E_2, && (7.4) \\ Q_{inv} &= \sqrt{Q_x^2 + Q_y^2 + Q_z^2 - Q_0^2} && (7.5) \end{aligned}$$

The right panel of Fig. 7.1 shows Q_{inv} distribution of $\pi^+\pi^+$ pair of real data with standard Gamov Coulomb correction (open square) and normalized mixed background (filled square).The ratio of the two distributions give the normalized correlation function C_2 as a function of Q_{inv} as shown in the left panel of Fig. 7.1.

To calculate the two-particle correlation function C_2 for identical boson, we assume that particles suffer no final state interaction after emission. However for the experimental analysis of HBT, the Coulomb interaction between these charged particles in the final state is not negligible. The Coulomb repulsion effect suppresses the pair of lower relative momentum. To extract the "true" information of the source from the correlation function, the Coulomb correction must be incorporated. In this analysis, the standard Gamov correction is applied on a pair-by-pair bias in real data used to correct the Coulomb effect in the correlation function.

The method of the standard Gamov correction is as follows. The correction factor depends only the relative momentum difference, $Q = p_1 - p_2$. The standard Gamov correction factor is expressed as,

$$G(\eta) = \frac{2\pi\eta}{e^{2\pi\eta} - 1} \qquad (7.6)$$

where $\eta = m\alpha/Q$, with a particle mass m and the fine structure constant α. The Gamov factor G is the square of the relative Coulomb wave-function of a particle pair at zero separation in configuration space. Using Eq. 7.6, the Gamov factor is weighted in real event in pair-by-pair bias as a function of Q_{inv}. For three dimensional decomposition of Q as described in Section 7.4, the Gamov factor is weighted in each Q_i bin calculated by the corresponding Q_{inv} as,

$$C_2(Q_i) = C_2^{raw}(Q_i) \times G^{-1}(Q_{inv}). \tag{7.7}$$

The left panel in Fig. 7.1 shows the correlation function as a function of Q_{inv} with and without the standard Gamov Coulomb correction.

While the assumptions of a non-relativistic and point-like source made in the formulation of the standard Gamov factor are perhaps appropriate for the sources investigated in e^+e^- or proton-proton collisions, they are certainly not valid for the sources created in the relativistic heavy-ion experiments at AGS and SPS.

NA49 collaboration has been extracted the effects of the Coulomb interaction from correlations between *measured* "$+-$" charged pairs in the experiment [17]. Because opposite sign pions do not exhibit a Bose-Einstein correlation, any signal obtained by this method may be interpreted as due to the Coulomb effect.

The Coulomb correction applied in NA49 is based on the correlation function of the correlation of "$+-$" pairs in the variable Q_{inv} with the same cuts used in the calculations of a conventional correlation function. The Coulomb correction is then parameterized in an analytic form, and the factor is weighted for each pair in terms of their Q_{inv}. The phenomenological Coulomb correction is taken as an exponentially damped Gamov factor as;

$$(G(\eta) - 1)\exp^{-Q_{inv}/Q_{eff}} + 1, \tag{7.8}$$

where $G(\eta)$ is the Gamov factor as defined in Eq. 7.6, and Q_{eff} is a parameter that is fit to the data. We call this type of correction factor as "modified Gamov factor". In the limit of $Q_{eff} \to \infty$, the correction approaches the Gamov factor (a point like source), while in the limit of $Q_{eff} \to 0$, the function goes to 1 (an infinite source). Fig. 7.2 shows the Coulomb correction factor as a function of Q_{inv} in standard Gamov (solid line) and modified Gamov (broken line) Coulomb correction. In general the factor in standard Gamov correction is bigger than that in the modified Gamov correction, and the effect is not vanished in high Q_{inv} region in standard Gamov correction.

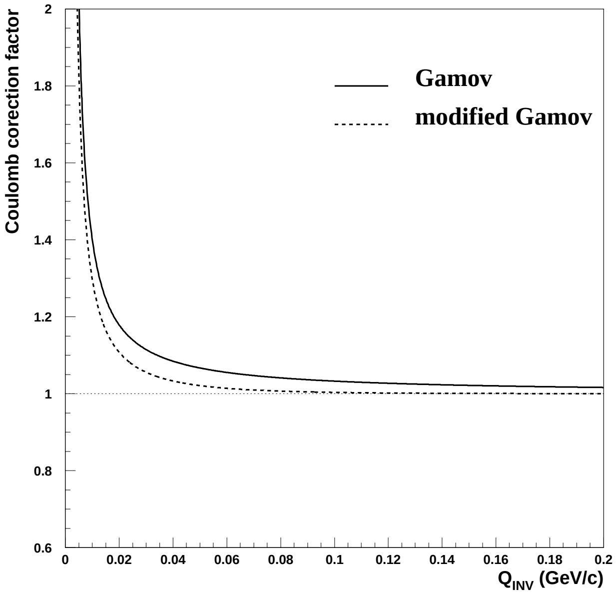

Figure 7.2: Coulomb correction factor as a function of Q_{inv} in standard Gamov (solid line) and modified Gamov (broken line) method.

Fig. 7.3 shows the correlation function C_2 as a function of Q_{inv} with standard Gamov correction, modified Gamov correction and without Coulomb correction. For C_2 with modified Gamov correction, the value of Q_{eff} is set as 46 MeV, which is used in the NA49 two-particle correlation analysis in Pb+Pb collisions [60]. The extracted R_{inv} parameters in modified Gamov Coulomb correction is 10 % larger than that in standard Gamov method. This uncertainty due to the difference of two types of Coulomb corrections is included as the systematic error in this analysis.

7.2 Cut Criteria

7.2.1 Two-track separation

Due to the finite resolution of two-track separation in the Forward Spectrometer, we have to take into account the cut of the close tracks of pair, for the the correlation function. Fig. 7.4 and Fig. 7.5 show the distributions of $\pi^+\pi^+$ pair as a function of the position difference of the two-particle in x and y direction at the mid-plane of each TPC in 1-dimensional and 2-dimensional mesh.

The position difference of a pair at TPCs in x and y directions, i.e.,

$$\Delta X = |x_1 - x_2|, \tag{7.9}$$

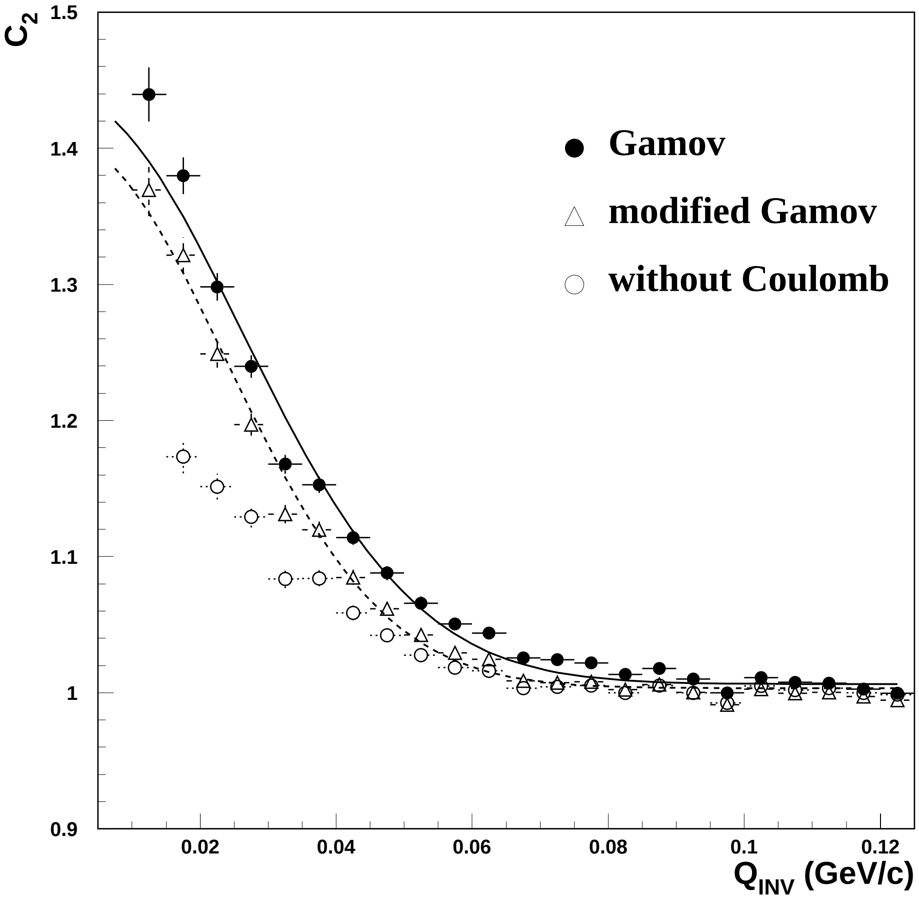

Figure 7.3: The correlation function C_2 as a function of Q_{inv} with standard Gamov correction (solid circles), modified Gamov correction (open triangles) and without Coulomb correction (open circles). The fitting results by the function, $C_2(Q_{inv}) = 1 + \lambda \exp(-R_{inv}^2 Q_{inv}^2)$ to data are also shown. For C_2 with modified Gamov correction, the value of Q_{eff} in Eq. 7.8 is set as 46 MeV, which is used in the NA49 two-particle correlation analysis in Pb+Pb collisions [60].

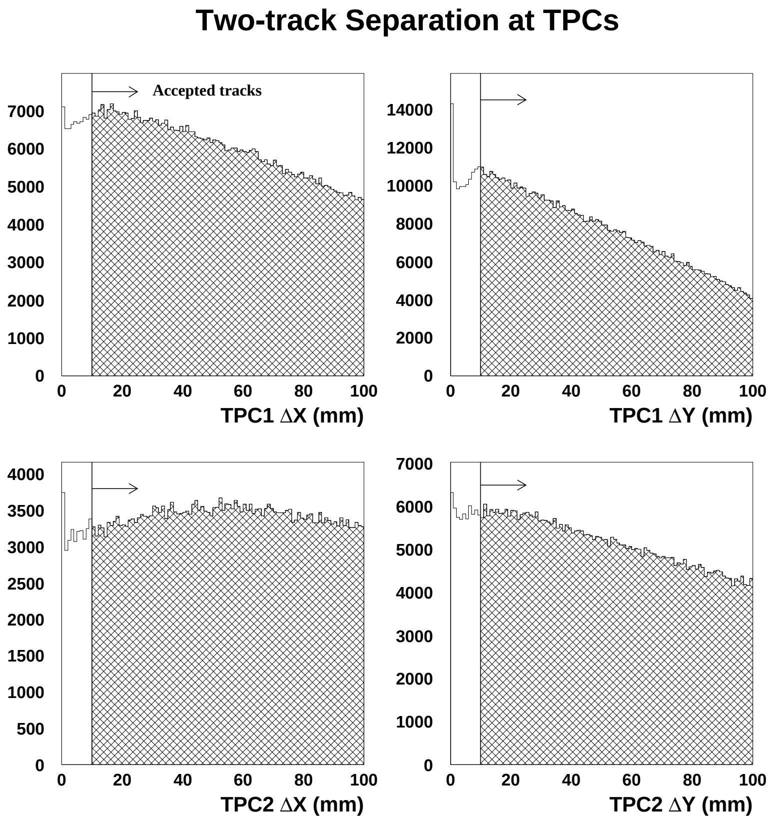

Figure 7.4: The distributions of $\pi^+\pi^+$ pairs as a function of the position difference of the two-particle in x and y direction at the mid-plane of each TPC. The hatched area are accepted as a track for the calculation of correlation function, if the other directions and TPC planes are also within the cut criteria. The unit in the figures is [mm].

$$\Delta Y \quad = \quad |y_1 - y_2|, \tag{7.10}$$

are used for the cut. As shown in Fig. 7.5, the resolution of two track separation is estimated ~ 1 [cm], we set the cut-off parameter as 1 [cm] in both x and y directions at each TPC.

7.2.2 Other cuts

In addition with the cut of two-track separation, it is applied that the rapidity cut due to the limited acceptance and centrality cut for the selection of 10 % central by $ZCAL$ as,

- Rapidity cut : $1.6 < Y_{\pi\pi} < 2.3$

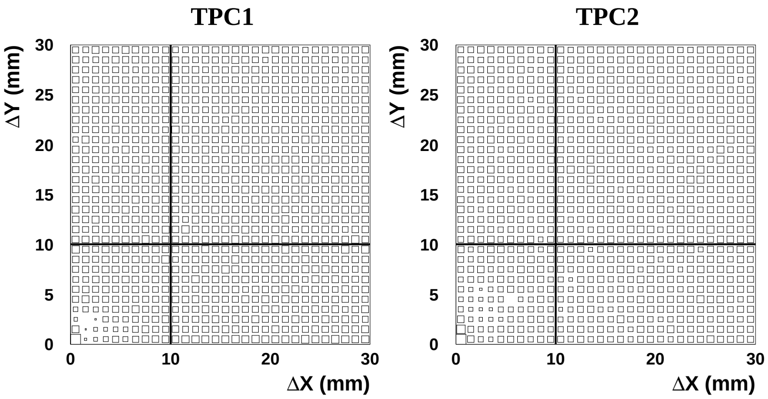

Figure 7.5: The distributions of $\pi^+\pi^+$ pairs as a function of the position difference of the two-particle in 2-dimensional $(x - y)$ mesh at TPC1 (left) and TPC2 (right). The lines in the figures represent the boundary for the two-track separation cut.

- Centrality cut : 10 % most central event selection by $ZCAL$

By these cuts, the event of the most central and near mid-rapidity can be selected.

7.3 Statistics and Event Mixing

As described in Chapter 4, we used the data set 23.6 M in $\overline{ZCAL}$ trigger event for high statistic $\pi^+\pi^+$ two-particle correlations analysis. After the several cuts and the Coulomb correction, the extracted $\pi^+\pi^+$ pairs in Au+Au 10% most central collisions at 11 A GeV are about 2.5 M.

In order to calculate the correlation function, the uncorrelated distribution of pion pairs is needed for the normalization. A convenient way is to make the uncorrelated distribution from different events with the same cut criteria, called the event mixing method.

In this analysis, the event mixing has been done by sampling in each successive five event, and make the pair from different event in the same way as making combination for the real events. The mixed event distribution is normalized by the factor, which is obtained by the ratio of entries between the real and mixed events.

7.4 Parameterization

In this section, we describe the two different parameterization, Yano-Koonin Podgoretskii (YKP) parameterization and the standard side-out-long parameterization.

7.4.1 YKP parameterization

For extraction of the source parameters from the correlation functions, we employ the Gaussian approximation in a representation given by Heinz [16] that is reveal longitudinal collective motion. This parameterization is known as "Yano-Koonin Podgoretskii parameterization" [15], and we abbreviate it as "YKP" hereafter.

The YKP parameterization procedure uses a Gaussian fit for the two-particle correlation function in boost invariant form. The relative momentum of a pair, Q is decomposed into Q_T, Q_L and Q_0, where the momentum difference of transverse direction, that of longitudinal direction and the energy difference of the two particles, respectively. The frame is set in the local center of mass system of the pair. The fitting function in YKP parameterization can be expressed as,

$$\begin{aligned} C_2(Q_T, Q_L, Q_0; K_T) &= 1 + \lambda \exp\Big[-Q_T^2 R_T^2 \\ &\quad - \gamma_{YK}^2 \Big(Q_L - \beta_{YK} Q_0\Big)^2 R_L^2 \\ &\quad - \gamma_{YK}^2 \Big(Q_0 - \beta_{YK} Q_L\Big)^2 R_0^2\Big]. \end{aligned} \tag{7.11}$$

This expression is the explicit function of the energy difference Q_0, transverse momentum difference of $Q_T = \sqrt{Q_x^2 + Q_y^2}$, longitudinal momentum difference $Q_L = Q_z$. The fitting parameters in this parameterization are correlation intensity parameter λ, source size parameters; R_T, R_L, R_0 and Yano-Koonin velocity β_{YK}, which describes the source's longitudinal collective motion.

7.4.2 Standard side-out-long parameterization

Another parameterization, which is often used in 3-dimensional HBT analysis is the standard side-out-long parameterization[1] .

In this parameterization, the frame is chosen the Longitudinal Center of Mass System (LCMS), which defined as $p_{1z} + p_{2z} = 0$. As illustrated in Fig. 7.6, the relative

---

[1] This parameterization is also call as Bertsch-Pratt parameterization.

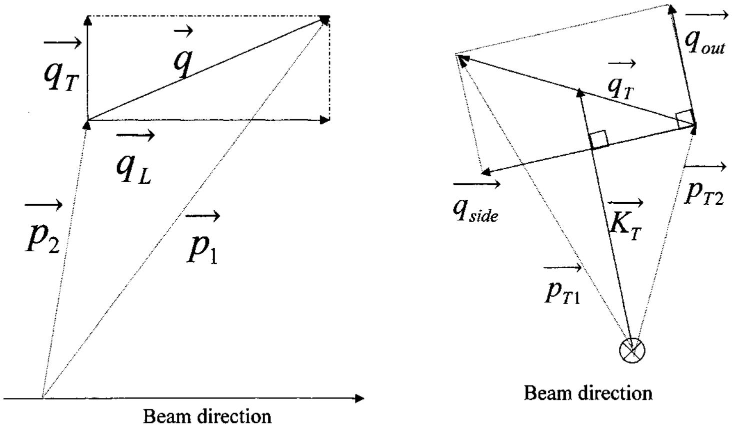

Figure 7.6: The illustration of the standard side-out-long parameterization. See text for detail descriptions.

momentum can be decomposed into $\vec{Q}_L$ and $\vec{Q}_T$, where $\vec{Q}_L$ is parallel to the beam axis and $\vec{Q}_T$ is perpendicular to the beam axis. The same decomposition can be done with the average momentum $\vec{K} = \frac{1}{2}(\vec{p}_1 + \vec{p}_2)$, the corresponding notation is $\vec{K}_L$ and $\vec{K}_T$. The transverse component $\vec{Q}_T$ can be decomposed further into $\vec{Q}_{side}$ and $\vec{Q}_{out}$, where $\vec{Q}_{out}$ is parallel to $\vec{K}_T$ and $\vec{Q}_{side}$ is perpendicular to $\vec{K}_T$. For the longitudinal direction, the suffix is replaced from L to *long*, $Q_L \to Q_{long}$. The fitting function of the standard side-out-long parameterization in the Gaussian approximation can be expressed as,

$$C_2(Q_{side}, Q_{out}, Q_{long}; K_T) = 1 + \lambda \exp(-Q_{side}^2 R_{side}^2 - Q_{out}^2 R_{out}^2 - Q_{long}^2 R_{long}^2). \quad (7.12)$$

The fitting parameters are λ, R_{side}, R_{out} and R_{long}.

7.5 Results in YKP Parameterization (K_T dependence of R_T)

In this section, the results of averaged momentum K_T dependence of R_T parameter in YKP parameterization are presented. First, we define the class of K_T range. Fig. 7.7 shows the K_T distribution of $\pi^+\pi^+$ pairs. The distribution is divided in three different class of K_T range, as listed in the Table 7.1.

Fig. 7.8 shows correlation functions in YKP parameterization as a function of Q_T in three different K_T range; (I) the low K_T region (top left), (II) the mid K_T region (top right) and (III) the high K_T region (bottom left). For the other two variables, Q_L, Q_0 are projected on Q_T axis, if $|Q_L|, |Q_0|$ are less than 50 MeV/c.

For the fitting function, number of parameters in Eq. 7.11 can be reduced by limiting Q_0 and Q_L variables. We use the fitting function to extract the R_T parameter as,

$$C_2(Q_T; K_T) = 1 + \lambda \exp(-Q_T^2 R_T^2). \tag{7.13}$$

In Fig. 7.8, the fitting results are also shown in each panel. The extracted R_T parameters are plotted as a function of K_T in Fig. 7.9. It is observed that the gradual decrease of R_T from 5.21 ± 0.17 fm to 3.73 ± 0.26 fm with increasing K_T from 0.1 GeV/c to 0.45 GeV/c.

As shown in section 7.1, Coulomb correction is important for the extraction of source parameters from two-particle correlations. In order to check the effect of Coulomb correction, R_T parameters in each K_T range with modified Gamov Coulomb correction are extracted. Fig. 7.10 shows the two-particle correlation functions in YKP parameterization in two different Coulomb corrections; standard Gamov (solid circles) and modified Gamov (open circles) correction. Fig. 7.11 shows the K_T dependence of R_T parameters in standard Gamov correction and modified Gamov correc-

Class	K_T range [GeV/c]
Class I	0.1 – 0.25
Class II	0.25 – 0.35
Class III	0.35 – 0.45

Table 7.1: The class of K_T range.

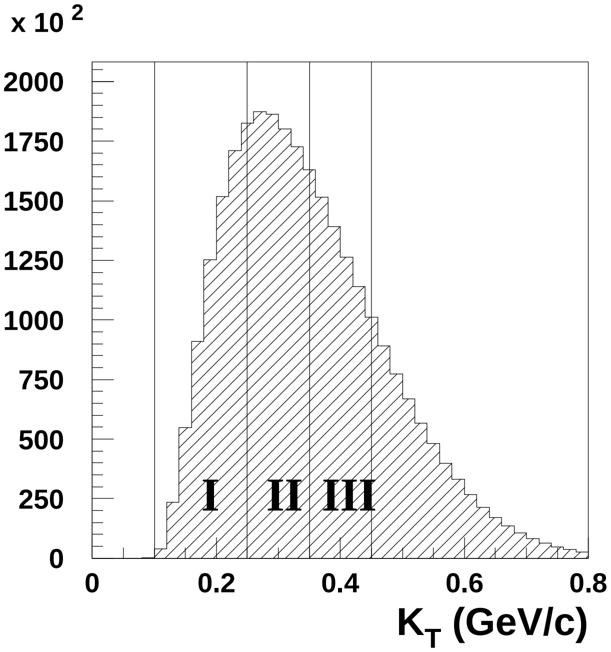

Figure 7.7: The averaged transverse momentum K_T distribution of $\pi^+\pi^+$ pairs. The distribution is divided in three different class of K_T range, as listed in the Table 7.1.

tion. For modified Gamov correction, Q_{eff} is set as 46 MeV, which is used in NA49 Pb+Pb collisions HBT analysis. The extracted source size parameters are listed in Table 7.2. The extracted R_T in modified Gamov correction are larger than that in standard Gamov correction and depend on the range of K_T. In K_T range I and II, it is about 2.5 % and in range III, it is estimated about 1.0 %. These uncertainty caused by coulomb correction are included as an systematic error for the model fitting in Chapter 8.

	Standard Gamov		Modified Gamov	
K_T Class	R_T [fm]	λ	R_T [fm]	λ
I	5.21 ± 0.17	0.39 ± 0.01	5.34 ± 0.19	0.35 ± 0.01
II	4.64 ± 0.27	0.30 ± 0.02	4.76 ± 0.31	0.26 ± 0.02
III	3.73 ± 0.26	0.46 ± 0.04	3.75 ± 0.28	0.41 ± 0.03

Table 7.2: Extracted R_T and λ parameters in two different Coulomb correction, standard Gamov and modified Gamov correction.

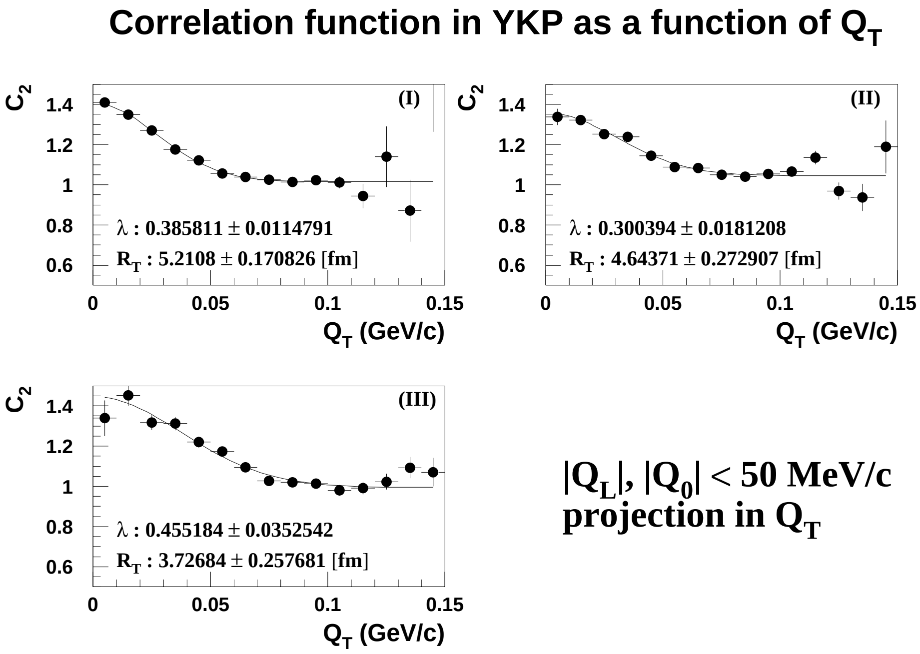

Figure 7.8: $\pi^+\pi^+$ correlation functions in Au+Au central collisions at 11 A GeV beam energy. The correlation functions are presented in YKP parameterization as a function of Q_T in three different K_T range; the low K_T region (I; top left), the mid K_T region (II; top right) and the high K_T region (III; bottom left). For the other two variables, Q_L, Q_0 are projected on Q_T, if $|Q_L|, |Q_0| < 50$ MeV/c. Solid curves in the panels represent the fitting results by Eq. 7.13 and the numbers correspond to the extracted fitting parameters, λ and R_T [fm] are also shown.

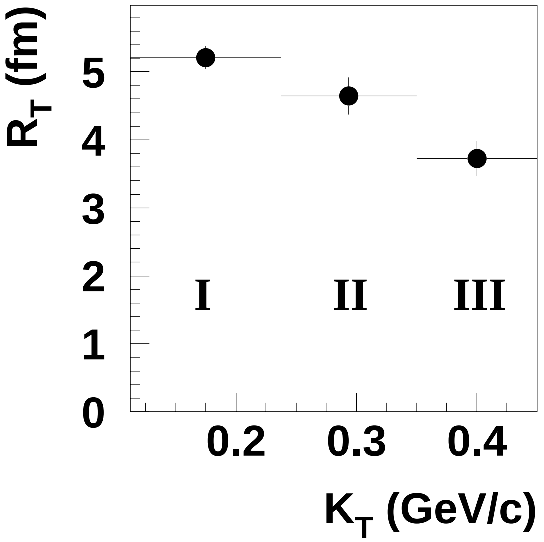

Figure 7.9: K_T dependence of R_T parameters extracted in YKP parameterization. The error bars indicate the statistical errors only.

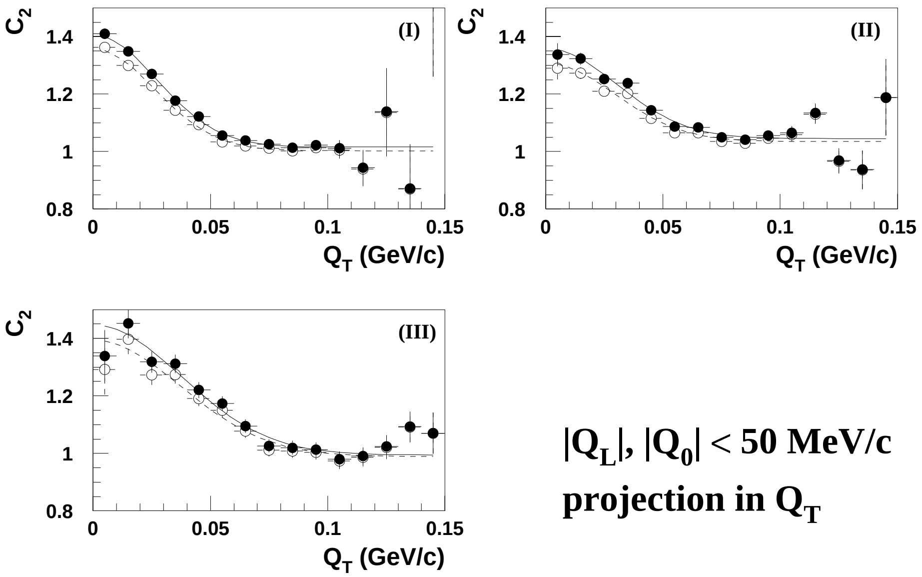

Figure 7.10: Two-particle correlation functions (YKP parameterization) in two different Coulomb corrections, standard Gamov (solid circle) and modified Gamov (open circle) correction in three K_T ranges. The fitting results by Eq. 7.13 to the data are also shown.

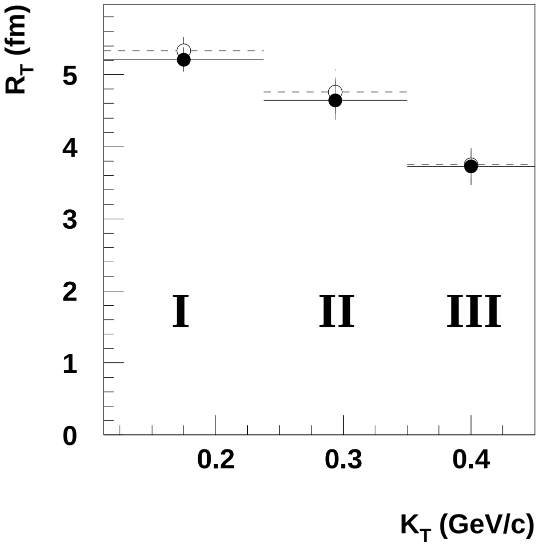

Figure 7.11: K_T dependence of R_T parameters extracted in two different Coulomb corrections, standard Gamov correction (solid circles) and modified Gamov correction (open circles) with $Q_{eff} = 46$ MeV in Eq. 7.8, respectively. The error bars indicate the statistical errors only.

7.6 Results in the Standard Side-Out-Long Parameterization

To check the consistency, the correlation functions in the standard side-out-long parameterization are studied using the same data set and the same cut criteria, which is used in the HBT analysis in YKP parameterization. Fig 7.12 shows the correlation functions in the standard side-out-long parameterization. From left to right in the figure, the correlation function as a function of Q_{side}, Q_{out} and Q_{long} are shown. From top to bottom, C_2 functions at each K_T range, classified in Table 7.1 are arranged. These correlation functions in Q_i is obtain by the limited in $|Q_j|, |Q_k| < 50$ MeV/c where i, j and k indicate "*side*", "*out*" and "*long*".

The extracted source size parameters, R_{side}, R_{out} and R_{long} are plotted as a function of K_T in Fig. 7.12 and these values are listed in Table 7.3. It is observed that the gradual decrease of all source size parameters with increase of the average transverse momentum of pair, and it is consistent with the results obtained in the YKP parameterization.

K_T range	R_{side} [fm]	R_{out} [fm]	R_{long} [fm]
I ($0.1 < K_T < 0.25$ GeV/c)	4.71 ± 0.50	4.27 ± 0.12	3.71 ± 0.20
II ($0.25 < K_T < 0.35$ GeV/c)	4.24 ± 0.57	3.33 ± 0.13	3.20 ± 0.20
III ($0.35 < K_T < 0.45$ GeV/c)	3.17 ± 0.35	3.47 ± 0.22	2.66 ± 0.20

Table 7.3: Extracted source size parameters in the standard side-out-long parameterization at each K_T range.

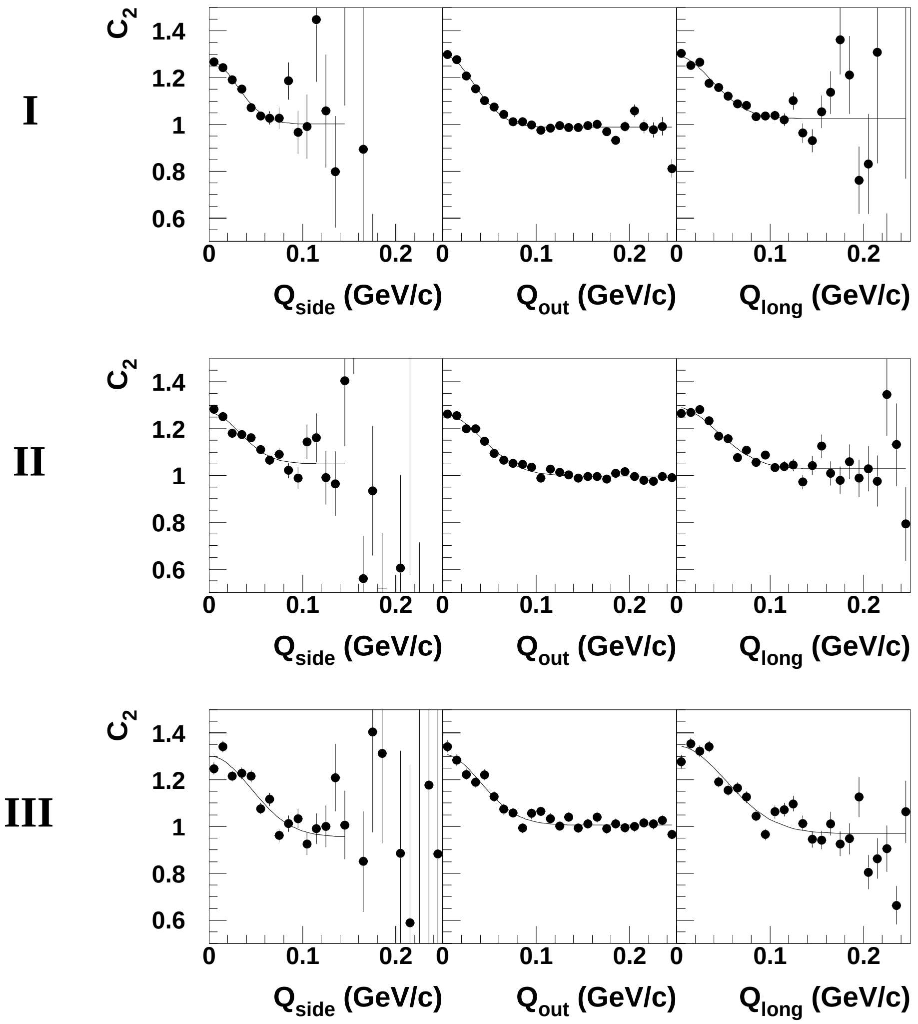

Figure 7.12: The correlation functions of $\pi^+\pi^+$ pairs in the standard side-out-long parameterization. From left to right, the correlation functions as a function of Q_{side}, Q_{out} and Q_{long} are shown. From top to bottom, C_2 functions at each K_T, classified in Table 7.1 are arranged. The solid curves in each panel correspond to the fitting results with Eq. 7.12.

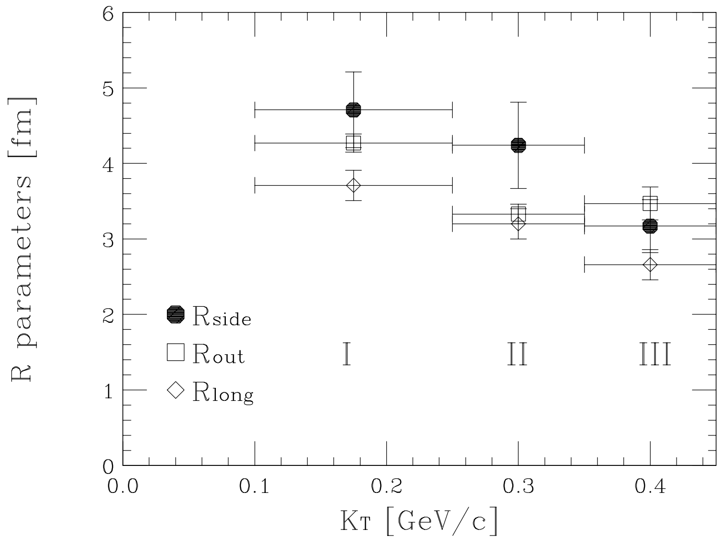

Figure 7.13: The average transverse momentum dependence of R_{side} (solid circle), R_{out} (open square) and R_{long} (open diamond) parameters in the standard side-out-long parameterization. The error bars indicate the statistical errors only.

7.7 Systematic Errors

Systematic error on the extracted HBT radii are itemized as follows.

1. **Coulomb correction**

   We used the standard Gamov factor for the Coulomb correction in the analysis. The Gamov factor is "point-like", in that it describes the emission of an isolated pair of charged particles from a small and otherwise neutral spatial region (r < 1fm). Because of the finite size of realistic sources [61] and the multi-particle Coulomb screening which occurs when a large number of charged pions are simultaneously emitted, the Gamov coulomb corrections is expected to cause systematic errors in the case of Au+Au collisions at AGS energies. The more realistic method for Coulomb correction has been developed by Pratt [37], which includes the Coulomb and the strong interaction corrections in the finite source size. Another realistic way of Coulomb correction is the extraction of the factor from measurements of correlation function of unlike-sign pairs as shown in Section 7.1 and 7.5. By the comparison between the extracted R_T parameters with standard Gamov correction and that with modified Gamov correction, it is estimated 2.5 % in K_T range I and II, and 1.0 % in K_T range III.

2. **Contamination in particle identification**

   In the analysis, the correlation functions are extracted identified π^+. The contamination from the other particles is estimated less than 1%, the error due to the contamination is expected to be negligible.

7.8 Summary of the Results for Two Particle Correlations

For two-particle correlation analysis, 2.5 millions of $\pi^+\pi^+$ pairs near mid-rapidity at 11 A GeV beam energy are used to extract correlation functions. In the frame of Yano-Koonin Podgoretskii (YKP) parameterization, it is found that the extracted source size parameter in the transverse direction, R_T, decrease from 5.21 ± 0.17 fm to 3.73 ± 0.26 fm with increasing averaged transverse pair momentum K_T from 0.1 GeV/c to 0.45 GeV/c. This gradual decease of R_T parameters with increasing of K_T is consistent with the picture with a expanding source.

As a consistency check, the correlation functions in the standard side-out-long parameterization are studied using the same data set and the same cut criteria, which is used in the HBT analysis in YKP parameterization. In that frame, it is also observed that the gradual decrease of all source size parameters with increase the average transverse momentum of pair, and it is consistent with the results obtained in the YKP parameterization.

Chapter 8

Discussions

In this Chapter, using the experimental results of single particle spectra in Chapter 6 and two-particle correlation in Chapter 7, we discuss the transverse velocity β_t and the freeze-out temperature T of the system created in Au+Au collisions at AGS energies within the framework of the expanding source model. Then the extracted β_t and T are compared with the results in Pb+Pb collisions at SPS, and we discuss validity of the picture of QGP formation in Pb+Pb central collisions at SPS from the viewpoint of β_t and T.

8.1 Overview

As shown in Chapter 6, we have observed the different mean transverse mass and the change of shapes in m_t spectra for different particle species in Au+Au collisions at AGS energies. In Chapter 7, the gradual decrease of R_T parameters with increasing averaged transverse momentum K_T of pair has been observed in $\pi^+\pi^+$ correlation function measurements at the energy of 11 A GeV central Au+Au collisions. As mentioned in Chapter 2, above features of both single particle and HBT's can be qualitatively explained by a expanding source picture.

On the other hand, in Pb+Pb central collisions at CERN-SPS energy, the same tendency has been reported by several experiments [65, 66, 67]. The transverse expansion velocity β_t and the freeze-out temperature T have been extracted by NA49 collaboration from the simultaneous analysis of single particle spectra and two-particle correlations using the framework of the finite expanding source scenario. Furthermore, as we introduced in Chapter 1, interesting experimental results which indicate the QGP formation have been reported in Pb+Pb at SPS energy in leptonic probes. Thus the comparison of β_t and T at AGS energies with that of at SPS should provide an important input to investigate the QGP formation.

In this chapter, the transverse velocity and the freeze-out temperature are extracted by fitting the data in Au+Au central collisions at AGS energies with the expanding source model. After the brief description of the finite expanding source model in Section 8.2, fitting results of the measured data in Au+Au central collisions with the model are shown in Section 8.3. Finally, the comparison with other beam energies are made, and the validity of picture of QGP formation at SPS energy are examined qualitatively in Section 8.4.

8.2 Expanding Source Model

We start from review of the general approach and definition of the notation with regard to the expanding source model [39, 40]. First, we mention the emission function, which defines the single particle momentum spectrum and two-particle correlation function. Next, the expanding source model is introduced in various sources, the static Gaussian source, the boost-invariant source and the finite expanding source. At the last part of this section, the functions of m_t spectrum and R_T including β_t and T are given.

8.2.1 Emission function

The emission function $S(x,p)$ describes the probability that a particle with on-shell momentum p ($p^2 = m^2$) is emitted from the space-time point x. $S(x,p)$ determines the single particle momentum spectrum $P_1(\mathbf{p})$ as well as the two-particle correlation function $C_2(\mathbf{K},\mathbf{q})$ as,

$$\begin{aligned} P_1(\mathbf{p}) &= E\frac{dN}{d^3p} = \int d^4xS(x,p), && (8.1)\\ C_2(\mathbf{K},\mathbf{q}) &= \frac{<N>^2}{<N(N-1)>}\frac{P_2(\mathbf{p_1},\mathbf{p_2}))}{P_1(\mathbf{p_1}),P_1(\mathbf{p_2})} && (8.2)\\ &= 1+\frac{|\int d^4xS(x,K)e^{iq\cdot x}|^2}{\int d^4xS(x,p_1)\int d^4xS(x,p_1)}, && (8.3)\end{aligned}$$

where $\mathbf{K} = (1/2)(\mathbf{p_1}+\mathbf{p_2}) = (\mathbf{K}_T, K_L)$ is the average momentum of the two particles, $\mathbf{q} = \mathbf{p_1} - \mathbf{p_2}$ is their relative momentum and $P_1(\mathbf{p})$, $P_2(\mathbf{p_1},\mathbf{p_2})$ are 1- and 2-particle distributions. In the numerator of Eq. 8.3, we have introduced off-shell momentum four-vectors K and q for the total and relative momentum of the particles in the pair by defining $K_0 = (1/2)(E_1 + E_2)$ and $q_0 = E_1 - E_2$ where $E_i = \sqrt{m^2 + \mathbf{p_i}^2}$. By putting K on shell, $K_0 \simeq E_K = \sqrt{m^2 + \mathbf{K}^2}$, and setting $p_1 = p_2 = K$ in the 1-particle distribution in the denominator, the correlation function is rewritten as,

$$C_2(\mathbf{K}, \mathbf{q}) \simeq 1 + \frac{|\int d^4x S(x,K) e^{iq\cdot x}|^2}{|\int d^4x S(x,K)|^2}. \tag{8.4}$$

Therefore, if the emission function $S(x,K)$ is known, the single particle spectrum and two particle correlation can be calculated by Eq. 8.1 and Eq. 8.4, respectively.

8.2.2 Static Gaussian source

First, we consider a static emission function which is defined by a space-time Gaussian at a position (x, y, z) and time t in its center of mass frame as;

$$S(x,K) = h(K) \exp\Big(-\frac{x^2+y^2}{2R^2} - \frac{z^2}{2L^2} - \frac{(t-t_0)^2}{2(\Delta t)^2}\Big), \tag{8.5}$$

where the z axis is along the beam (longitudinal) direction, L and R are the size of the source in the beam direction and in the perpendicular (transverse) direction with respect to the beam axis, respectively. The average and the root mean square of freeze-out time of the source is shown as t_0 and Δt, respectively. We define the rapidity corresponding to K as;

$$Y = \frac{1}{2} \ln\Big(\frac{K_0 + K_z}{K_0 - K_z}\Big). \tag{8.6}$$

The transverse mass M_T and the energy K_0 corresponding to K are defined by;

$$M_T = \sqrt{m_0^2 + K_T^2}, \tag{8.7}$$

$$K_0 = M_T \cosh(Y), \tag{8.8}$$

where m_0 is the rest mass of the particle. Assuming a thermalized system, the factor $h(K)$ in Eq. 8.5 can be expressed by the Lorentz invariant Boltzmann factor, $K_0 \exp(-K_0/T)$, where T is the temperature at freeze-out. In this case, the source function $S(x,K)$ can be rewritten as;

$$S(x,K) = N M_T \cosh(Y) \exp\Big(-\frac{K_0}{T} - \frac{x^2+y^2}{2R^2} - \frac{z^2}{2L^2} - \frac{(t-t_0)^2}{2(\Delta t)^2}\Big), \tag{8.9}$$

where N is a normalization factor. In the Yano-Koonin-Podgoretskii parameterization, abbreviation as YKP hereafter, fitting parameters are given as;

$$R_T = R, \tag{8.10}$$

$$R_L = L, \tag{8.11}$$

$$R_0 = \Delta t. \tag{8.12}$$

8.2.3 Boost-invariant source

Next we consider a longitudinally expanding source which invariant under a Lorentz boost along the beam axis. The emission function can be expressed as,

$$S(x,K) = NM_T \cosh(Y-\eta) \exp\Big(-\frac{K\cdot u}{T} - \frac{x^2+y^2}{2R^2} - \frac{(\tau-\tau_0)^2}{2(\Delta\tau)^2}\Big), \tag{8.13}$$

where $\tau = \sqrt{t^2-z^2}$ is the longitudinal proper time, τ_0 and $\Delta\tau$ are the average and the root mean square of the freeze-out proper time of the source, respectively. The longitudinal expansion of the source is described by the flow four-velocity $u^\mu(x)$ relative to some fixed frame as,

$$u_\mu(x) = (\cosh\eta, 0, 0, \sinh\eta). \tag{8.14}$$

In the expression, we assume longitudinal boost invariance by setting $v_L = z/t$, i.e., identifying the longitudinal flow rapidity $\eta_{\text{flow}} = (1/2)\ln[(1+v_L)/(1-v_L)]$ with space-time rapidity $\eta = (1/2)\ln[(t+z)/(t-z)]$.

The YKP fitting procedure gives:

$$R_T = R \tag{8.15}$$

$$R_L = \tau_0\sqrt{\frac{T}{M_T}}, \tag{8.16}$$

$$R_0 = \Delta\tau. \tag{8.17}$$

8.2.4 Finite expanding source

Finally, we consider the finite expanding source model as an extension of the above models. For the assumption used in the model, it can be summarized as below,

1. Local thermal equilibration of the system.

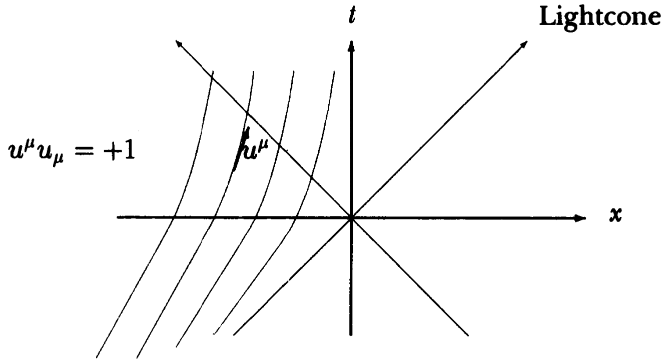

Figure 8.1: Flow velocity profile of a medium, u^μ, which is a time-like unit vector parallel to the world-line of particle. Reproduced from [68].

2. Transverse and longitudinal motion can be decoupled.
3. Longitudinal boost invariant.
4. Azimuthally symmetric Gaussian source.
5. Sudden freeze-out at a temperature T and a time τ_0 for all particle species.
6. No resonance contributions.

Considering these assumptions, the emission function in the case of the finite expanding source can be expressed as,

$$S(x,K) = NM_T \cosh(Y-\eta)\exp\Big(-\frac{K\cdot u}{T} - \frac{x^2+y^2}{2R^2} - \frac{(\tau-\tau_0)^2}{2(\Delta\tau)^2} - \frac{\eta^2}{2(\Delta\eta)^2}\Big). \quad (8.18)$$

The cutoff in space-time rapidity η is introduced due to the terms in $\cosh(Y-\eta)$ in the above expression. In the approximation that $M_T/T \gg 1$, the YKP fitting procedure gives as,

$$\begin{aligned} R_T &= R, && (8.19)\\ R_L &= \tau_0\Big(\frac{M_T}{T}\cosh(Y-\overline{\eta}) - \frac{1}{\cosh^2(Y-\overline{\eta})} + \frac{1}{(\Delta\eta)^2}\Big)^{\frac{1}{2}}, && (8.20)\\ R_0 &= \Delta\tau, && (8.21)\end{aligned}$$

where the parameter v is the velocity difference between the measurement frame and the local rest frame of the source. The parameter $\overline{\eta}$ is solution of :

$$\tanh(Y-\overline{\eta}) - \frac{M_T}{T}\sinh(Y-\overline{\eta}) + \frac{\overline{\eta}}{(\Delta\eta)^2} = 0. \quad (8.22)$$

In the case of a boost-invariant source, the above equation is simply $\overline{\eta} = Y$. In the limit $\Delta\eta \to \infty$, the finite expanding source reduces to the boost-invariant source. Next, We consider now a source function with a transverse velocity β_t in the flow four-velocity as,

$$u_\mu(x) = (\cosh\eta\cosh\beta_t, \sinh\beta_t\cos\phi, \sinh\beta_t\sin\phi, \sinh\eta\cosh\beta_t), \tag{8.23}$$

The transverse flow β_t is taken azimuthally (ϕ) symmetric. It is parameterized as the uniform expansion in r direction as:

$$\beta_t(r) = \beta_t\Big(\frac{r}{R}\Big), \tag{8.24}$$

where β_t is a constant and $r = \sqrt{x^2 + y^2}$. In the YKP fitting procedure, the measured R_T is given as,

$$\begin{aligned} R_T &\simeq \Big(1 + \frac{M_T}{T}\beta_f^2\Big)^{\frac{1}{2}} \\ &= \Big(1 + \frac{\sqrt{K_T^2 + m_\pi^2}}{T}\beta_f^2\Big)^{\frac{1}{2}} \end{aligned} \tag{8.25}$$

As seen in Eq. 8.25, R_T decreases with increasing the expansion velocity and with increasing average transverse momentum K_T of pair. We use the function in Eq. 8.25 to fit the measured data of K_T dependence of R_T parameter. It should be noted that only if β_t is incorporated in the model, the K_T dependence on R_T appear.

8.2.5 m_t spectrum in finite expanding source

In this section, we will discuss the transverse mass spectrum in the framework of the finite expanding source model given by Chapman et al. [69]. The single particle distribution P_1 in the case can be approximated by the expression as a function of the transverse mass m_t and the rapidity y as,

$$\begin{aligned} P_1(m_t, y) &\propto m_t R_*^2 \Delta\eta_* \left[1 + \frac{R_*^2}{2R_G^2}(\Delta\eta_*)^2 - \frac{m_t}{8T}(\Delta\eta_*)^4\right] \\ &\quad \exp\left[-\frac{m_t}{T} + \frac{\beta_t^2(m_t^2 - m_0^2}{2T(T + m_t\beta_t^2} - \frac{0.5y^2}{(\Delta\eta)^2 + T/m_t}\right], \end{aligned} \tag{8.26}$$

where

$$\frac{1}{R_*^2} = \frac{1}{R_G^2}\left(1 + \beta_t^2\frac{m_t}{T}\right), \tag{8.27}$$

$$\frac{1}{\Delta\eta_*^2} = \frac{1}{(\Delta\eta)^2} + \frac{m_t}{T}. \tag{8.28}$$

In Eq. 8.28, $\Delta\eta$ is the width of the space-time rapidity $\eta = (1/2)\ln(t+z)/(t-z)$. This is related to the width of the rapidity distribution Δy as,

$$(\Delta y)^2 = (\Delta\eta)^2 + \frac{T}{m_t}. \tag{8.29}$$

In Fig. 8.2, it is demonstrated the change of the shapes and slopes of m_t spectra for deuterons, protons, kaons and pions at the fixed temperature $T = 150$ MeV and various transverse velocity from $\beta_t = 0.0$ to 0.6 in 0.2 step. It is clearly shown that the shoulder arm shape arises in deuteron and proton spectra by increasing β_t, in contrast, in pions spectra, β_t changes the shapes from exponential scaling to concave shape particularly at low m_t region. Spectra shapes of kaons are almost the same, but increasing its inverse slope parameters with increasing β_t. These features are clearly seen in 4 and 11 A GeV Au+Au collisions as discussed in Chapter 6.

8.3 Fitting Results by the Finite Expanding Source Model

8.3.1 Fitting results of single particle spectra

Using Eq. 8.26 as the fitting function to the data, β_t and T are extracted in Au+Au central collisions at 4 and 11 A GeV, near mid-rapidity region.

Fig. 8.3 and Fig. 8.4 show the results of the fitting by the finite expanding source model for deuterons, protons, kaons and pions in Au+Au collisions at 4 and 11 A GeV beam energy, respectively. For the pion spectra at both 4 and 11 A GeV, average of π^+ and π^- spectra is taken for the fitting, and low m_t range is excluded for the fitting to avoid the contribution from resonance decay.

As shown in the Fig. 8.3 and Fig. 8.4, all the spectra at 4 and 11 A GeV are well reproduced by the model. Fig. 8.5 and Fig. 8.6 show allowed regions of freeze-out temperature T vs. transverse velocity β_t, derived from the fit of Eq. 8.26 to single particle spectra of deuterons, protons, kaons and pions in Au+Au collisions near mid-rapidity at 4 and 11 A GeV, respectively. Contours in each figure are drown at two standard deviations from the best fit values. The overlapped region of contours in the figure can be consider to the allowed region in β_t and T of the system. For the results at 4 A GeV, the spectra have the overlapped region in $T = 80 \sim 90$ MeV and $\beta_t = 0.6 \sim 0.7$, except for the deuteron. For the results at 11 A GeV, there are the

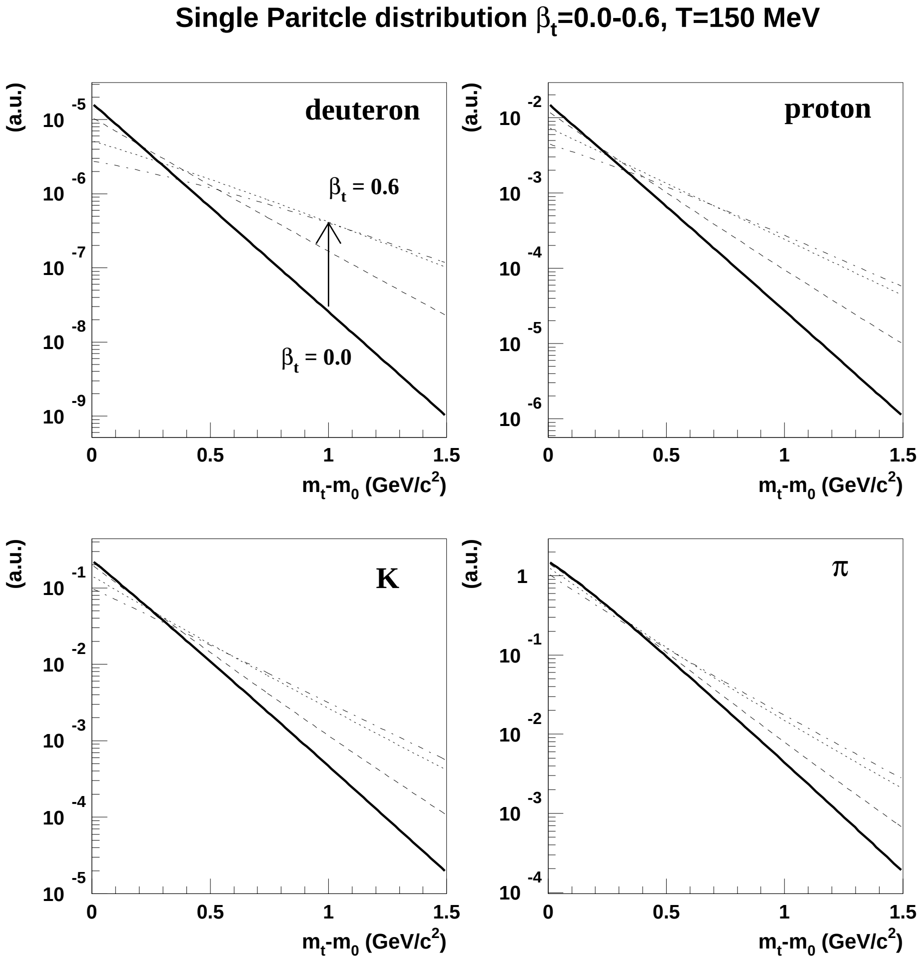

Figure 8.2: m_t spectra for deuterons, protons, kaons and pions calculated by the finite expanding source model (Eq. 8.26) at $T = 150$MeV and various transverse velocities β_t.

allowed region $T = 90 \sim 100$ MeV and $\beta_t = 0.65 \sim 0.85$. It is found the extracted value of both β_t and T are larger at 11 A GeV beam energy than that at 4 A GeV in central Au+Au collisions. The stronger transverse expansion velocity with higher temperature at 11 A GeV are created than that of 4 A GeV beam energy.

As discussed in Section 1.2.3, overlapped region is rather broad, so that the unique set of parameter (β_t, T) can not be determined by the single particle spectra alone, because of the strong anti-correlation between β_t and T. In order to resolve this uncertainty, K_T dependence of R_T parameter from two-particle correlations provide the another boundary in β_t vs. T plane, which is expected in perpendicular to the contours from single particle spectra.

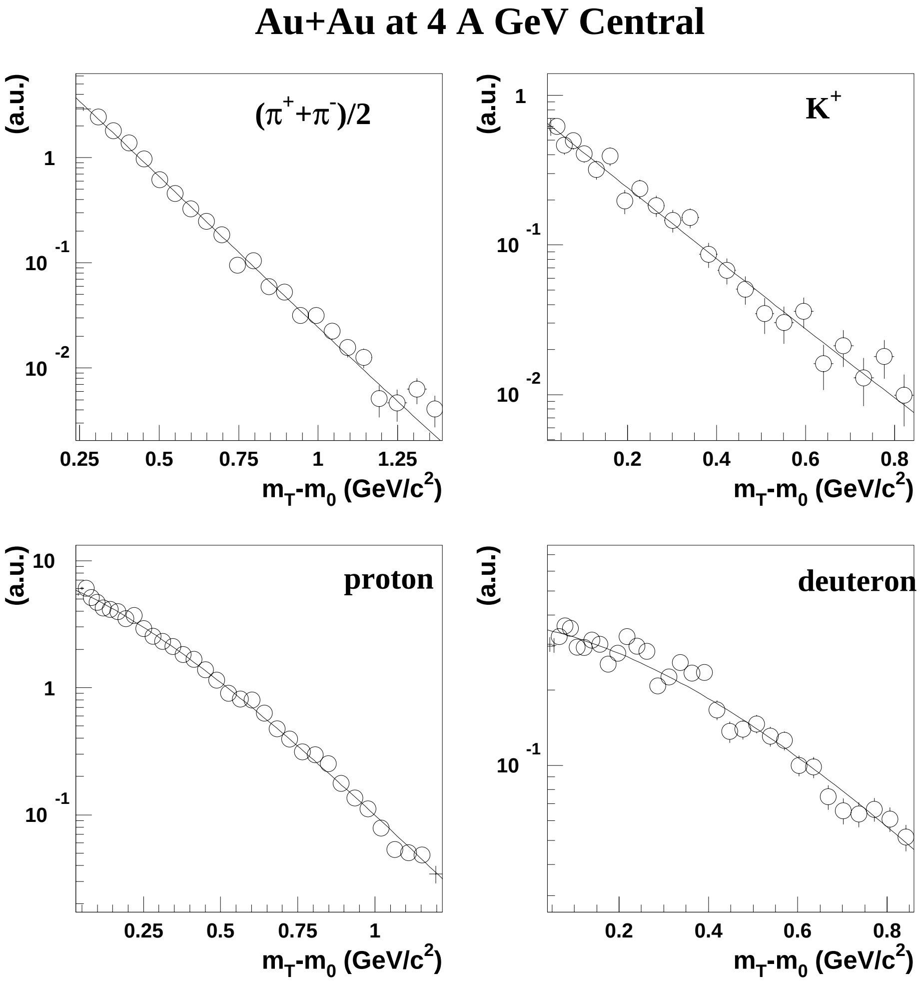

Figure 8.3: Fitting results by finite expansion source model for deuterons, protons, kaons and pions in Au+Au collisions at 4 A GeV beam energy. The centrality of data is 10% most central. For pions, cross-section are deduced by taking average $(\pi^+ + \pi^-)/2$.

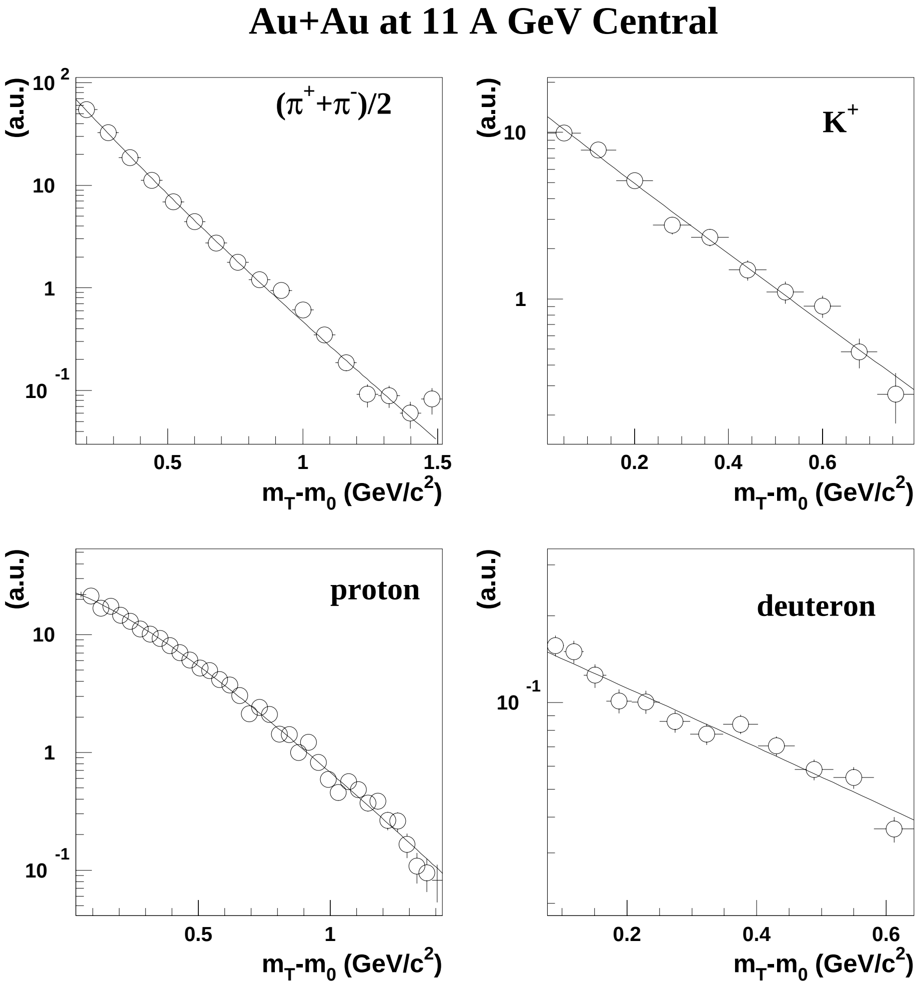

Figure 8.4: Fitting results by finite expansion source model for deuterons, protons, kaons and pions in Au+Au collisions at 11 A GeV beam energy. The centrality of data is 10% most central. For pions, cross-section are deduced by taking average $(\pi^+ + \pi^-)/2$.

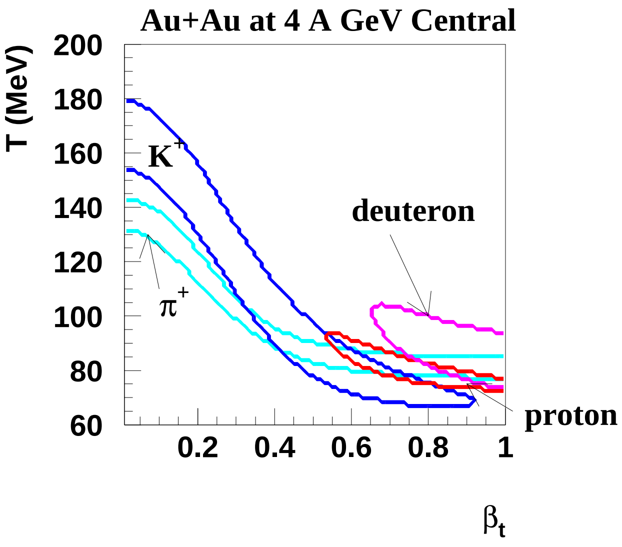

Figure 8.5: Allowed regions of freeze-out temperature T vs. transverse velocity β_t, derived from the fit of Eq. 8.26 to single particle spectra of deuterons, protons, kaons and pions in central Au+Au collisions at 4 A GeV, near mid-rapidity. Contours are shown for two standard deviations from the best fit.

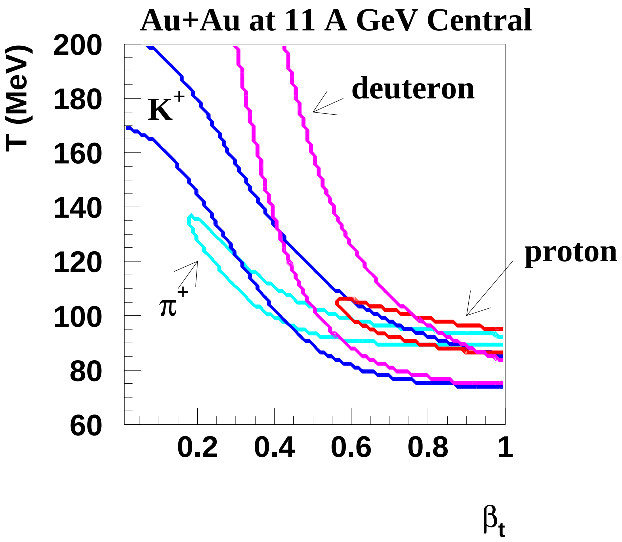

Figure 8.6: Allowed regions of freeze-out temperature T vs. transverse velocity β_t, derived from the fit of Eq. 8.26 to single particle spectra of deuterons, protons, kaons and pions in central Au+Au collisions at 11 A GeV, near mid-rapidity. Contours are shown for two standard deviations from the best fit.

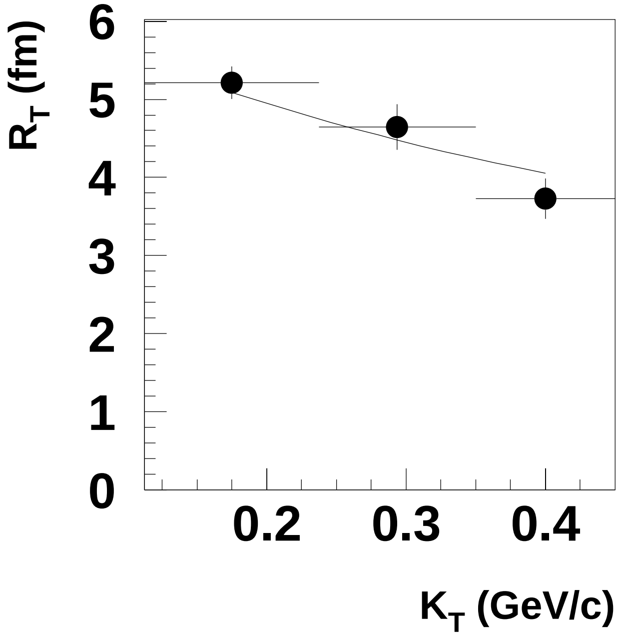

Figure 8.7: Fitting result of K_T dependence of R_T parameter in YKP parameterization by the finite expanding source model in Eq. 8.25 (solid line). The solid circles correspond to the experimental data obtained in Section 7.4.

8.3.2 Fitting results of two-particle correlations

Next, we consider K_T dependence of R_T by the same expanding source model, which is used in the fitting to the single particle spectra. The fitting function is the expression in Eq. 8.25, and fitting parameter is the ratio of β_t^2/T. Fig. 8.7 shows the fitting result, which is included systematic error from Coulomb corrections in the error bars. The extracted parameter by the fitting is $\beta_t^2/T = 8.00 \pm 0.70[\mathrm{GeV}^{-1}]$. From the ratio, the allowed region of $T - \beta_t$ can be determined. Fig. 8.8 shows the the allowed region of β_t vs. T, derived from the fit of Eq. 8.25 to the data of K_T dependence of R_T parameter in YKP parameterization. Contours are drown at two standard deviations from the best fit values.

The contours obtained from the analysis of two-particle correlation provide the further restriction to determine β_t and T uniquely, because of the different domain in $\beta_t - T$ plane between single particle spectra and HBT.

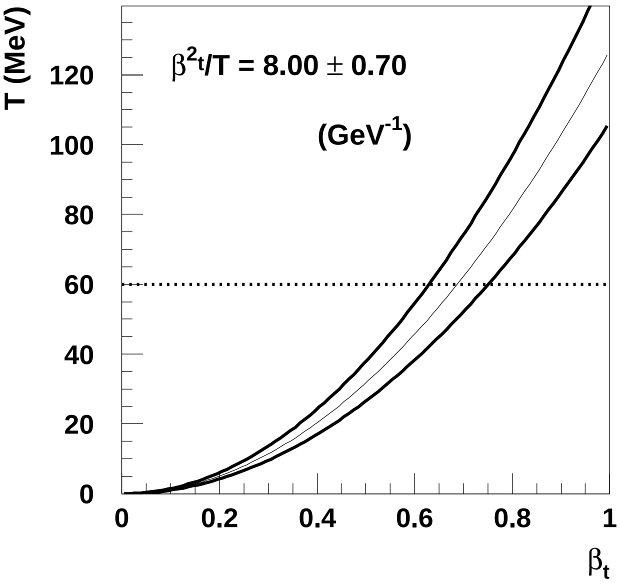

Figure 8.8: The allowed region of freeze-out temperature T vs. transverse velocity β_t, derived from the fit of Eq. 8.25 to two-particle correlations of $\pi^+\pi^+$ pairs in central Au+Au collisions at 11 A GeV, near mid-rapidity. Contours are drown at two standard deviations from the best fit values.

8.3.3 Simultaneous analysis of single particle spectra and HBT

In single particle analysis, strong anti-correlation between β_t and T is seen, while in HBT analysis, β_t and T is found to be proportional. Therefore, β_t and T cannot be determined uniquely neither from the analysis of single particle nor HBT alone. But by combining these two regions, it can be resolved this essential ambiguity and determine β_t and T uniquely.

Fig. 8.9 shows the overlay of the fitting results (Fig. 8.8) obtained in HBT on that from single particle spectra contours (Fig. 8.6) in Au+Au central collisions near mid-rapidity. From Fig. 8.9, we can obtain the overlap region between the contours from single particle spectra and that from HBT analysis, at $T = 95 \pm 5$ MeV and $\beta_t = 0.80 \pm 0.05$, which characterize the system created in Au+Au central collisions at the energy of 11 A GeV.

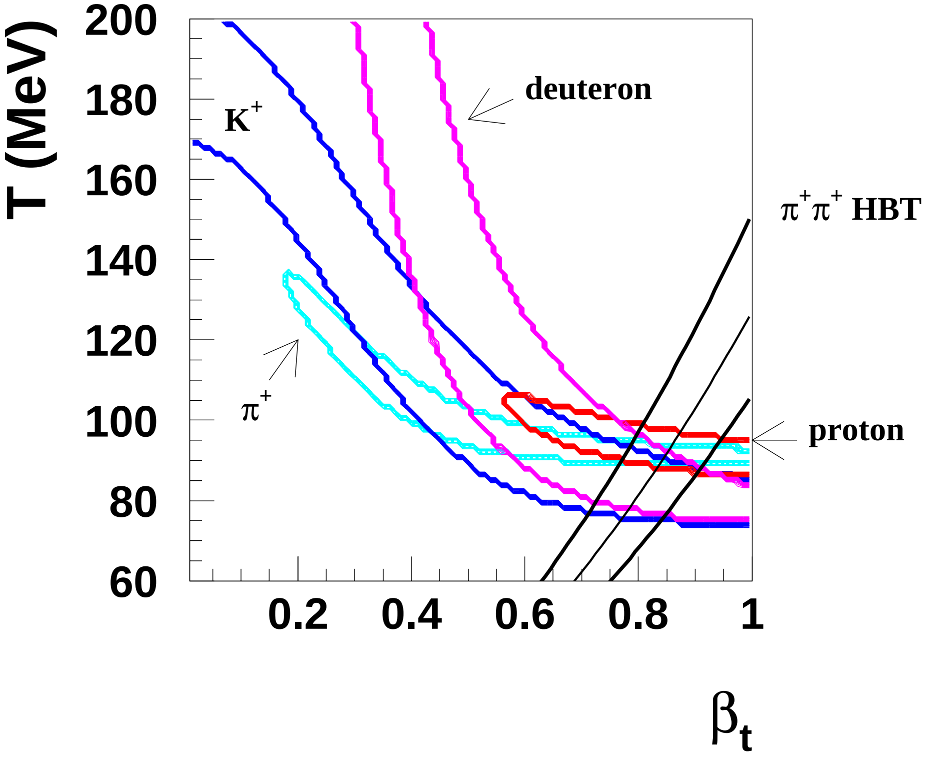

Figure 8.9: Allowed regions of T vs β_t for central Au+Au collisions near mid-rapidity, derived from the fit of Eq. 8.26 to transverse mass spectra of deuterons, protons, kaons and pions, and from the fit of Eq. 8.25 to to two-particle correlations of $\pi^+\pi^+$ pairs in central Au+Au collisions at 11 A GeV, near mid-rapidity. Contours are shown for two standard deviations from the best fit for transverse spectra and two-particle correlations.

8.4 Excitation Function of $< \beta_t >$ and T

As introduced in Chapter 1, it is predicted that the QGP formation causes the softening of the equation of state because the internal pressure relative to the internal energy drops at a critical temperature T_c [11, 62, 63, 64]. Thus the excitation function of transverse expansion velocity is considered as an important clue for the detection of the QGP formation; a sudden drop of β_t may indicate the QGP formation. In this section, we discuss the excitation functions of transverse velocity β_t and the freeze-out temperate T from the viewpoint of the QGP formation.

8.4.1 Excitation functions from SIS to AGS and SPS

The mean transverse expansion velocity $< \beta_t >$ and freeze-out temperature T have been studied in various collision system in wide range of the beam energies from GSI-SIS energy regime, 100 A MeV to CERN-SPS energy regime, 200 A GeV by the fitting the single particle spectra with the radial flow model [27]. Fig. 8.11 and Fig. 8.12 show the excitation function of $< \beta_t >$ and T from various experiments, respectively. The extracted values from the present analysis at AGS and from NA49 at SPS are also plotted in the figures, extracted by the simultaneous analysis of single particle spectra and HBT with the expanding source model. It should be noted that mean transverse velocity in this analysis and that of NA49 collaboration are deduced by taking average of the velocity profile of the expanding source model, $\beta_t(r) = \beta_t\left(\frac{r}{R}\right)$ as,

$$< \beta_t >= \frac{\int_0^R dr\, \beta_t(r)}{\int_0^R dr\, r} = \frac{2}{3}\beta_t, \tag{8.30}$$

where R is the radius of the system and r is the distance from the center of the system. As seen in Fig. 8.11, the values of $< \beta_t >$ rise monotonically with E_{beam} up to the AGS energy region ($\sim$ 10 A GeV), but it seems to saturate at the SPS energy. From Fig. 8.12, on the other hand, freeze-out temperatures rise continuously with increasing of E_{beam}.

8.4.2 Comparison of β_t and T between AGS and SPS energies

At CERN-SPS energy (158 A GeV) in Pb+Pb collisions, the similar simultaneous analysis of single particle spectra with HBT have been carried out. The extracted values in Pb+Pb central collisions by NA49 experiment is $T = 120 \pm 12$ MeV and

$\beta_t = 0.55 \pm 0.12$ [17]. In comparison of these at AGS and at SPS, the stronger transverse velocity β_t is obtained in central Au+Au collisions at 11 A GeV than that of SPS, while the freeze-out temperature is larger at SPS than at AGS energy at the confidence level of 95 %. How can we interpret the tendencies of β_t and T?

First, we consider the freeze-out temperature. The extracted T from the simultaneous analysis of single particle spectra with HBT is not the value for the simple parameterization like a inverse slope parameter, but is the more reliable value as the temperature of the system at freeze-out stage, because of 1) less ambiguity between β_t and T (as shown in Section 8.3.1) and 2) consistency; the same model are used for fitting with both data.

According to the lattice QCD calculations, the phase transition from hadronic phase to QGP phase occurs at the critical temperature $T_c = 140 \sim 200$ MeV in baryon-free matter [1]. We cannot compare directly the results of the lattice QCD with extracted freeze-out temperature. But as regarding the reduction of extracted β_t at SPS energy and extracted T is not so far from T_c, it is not so hard to assume that the temperature of the system created in Pb+Pb at SPS is above T_c, then the system expands and cools down to the freeze-out temperature $T = 120$ MeV, and finally, the particles are emitted from the reaction zone freely. On the other hand, in Au+Au central collisions at 11 A GeV, extracted $T = 95 \pm 5$ MeV seems far from the critical temperature. Therefore, it is likely that beam energy corresponding to the QGP phase transition is in between AGS and SPS.

Several interesting features of the observation have been reported in Pb+Pb collisions at SPS, among which are the suppression of J/Ψ production [7] by NA50 experiment and the enhancement of low-mass dilepton [9] by CERES experiment. NA50 collaboration have claimed in the paper [7] that "an observed anomalous J/Ψ suppression can be considered as a strong indication of the production of a QGP phase in central Pb+Pb collisions". Ordinal hadronic scenario has been shown to fail in qualitative explanation of J/Ψ data.

The observed effect of the smaller β_t at SPS compared to that at AGS energy seems to be explained by the softening of the equation of state (EoS) due to a QGP formation at SPS energy in Pb+Pb collisions. Fig. 8.10 shows the equation of state, derived by simple parameterization of the results of lattice QCD calculations [11]. The ideal hadron gas (dashed lines), a first order QGP phase transition (solid lines) and a smooth QGP transition (dotted lines) are shown in the figure. Each panel in Fig. 8.10

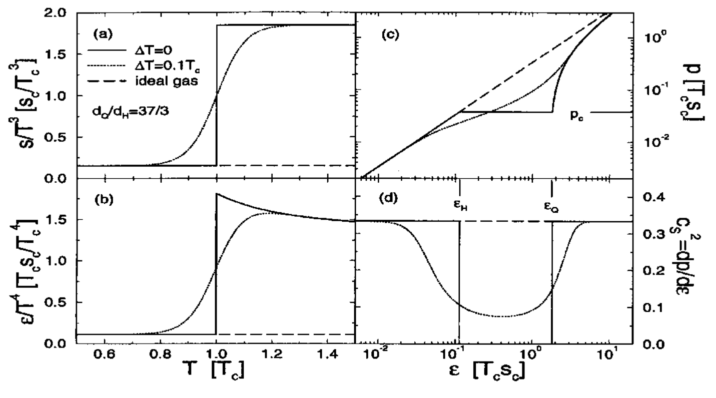

Figure 8.10: The equation of state: (a) entropy density divided by T^3, (b) energy density divided by T^4 as function of temperature, (c) pressure, and (d) the squared velocity of sound as functions of energy density. Solid lines are for a first order transition (ΔT =0), dotted lines for a smooth transition with $\Delta T = 0.1T_c$, and dashed lines are for an ideal gas with d_H degrees of freedom. The ratio of degrees of freedom is $d_Q/d_H = 37/3$ [11].

is; (a) the entropy density, (b) the energy density as functions of temperature, and (c) the pressure and (d) the squared velocity of sound $c_S^2 \equiv \mathrm{d}p/\mathrm{d}\epsilon$ as functions of energy density. ΔT is the width of temperature at T_c. As can be seen in (c) in Fig. 8.10, for $\Delta T = 0$ the pressure stays constant in the mixed phase $\epsilon_H \leq \epsilon \leq \epsilon_Q$, where ϵ_H is the energy density at the phase boundary between mixed phase and hadronic phase, and ϵ_Q is that between mixed phase and QGP. As hydrodynamical expansion is driven by pressure gradients, the square of the velocity of sound $c_S^2 = \mathrm{d}p/\mathrm{d}\epsilon$ is the most relevant measure of the system's tendency to expand as shown in Fig 8.10 (d). For $\Delta T = 0$, the velocity of sound vanishes in the mixed phase, i.e., mixed phase matter does not exhibit expansion at all. For finite ΔT, pressure gradients are finite, but still smaller than for an ideal hadronic gas, and therefore the expansion velocity is also reduced (Fig. 8.10 (d)).

The reduction of c_S^2 in the transition region is commonly referred to as "*softening*" of the EoS. For matter passing through that region during the expansion phase, the velocity of expansion will temporarily slow down. Based on the above picture, the observed reduction of β_t at SPS may be attributed to these softening of EoS by the formation of QGP.

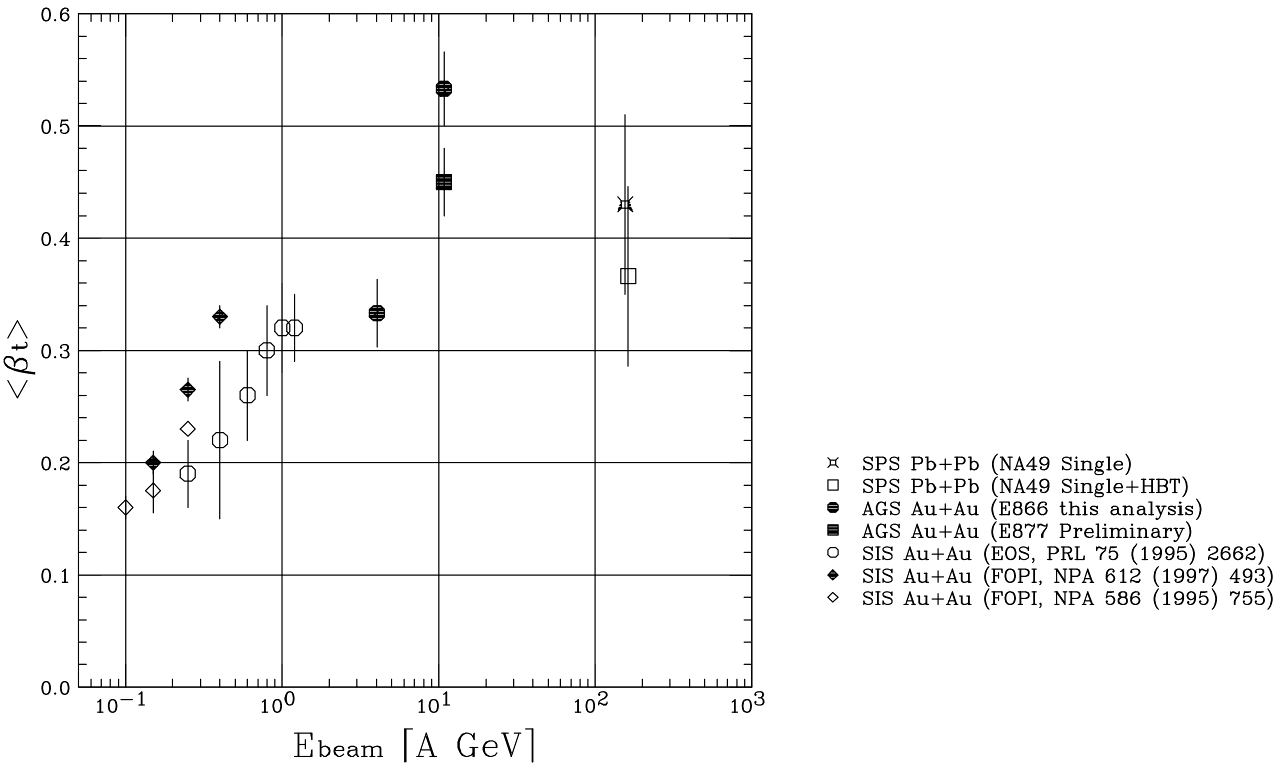

Figure 8.11: Excitation function of mean transverse velocity $< \beta_t >$ extracted by the fitting single particle spectra with the expanding source model [27]. Extracted values in this analysis and NA49 collaboration by the simultaneous analysis of single particle spectra and HBT are also shown in terms of $< \beta_t >$. See also [70] for the compilation of $< \beta_t >$ extracted from single particle spectra alone in various experiments.

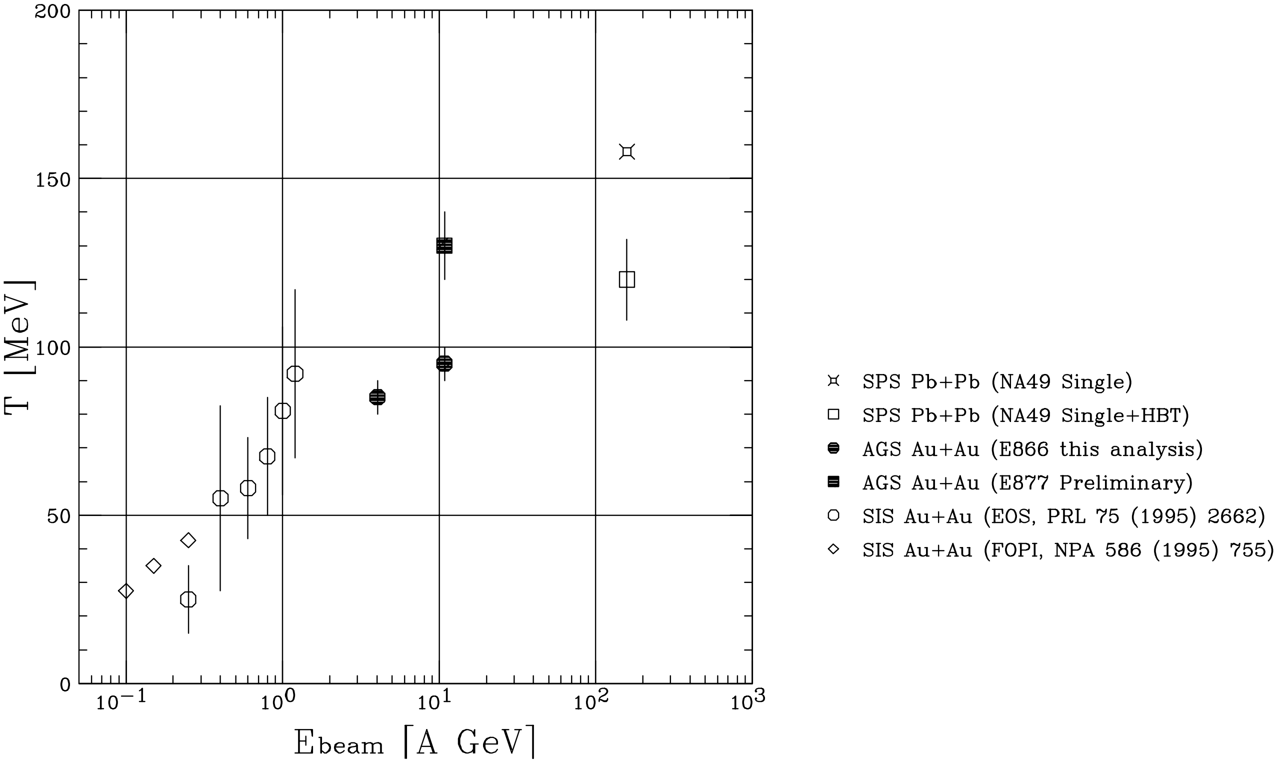

Figure 8.12: Excitation function of freeze-out temperature T extracted by the fitting single particle spectra with the expanding source model [27]. Extracted values in this analysis and NA49 collaboration by the simultaneous analysis of single particle spectra and HBT are also shown. See also [70] for the compilation of T extracted from single particle spectra alone in various experiments.

Chapter 9

Conclusions

We have presented the results of single particle spectra in Au+Au collisions at the energy of 4 and 11 A GeV, and the results of high statistic $\pi^+\pi^+$ two-particle correlations in Yano-Koonin Podgoretskii (YKP) parameterization in Au+Au collisions at 11 A GeV, measured by the E866 experiment using the Alternating Gradient Synchrotron (AGS) at Brookhaven National Laboratory (BNL).

For the systematic studies of hadron productions in relativistic heavy-ion collisions near mid-rapidity region, we have constructed a rotatable magnetic spectrometer, called the Forward Spectrometer. It is designed for the good particle identification capability under the condition of high particle density and for the wide range of kinematic coverage in Au+Au collisions at AGS. Using the data taken by the Forward Spectrometer, single particle spectra and HBT correlations are analyzed.

For single particle analysis, we have measured transverse mass spectra for $\pi^\pm$, K^+, protons and deuterons at 4 and 11 A GeV as a function of centrality. For the transverse mass spectra, we have observed the mass dependence of mean transverse mass $< m_t > -m_0$; for the particle with heavier mass, the larger $< m_t > -m_0$ is seen. In addition, the shapes of the m_t spectrum for protons have a shoulder-arm shape in central collisions at low m_t region. On the other hand, the pion spectra at 11 A GeV have a concave shape at low m_t region, which can be attributed, in part, to the effects of a transverse velocity field of a created system. Observed shoulder-arm shapes of protons and the mass dependence of mean transverse mass are consistent with an expanding source.

For the proton's dN/dy, the distributions have a maximum at mid-rapidity at both 4 and 11 A GeV beam energy in central events, which indicates a large baryon stopping in Au+Au collisions at AGS energies.

In $\pi^+\pi^+$ HBT correlation analysis in YKP parameterization, it is found that the extracted source size parameter in the transverse direction, R_t, decreases from 5.21 ± 0.17 fm to 3.73 ± 0.26 fm with increasing the transverse pair momentum K_T from 0.1 GeV/c to 0.45 GeV/c. This gradual decease of R_T with increasing K_T is also consistent with the expanding source.

As a consistency check, the correlation functions in the standard side-out-long parameterization are studied using the same data set and the same cut criteria, which is used in the HBT analysis in YKP parameterization. In that frame, it is also observed that the gradual decrease of all source size parameters with increase the average transverse momentum of pair, and it is consistent with the results obtained in the YKP parameterization.

Motivated by these observations that both single particle spectra and HBT correlations are qualitatively consistent with the picture of an expanding source, the simultaneous analysis of both data using the finite expanding source model is carried out for the first time at AGS energy. From this analysis, the freeze-out temperature T and the transverse expansion velocity β_t in Au+Au central collisions at 11 A GeV are extracted uniquely; $T = 95{\pm}5$ MeV and $<\beta_t>= 0.53{\pm}0.03$, which can be considered as more reliable values than those from the conventional analysis of single particle spectra alone. Compared with $T = 120 \pm 12$ MeV and $<\beta_t>= 0.37 \pm 0.08$, reported from the former analysis at CERN-SPS 158 A GeV Pb+Pb collisions, T is larger at SPS than at AGS, while $<\beta_t>$ is larger at AGS than at SPS at the confidence level of 95 %. The softening of equation of state (EoS) by the QGP formation is one of the qualitative interpretation for the observed small $<\beta_t>$ at SPS energy than that at AGS. Thus, the reduction of $<\beta_t>$ at SPS dose not contradict the picture of the QGP formation in Pb+Pb collisions at 158 A GeV, which is indicated by the recent observation of anomalous J/Ψ suppression and low-mass dilepton enhancement.

Appendix A

Kinematic Variables

Here, we introduce kinematic variables used in the thesis. It is useful to describe them with Lorentz invariant variables or variables which have simple Lorentz transformation properties, because we deal with relativistic particles and system .

We take a beam line to be z-axis of a frame. For a particle which has momentum $\mathbf{p} = (p_x, p_y, p_z)$ and mass m, we use a longitudinal momentum p_z, a transverse momentum $p_t \equiv \sqrt{p_x^2 + p_y^2}$, and total energy $E = \sqrt{\mathbf{p}^2 + m^2}$. Transverse mass m_t and rapidity y are defined as

$$m_t \equiv \sqrt{p_t^2 + m^2} \tag{A.1}$$

$$y \equiv \frac{1}{2}\ln\left(\frac{E + p_z}{E - p_z}\right). \tag{A.2}$$

The total energy and longitudinal momentum of a particle can be easily related to its transverse mass and rapidity as

$$E = m_t\cosh(y) \tag{A.3}$$

$$p_z = m_t\sinh(y). \tag{A.4}$$

Appendix B

The BNL-AGS E802/866 Collaboration List

BNL-UC Berkeley-UC Riverside-Columbia-INS(Tokyo)-Kyoto-LLNL-Maryland-MIT-Tokyo-Tsukuba-Yonsei

L.Ahle[h], Y.Akiba[e], K.Ashktorab[a], M.D.Baker[h], D.Beavis[a], H.C.Britt[g], J.Chang[c], C.Chasman[a], Z.Chen[a], C.-Y.Chi[d], Y.Y.Chu[a], T.Chujo[k], V.Cianciolo[g], B.A.Cole[d], H.J.Crawford[b], J.B.Cumming[a], R.Debbe[a], J.C.Dunlop[h], W.Eldredge[c], J.Engelage[b], S.-Y.Fung[c], J.Gaardhoje[i], E.Garcia[m], M.Gonin[a], S.Gushue[a], H.Hamagaki[e], A.Hansen[i], L.Hansen[i], R.S.Hayano[j], G.Heintzelman[h], S.Homma[e], E.Judd[b], H.Kaneko[f], J.Kang[l], E.-J.Kim[l], A.Kumagai[k], K.Kurita[k], J.-H.Lee[a], M.J.Levine[a], J.Luke[g], Y.Miake[k], A.Mignerey[m], B.Moskowitz[a], M.Moulson[d], C.Müentz[a], S.Nagamiya[d], M.N.Namboodiri[g], C.Ogilvie[h], J.Olness[a], L.P.Remsberg[a], H.Sako[k], T.C.Sangster[g], R.Seto[c], J.Shea[m], K.Shigaki[j], R.Soltz[g], S.G.Steadman[h], G.S.F.Stephans[h], M.J.Tannenbaum[a], J.H.Thomas[g], S.Ueno-Hayashi[k], F.Videbæk[a], F.Wang[d], Y.Wang[d], Y.Wu[d], H.Xiang[c], G.H.Xu[c], K.Yagi[k], H.Yao[h], W.A.Zajc[d], Q.Zhu[c], F.Zhu[a]

[a] Brookhaven National Laboratory, Upton, NY 11973

[b] University of California, Space Sciences Laboratory, Berkeley, CA 94720

[c] University of California, Riverside, CA 92507

[d] Columbia University, New York, NY 10027 and Nevis Laboratories, Irvington, NY

10533
[e] Institute for Nuclear Study, University of Tokyo, Tokyo 188, Japan
[f] Kyoto University, Sakyo-ku, Kyoto 606, Japan
[g] Lawrence Livermore National Laboratory, Livermore, CA 94550
[h] Massachusetts Institute of Technology, Cambridge, MA 02139
[i] Niels Bohr Institute for Astronomy, Physics, and Geophysics, University of Copenhagen, Denmark
[j] Department of Physics, University of Tokyo, Tokyo 113, Japan
[k] University of Tsukuba, Tsukuba, Ibaraki 305-8571, Japan
[l] Yonsei University, Seoul 120-749, Korea
[m] University of Maryland,College Park, MD 20742

Bibliography

[1] C. Bernard *et al.*, Phys. Rev. **D55** (1997) 6861.

[2] E. Laermann, Nucl. Phys. **A610** (1996) 1c.

[3] S. A. Bass *et al.*, J. Phys. **G25** (1999) R1.

[4] H. R. Schmidt and J. Schukraft, J. Phys. **G19** (1993) 1705.

[5] T. Matsui and H. Satz, Phys. Lett. **B178** (1986) 416.

[6] T. Matsui, Z. Phys. **C38** (1988) 245.

[7] M. C. Abreu *et al.*, (NA50 Collaboration), Phys. Lett. **B450** (1999) 456.

[8] E. V. Shuryak, Phys. Lett. **78B** (1978) 150.

[9] G. Agakichiev *et al.*, (CERES Collaboration), nucl-ex/9910015, Proceedings of XIV int. Conf. on Nucleus-Nucleus Collisions, Quark Matter 99, Torino, Italy.

[10] G. Agakichiev *et al.*, (CERES Collaboration), Nucl. Phys. **A638** (1998) 159c.

[11] D. H. Rischke, Nucl. Phys.**A610** (1996) 88c.

[12] D. K. Srivastava *et al.*, Nucl. Phys. **A610** (1996) 350c.

[13] L. A. Winckelmann *et al.*, Nucl. Phys. **A610** (1996) 116c.

[14] C. M. Ko *et al.*, Nucl. Phys. **A610** (1996) 342c.

[15] F. B. Yano, S. E. Koonin, Phys. Lett. **B78** (1978) 556; M. I. Podgoretskii, Sov. J. Nucl. Phys. **37** (1983) 272.

[16] U. Heinz, Nucl. Phys. **A610** (1996) 264c.

[17] H. Appelshäuser *et al.*, Eur. Phys. J. **C2** (1998) 661.

[18] T. Chujo, Progress of Theoretical Physics Suppl. **129** (1997) 173.

[19] R. J. Glauber, Lectures in Theoretical Physics **1**, Interscience Publishers, New York, (1959).

[20] K. Guettler *et al.*, Phys. Lett. **B64** 111.

[21] C. Michael, Part. Nucl. Phys. **2** (1979) 1.

[22] R. Hagedorn, Riv. Nuovo Cimento **6** 1983 1.

[23] Y. A. Tarasov, Sov. J. Nucl. Phys. **42** (1985) 260.

[24] T. Abbott *et al.*, (E802 Collaboration), Phys. Rev. Lett. **66** (1991) 1567.

[25] L. Ahle *et al.*, (E802 Collaboration), Phys. Rev. **C57** (1998) R466.

[26] L. Ahle *et al.*, (E802 Collaboration), Phys. Rev. **C60** (1999) 044904.

[27] E. Schnedermann *et al.*, Phys. Rev. **C48** (1993) 2462.

[28] T. Abbott *et al.* (E802 Collaboration), Phys. Rev. **C50** (1994) 1024.

[29] P. Braun-Munzinger *et al.*, Phys. Lett. **B344** (1995) 43.

[30] R. Hanbury-Brown and R. Q. Twiss, Phil. Mag. **45** (1954) 633; R. Hanbury-Brown and R. Q. Twiss, Phil. Mag. Nature **177** (1956) 27; R. Hanbury-Brown and R. Q. Twiss, Phil. Mag. Nature **178** (1956) 1046.

[31] C. Y. Wong, Introduction to High-Energy Heavy-Ion Collisions, World Scientific Pub. Co., Pte. Ltd., (1994) pp431.

[32] E. V. Shuryak, Phys. Rep. **61** No.2 (1980) 72.

[33] J. D. Bjorken, Phys. Rev. **D27** (1993) 140.

[34] A. N. Makhlin, Y. M. Sinyukov, Z. Phys. **C39** (1988) 69.

[35] Y. M. Sinyukov, Nucl. Phys. **A498** (1989) 151.

[36] G. F. Bertsch, Nucl. Phys. **A498** (1989) 173.

[37] S. Pratt, T. Csörgö, J. Zimanyi, Phys. Rev. **C42** (1990) 2646.

[38] S. Pratt, Phys. Rev. **D33** (1986) 1314.

[39] U. Heinz *et al.*, Phys. Lett. **B382** (1996) 181.

[40] S. Chapman, J. R. Nix, U. Heinz, Phys. Rev. **C52** (1995) 2694.

[41] J. Barrette *et al.* (E877 Collaboration), Nucl. Phys. **A638** (1998) 69c.

[42] Y. -F. Wu *et al.*, Eur. Phys. J. **C1** (1998) 599.

[43] C. Chasman and H. Hamagaki *et al.*, Proposal submitted to the AGS Program Committee (1990).

[44] H. Sako, Doctor thesis, University of Tokyo (1997).

[45] T. Roser, 4th European Particle Accelerator Conference, EPAC-94, London England. BNL Preprint BNL-49700 (1994).

[46] D. Deavis, private communication.

[47] J. B. Cumming, E866 Memo **16**, BNL-62000 (1995).

[48] D. Beavis *et al.* Nucl. Inst. and Meth. **A281** (1989) 367.

[49] J. C. Dunlop and M. D. Baker, E866 Memo **19**, BNL (1995).

[50] F. Videbæk *et al.*, (E802 Collaboration), Nucl. Phys. **A590** (1995) 249c.

[51] J. Chang, (E802 Collaboration), Proceedings of 13th Winter Workshop on Nuclear Dynamics (1997).

[52] L. Ahle *et al.*, (E802 Collaboration), Phys. Rev. **C54** (1999) 2173.

[53] K. Shigaki, Master's thesis, University of Tokyo (1992).

[54] H. Sako, Master's thesis, University of Tokyo (1993).

[55] A. Kumagai, Master's thesis, University of Tsukuba (1994).

[56] T. Abbott *et al.*, (E802 Collaboration), Nucl. Inst. and Meth. **A290** (1990) 41.

[57] K. Ashktorab, M. J. LeVine, and R. A. Scheetz, IEEE Transactions on Nuclear Science **41** (1994) 13.

[58] H. Sako, E866 memo, E866 Memo **15**, BNL (1995).

[59] CERN Computing and Network Division, GEANT 3.1.5 Manual.

[60] K. Kadija (NA49 Collaboration), Nucl. Phys. **A610** (1996) 248c.

[61] G. Baym and P. Braun-Munzinger, Nucl. Phys. **A610** (1996) 286c.

[62] C. M. Hung and E. V. Shuryak, Phys. Rev. Lett. **75** (1995) 4003.

[63] D. H. Rischke, S. Bernard, J. A. Maruhn, Nucl. Phys. **A595** (1995) 346.

[64] D. H. Rischke and M. Gyulassy, Nucl. Phys. **A597** (1996) 701.

[65] I. G. Bearden *et al.*, (NA44 collaboration), Nucl. Phys. **A638** (1998) 103c.

[66] H. Appelshäuser *et al.*, (NA49 collaboration), Nucl. Phys. **A638** (1998) 91c.

[67] E. Andersen *et al.*, (WA97 collaboration), Nucl. Phys. **A638** (1998) 115c.

[68] L. P. Csernai, Introduction to Relativistic Heavy Ion Collisions, John Wiley & Sons Ltd., (1994).

[69] S. Chapman, P. Scotto, U. Heinz, Heavy Ion Physics **1** (1995) 1.

[70] N. Herrmann, Nucl. Phys. **A610** (1996) 49c.